Impacts of regular head waves on thrust deduction at model self-propulsion point

(article starts on next page)

Impacts of regular head waves on thrust deduction at model self-propulsion point

Mohsen Irannezhad [a],[*], Martin Kjellberg [b], Rickard E. Bensow [a], Arash Eslamdoost [a]

[a] *Department of Mechanics and Maritime Sciences, Chalmers University of Technology, 412 96, Gothenburg, Sweden*
[b] *RISE - SSPA Maritime Center, 412 58, Gothenburg, Sweden*

ARTICLE INFO

ABSTRACT

The results obtained from the self-propulsion simulations using Computational Fluid Dynamics (CFD) in the current study, for a ship free to heave, pitch and surge with the means of a weak spring system, are combined with the formerly executed CFD results of the bare hull and propeller open water simulations to investigate the impacts of regular head waves on the propeller-hull interactions in comparison to calm water, at the self-propulsion point of the model. Despite a rather significant dependency of the nominal wake on the wave conditions, the Taylor wake fraction remains almost unchanged in different studied waves which is around 12% lower than the calm water value. The thrust deduction factor in waves is reduced (12.8%–26.1%) in comparison to the calm water value. The change of thrust deduction factor is found to be associated with the boundary layer contraction/expansion and vortical structure dynamics, originating from the wave orbital velocities as well as the significant shaft vertical motions and accelerations that resulted in a modified propeller action, and consequently diminished suction effect on the aft ship. The altered thrust deduction factor and wake fraction in waves in comparison to calm water underlines the significance of waves on the propulsive factors and propeller design.

1. Introduction

Ship hydrodynamics investigations have traditionally focused on the performance evaluation in calm water condition, even though such an ideal scenario is relatively rare in a realistic seaway. Thus, the prediction of the required power, as one of the important ship performance characteristics, often concerns the calm water condition. However, the required power of a ship to maintain the same speed in a more realistic environmental condition than calm water may undergo a significant variation. Added resistance due to waves and wind as well as the change of propulsion characteristics due to the variation of propeller/engine load (originated primarily from the complex change of wake encountered by the propeller due to ship motions, speed oscillations and propeller ventilation/emergence) for a ship operating in an actual sea may adversely affect the obtained ship speed at a constant calm water powering, (Bhattacharyya, 1978). This involuntary speed loss in addition to the voluntary adjustment of the engine speed for course keeping or prevention of green water, slamming, excessive accelerations and propeller racing, may have a substantial impact on the ship performance.

In the design process, to diminish the involuntary speed loss and determine a compatible machinery system that ensures reliable ship performance in practical scenarios, an experience-based reserved power of 15–25%, referred to as "sea margin" according to ITTC (2017), is usually added to the predicted required power in calm water. While this practice has demonstrated its adequacy in predicting power requirements for numerous vessels over the years, it can potentially result in underpower/overpower situations as the ships may seldom encounter such severe conditions. Today, with the development of advanced power prediction methods, there is a growing tendency for ship/propeller design optimization in operational conditions closer to near-service conditions rather than the traditional calm water considerations.

In an actual seaway, waves stand out as a considerable element impacting the power requirements of a ship, as the interactions between waves, hull and the propulsion system of the ship may significantly affect the ship motions, resistance, wake and propeller/engine load. It is well-established, for instance by Gerritsma et al. (1961), Moor and Murdey (1970), Van Sluijs (1972) and Nakamura and Naito (1975), that the propulsive factors are different in waves in comparison to calm water, which may results in a significant ship performance degradation. Consequently, it is critically important to predict the ship performance

---

* Corresponding author.
E-mail address: mohsen.irannezhad@chalmers.se (M. Irannezhad).

Nomenclature

$(P/D)_{0.7R}$	Pitch ratio at $r/R = 0.7$ (-)
$\bar{\eta}_D$	Mean of propulsive efficiency (-)
$\bar{\eta}_H$	Mean of hull efficiency (-)
$\bar{\eta}_O$	Mean of propeller open water efficiency read off from propeller open water curves through the thrust identity method (-)
$\bar{\eta}_R$	Mean of relative rotative efficiency (-)
$\bar{\psi}$	Mean (time-averaged) of quantity under study in Fourier analysis
$\bar{\psi}$	The mean value of the quantity under study in Fourier analysis
$\bar{J}_T$	Mean of advance ratio read off from propeller open water curves through the thrust identity method (-)
$\bar{K}_{Q_O}$	Mean of propeller torque coefficient read off from propeller open water curves through the thrust identity method (-)
$\bar{t}$	Mean of thrust deduction factor (-)
$\bar{w}_T$	Mean of Taylor wake fraction (-)
$\ddot{\Delta}z_{shaft}$	Vertical acceleration of the shaft center (m/s^2)
$\ddot{x}$	Surge acceleration (m/s^2)
Δt	Time step (s)
Δz_{shaft}	Vertical displacement of shaft from its initial position (m)
Δ	Mass displacement (kg)
$\dot{x}$	Surge velocity (m/s)
λ	Wave length (m)
μ	Heading angle (deg)
∇	Volume displacement (m^3)
ν	Kinematic viscosity of water (m^2/s)
Ω	Propeller rotational angular velocity (rad/s)
ω	Fast Fourier Transform frequency (rad/s)
ω_b	Blade passing frequency (rad/s)
ω_E	Encounter wave frequency (rad/s)
ω_p	Propeller frequency equal to Ω (rad/s)
ω_w	Wave frequency (rad/s)
ω_{spring}	spring natural frequency (rad/s)
$\psi(t)$	Time series of the quantity under study in Fourier analysis
ψ_i	The ith harmonic amplitude of quantity under study in Fourier analysis
$\psi_{\varepsilon i}$	The ith harmonic phase of quantity under study in Fourier analysis
ρ	Water density (kg/m^3)
Θ	Azimuthal position on propeller disk (deg)
θ	Pitch motion (deg)
θ_i	The ith harmonic amplitude of pitch motion at wave encounter frequency (deg)
θ_{sk}	Skew angle (°)
ζ	Free surface elevation (m)
A	Wave amplitude $H/2$ (m)
A_E/A_O	Expanded area ratio (-)
B	Breadth at mid-ship (m)
C_B	Block coefficient (-)
C_T	Non-dimensional bare hull total resistance (-)
$C_{0.7R}$	Chord length at $0.7R$ (m)
D	Propeller diameter (m)
D_{hub}	Hub diameter (m)
F_0	External constant force (N)

F_D	Skin friction correction tow force (N)
Fr	Froude number (-)
g	Gravitational acceleration (m/s^2)
H	Wave height (m)
K	Spring stiffness (N/m)
k	Wave number $360/\lambda$ (deg/m)
K_Q	Propeller torque coefficient (-)
K_T	Propeller thrust coefficient (-)
K_{yy}	Mass radius of gyration around Y-axis (m)
L	Length between perpendiculars (m)
L_{CG}	Longitudinal position of center of gravity from aft perpendicular (m)
m_1	Mass of hull and pitch-free gimbal (kg)
m_2	Mass of dynamometer (kg)
m_3	Mass of light weight carriage (kg)
n	Propeller rotational speed (rps)
P_D	Delivered power (W)
Q	Propeller torque (Nm)
R	Propeller radius (m)
r	Radial position on propeller disk (m)
R_T	Bare hull total resistance (N)
R_{hub}	Hub radius (m)
Re	Reynolds number (-)
S	Bare hull wetted surface area at rest (m^2)
T	Propeller thrust (N)
t	Time (s)
T_A	Draft at aft perpendicular (m)
T_b	Blade passing time period $2\pi/\omega_b$ (s)
T_E	Wave encounter period (s)
T_F	Draft at fore perpendicular (m)
T_p	Propeller revolution time period $2\pi/\omega_p$ (s)
T_{spring}	Spring natural period $2\pi/\omega_{spring}$ (s)
U	Ship velocity (m/s)
u	Axial velocity component of propeller slipstream or bare hull nominal wake (m/s)
U_A	Speed of advance in propeller open water condition (m/s)
V_{CG}	Vertical position of center of gravity from keel (m)
x	Surge motion (m)
x_i	The ith harmonic amplitude of surge motion at wave encounter frequency (m)
x_{1_s}	The 1st harmonic amplitude of surge motion at spring natural frequency (m)
X_{prop}	Longitudinal position of propeller center forward aft perpendicular (m)
y^+	Non-dimensional wall distance for a wall-bounded flow (-)
z	Heave motion (m)
z_i	The ith harmonic amplitude of heave motion at wave encounter frequency (m)
Z_{prop}	Vertical position of propeller center under water line (m)
R_{Ti}	The ith harmonic amplitude of bare hull total resistance at wave encounter frequency (N)
v	Transversal velocity component of bare hull nominal wake (tangential to the plane of study in Y, in which axial velocity component is defined on) (m/s)
w	Vertical velocity component of bare hull nominal wake (tangential to the plane of study in Z, in which axial velocity component is defined on) (m/s)

in waves, particularly in the early stages of the ship design process. Assessing the performance of a ship across every possible wave condition (wave height, length and propagation direction) and operational conditions (such as loading condition, forward speed, propeller rotational speed, rudder angle and engine/machinery system operation point) is practically unfeasible. However, from a hydrodynamics engineering perspective, the focus lies on understanding the physical phenomena associated with fluid flow and their impacts on ship performance in waves. Therefore, the ship performance can be initially analyzed in a selective number of simplified scenarios and then advanced to more complex circumstances.

One of the commonly considered simple scenarios is the investigation of the propeller-appended bare hull hydrodynamic performance in regular head waves in model-scale. This case not only offers a simpler ship behavior in such waves, but also disregards the complexities imposed by the other components of the propulsion system than the propeller. Moreover, investigations in model-scale are usually carried out under a more controlled condition compared to full-scale, hence enabling a clearer understanding of the entailed physics. Furthermore, by integrating the findings from these self-propulsion (propeller-appended bare hull) studies with the results of the bare hull and propeller open water (POW) investigations, the propeller-hull interaction effects on the ship performance, such as thrust deduction factor and wake fraction, in conjunction with the other propulsive factors can be analyzed.

In the literature, several experimental and numerical investigations are available related to the hydrodynamic performance assessment of self-propelled ships in calm water and regular head waves. The International Towing Tank Conference (ITTC) outlines, e.g., in ITTC (2021e,g) and ITTC (2021f), the common techniques used in the model test experiments in towing tanks or seakeeping basins, referred to as Experimental Fluid Dynamics (EFD), to evaluate the propulsion characteristics of ships. While these measurements are expensive and time-consuming, they often yield rather accurate results. On the other hand, numerical methods, which often incorporate state-of-the-art Computational Fluid Dynamics (CFD) techniques, can be employed to study the self-propulsion performance of ships. The CFD methods can provide valuable insights into the entailed fluid flow, which is challenging, costly and extremely cumbersome to acquire via model tests, if even possible. The CFD methods based on the so-called Reynolds-Averaged Navier–Stokes (RANS) approach are widely used in the context of ship hydrodynamics in calm water and regular head waves. Common practices in ship hydrodynamics often involve a combined approach, utilizing both model tests and numerical predictions. The numerical results are then validated using the experimental measurements, and subsequently analyzed to extract and gain detailed information about the ship hydrodynamic performance.

Numerous examples of the EFD and/or CFD self-propulsion investigations in regular head waves can be found in the literature, for instance in the studies by Gerritsma et al. (1961), Moor and Murdey (1970), Van Sluijs (1972), Nakamura and Naito (1975), Faltinsen et al. (1980), Tanibayashi (1983), Lee et al. (2010), Ueno et al. (2013), Bhattacharyya and Steen (2014), Tokgoz (2015), Lee et al. (2019), Sigmund (2019), Seo et al. (2020), Saettone (2020), Wu et al. (2020), Mwangi (2021), Lee et al. (2021), Kim et al. (2021), Mikkelsen (2021), Sanada et al. (2022), Woeste et al. (2022), Lee et al. (2022), Yu et al. (2022), Cai et al. (2023), Kim et al. (2023) and Lee et al. (2023). Different set of considerations are taken into account in each of these investigations, which are discussed in the following.

- Each investigation is carried out in a particular choice of Degrees of Freedom (DOF). While waves and the rotation of the propeller can induce all six ship motions, the primary motions in regular head waves are surge, heave, and pitch.
  The free-running self-propulsion investigations are carried out in 6DOF, in which an active rudder required to maintain the ship in the desired heading angle relative to the incoming waves.

Consequently, additional complexities are often involved in the free-running self-propulsion investigations.
The majority of the investigations neglected the necessity of surge motion on the propeller incident wake and ship performance, hence they only considered the heave and pitch motions (2DOF) while the ship was moved at the constant desired velocity at a chosen propeller rotational speed. Consequently, the ship velocity oscillations during one wave encounter period are overlooked in 2DOF investigations and there is no assurance that the chosen propeller rotational speed would yield the desired ship velocity during performance in waves.
The investigations in 3DOF (surge, heave and pitch) are not common, mainly due to the complexities involved in such conditions. In 3DOF investigations, if the ship is completely free in surge motion, then the propeller rotational speed should be adjusted to achieve the desired ship velocity. However, obtaining the precise desired velocity might be practically challenging, particularly in regular head waves, as there are various factors influencing the ship performance due to the complex propeller-hull interactions. On the other hand, the free surge condition (3DOF) can be applied using a weak spring system, meaning that one side of the spring is moved with the desired ship velocity and the other side is connected to the ship. For instance, the test setup in this type of 3DOF experimental model tests enables the ship to surge while it is towed with a light-weight carriage connected to the main carriage through the weak spring system. Then, the ship behavior, especially surge motion, consists of extra harmonic components in the spring natural frequency aside from the wave encounter frequency, whereas the ship velocity during the spring natural period remains very close to the desired ship velocity.

- The investigations can be categorized according to the choice of the propeller loading, often defined through the operational point at which the ship resistance and propeller thrust are in equilibrium (self-propulsion point).

The majority of the investigations focused on the ship performance evaluation in full-scale, mainly through the initial analysis in model-scale and then extrapolation to full-scale results, for instance using the 1978 ITTC Performance Prediction Method outlined in ITTC (2021f). Therefore, the common practice in model-scale self-propulsion investigations usually accounts for the theoretically correct propeller loading in model-scale to justify reliable scaling results. This correction is usually applied through an external tow force in model-scale self-propulsion conditions, called skin friction correction force, to unload the propeller. When this force is considered, the operational point is called "the self-propulsion point of the ship" (ship SPP), and it should be considered for the derivation of the thrust deduction factor, as one of the important propeller-hull interactions factors.
In the aforementioned studies, the skin friction correction force is estimated using different equations. For instance, the estimation equation varies among studies by Seo et al. (2020), Cai et al. (2023), Sigmund (2019) and Bhattacharyya and Steen (2014), which are also different from the newest ITTC equation provided in ITTC (2021e) and ITTC (2021f) and older equations presented in ITTC (2021d). Consequently, the estimated skin friction correction force from these equations results in remarkably different values, hence leading to distinct shifting of the propeller loading and uncertainty in the self-propulsion point of the ship (ship SPP). In the ship SPP, it is often assumed that the skin friction correction force is similar between calm water and waves, as the averaged frictional resistance per encountered wave period is assumed to remain identical to the calm water frictional resistance. However, based on the investigations carried out by Irannezhad et al. (2023) and Sigmund (2019), it is seen that this assumption is not valid as the frictional component of the added resistance due to waves is determined to be considerable. This introduces an additional uncertainty to the correct propeller loading consideration in waves in the case of ship SPP.

- As the objectives of individual investigations differ, the self-propulsion condition may vary based on considerations such as the presence/absence of the rudder, propeller duct (open or ducted propeller) and Energy Saving Devices (ESDs). Moreover, the bare hull and POW investigations are only included in some of the studies. Therefore, the analyzed quantities as well as the post-processing techniques vary between different studies.
- The CFD investigations can be divided according to how the propeller is modeled in the simulations. In the majority of the studies, the propeller rotation and its effects are implemented using a virtual disk or through the higher fidelity approach by the discretized propeller geometry. The choice is based on the availability of computing resources, as the computational costs of the simulations incorporating the discretized propellers are often a few orders of magnitude higher than the more simple approaches. Nevertheless, more accurate computations are expected using the discretized propellers.

The main objective of the current paper is to analyze the impact of regular head waves on the propeller-hull interactions, in comparison to calm water condition. To this end, a set of CFD simulations (using RANS approach) are carried out in this study for a propeller-appended hull (self-propulsion) in calm water and regular head waves. The KVLCC2 tanker equipped with the KP458 propeller is chosen as the case study in this paper. The propeller is modeled in the simulations using the discretized approach.

Contrary to most of the aforementioned studies in literature, the investigations in this paper concern the ship free to surge (3DOF) by means of a weak spring system, enabling enhanced evaluations of the ship behavior and propeller performance in waves. Since the focus lies on the flow physics analysis, solely the model-scale condition is addressed in this paper. Therefore, the self-propulsion point of the model (model SPP) is examined considering skin friction correction force equal to zero, in order to eliminate the aforementioned estimation uncertainties related to the propeller loading involved in the application of this force. Moreover, the self-propulsion results are combined with the results of the bare hull performance investigations in Irannezhad et al. (2023) and propeller open water (POW) performance investigations in Irannezhad et al. (2024) in similar operational conditions to derive the propulsion characteristics of the ship, mainly the thrust deduction and wake fraction. In this way, the common assumption in the added power prediction methods on equal thrust deduction factor and wake fraction in calm water and waves, e.g., in the Thrust and Revolution Method (TNM) as well as the Resistance and Thrust Identity Method (RTIM) in ITTC (2021g), is examined. Suitable convergence criteria and post-processing techniques are utilized in this paper and the available model test data, including local flow measurements, are used to validate the results. The analyses from this paper can shed more light onto the propeller-hull interaction effects in regular head waves and help the ship/propeller designers optimize their designs for more realistic environmental conditions than only calm water.

2. Hull and propeller geometries and operational conditions

The ship under study is the second variant of the MOERI tanker (KVLCC2) in model-scale (scale factor = 100) appended with KP458 propeller, originally designed by Korea Research Institute of Ships and Ocean Engineering (KRISO, formerly MOERI), and a hub cap. The investigations concern the design loading condition (fully-loaded) of the ship. The propeller and hull main particulars in the fully-loaded operational condition are provided in Table 1.

This study evaluates the hydrodynamic performance of the ship operating in fresh water with the density of $\rho = 998.1$ kg/m^3 and the kinematic viscosity of $\nu = 1.002 \times 10^{-6}$ m^2/s. The investigations are conducted at the design speed of the ship $U = 0.79739$ m/s, hence at the Froude number of $Fr = U/\sqrt{gL} = 0.142$ and Reynolds number of $Re = UL/\nu = 2.546 \times 10^6$.

The investigated environmental conditions in this study are identical to the conditions considered for the bare hull study presented by Irannezhad et al. (2023), i.e., calm water and three regular head waves with the same wave height $H = 0.06$ m and three different wave lengths $\lambda/L = 0.6$, 1.1 and 1.6. The wave encounter frequency ω_E and encounter period T_E can then be determined for each wave length by utilizing the corresponding wave frequency ω_w and the heading angle $\mu = 180°$ as,

$$\omega_E = \omega_w - \frac{\omega_w^2 U}{g}\cos(\mu), \qquad T_E = 2\pi/\omega_E. \qquad (1)$$

The propulsion characteristics are mainly investigated at the self-propulsion point of the model (model SPP). Therefore, the skin friction correction tow force F_D (which is often considered to correct the loading on the propeller in model-scale for a practical result extrapolation to full-scale) is not adopted ($F_D = 0$ N) in this study. This is because of the aforementioned uncertainties involved in the derivation of F_D from the current literature, as there are various estimation methods available from which significantly different F_D are calculated for the same conditions. The choice of model SPP is yet in line with the objectives of this paper, as the main aim is to study the flow physics and how it affects the propeller-hull interactions in regular head waves in comparison to calm water. Therefore, since the investigations only concern the model-scale condition, the consideration of the model SPP for the analysis of the flow physics appears coherent. However, it should be kept in mind that at the self-propulsion point of the model (model SPP), the propeller is highly loaded which may result in amplification of the propeller-hull interaction effects when compared to the full-scale.

The available experimental data from Osaka University Towing Tank, provided by Mwangi (2021), is used for validation of the computational results. Given that the primary objective of these model tests was to analyze Energy Saving Devices (ESDs), an identical propeller rotational speed of $n = 16.50$ rps was considered in calm water and waves, which does not represent the model SPP in waves. Consequently, the CFD investigations in this paper are divided into two categories: one focusing on the validation practice by considering similar propeller rotational speed as in EFD, and another for the analysis of the propeller-hull interaction effects by applying the propeller rotational speeds at the model SPP. The investigated operational conditions are presented in Table 2.

Two reference frames are defined: a carriage-fixed reference frame (CF) and a hull-fixed reference frame (HF). While the reference frame fixed to the carriage is assumed to move in the longitudinal direction at the design speed U, the reference frame fixed to the hull follows the ship motions and its instantaneous speed. Accordingly, three Cartesian coordinate systems are considered: CF_{COG} and CF_{PSP} in the CF reference frame as well as HF_{COG} in HF reference frame. Moreover, a Cylindrical coordinate system at the propeller center HF_{PC} is defined in the HF reference frame. These coordinate systems at the initial position of the ship are shown in Fig. 1. The curved arrow marked by Ω (propeller rotation rate) illustrates the rotation direction of the right-handed propeller, which is in the decreasing azimuthal angle Θ direction. For a clearer understanding of the single-blade analysis in this paper, the blades are numbered in the propeller rotational direction.

CF_{COG} and HF_{COG} are defined at the initial positions of ship Center of Gravity (COG) and at the beginning have X-axis pointing towards the ship advancing direction, Y-axis towards portside and Z-axis pointing upwards. During the ship performance, CF_{COG} moves with the constant ship velocity of U and its orientation always remains unchanged, whereas HF_{COG} moves with the instantaneous ship velocity and its orientation changes based on the instantaneous ship motions. As a result, positive surge occurs when HF_{COG} moves forward of CF_{COG} in the longitudinal direction, positive heave occurs when HF_{COG} moves upwards and positive pitch occurs when ship stern moves upwards (bow moves downwards).

Table 1
Model-scale KVLCC2 vessel bare hull and propeller main particulars (scale factor = 100).

Symbol	Value/Type	Unit	Denotation
Bare Hull			
L	3.2	(m)	Length between perpendiculars
B	0.58	(m)	Breadth at mid-ship
T_F	0.208	(m)	Draft at fore perpendicular
T_A	0.208	(m)	Draft at aft perpendicular
∇	0.312622	(m³)	Volume displacement
Δ	312.028	(kg)	Mass displacement
S	2.7194	(m²)	Bare hull wetted surface area at rest
C_B	0.8098	(–)	Block coefficient
L_{CG}	1.71136	(m)	Longitudinal position of COG from aft perpendicular
V_{CG}	0.186	(m)	Vertical position of COG from keel
K_{yy}	0.8	(m)	Mass radius of gyration around Y-axis (pitch)
Propeller - KP458 (based on Osaka University Towing Tank model setup)			
D	0.0986	(m)	Propeller diameter
D_{hub}	$0.155D$	(m)	Hub diameter
$(P/D)_{0.7R}$	0.721	(–)	Pitch ratio at $r/R = 0.7$
A_E/A_O	0.431	(–)	Expanded area ratio
θ_{sk}	21.15	(°)	Skew angle
$C_{0.7R}$	0.0226	(m)	Chord length at $r/R = 0.7$
–	4	(–)	Number of blades
–	FPP	(–)	Fixed Pitch Propeller type
–	Right-handed	(–)	Rotation direction
X_{prop}	$0.02L$	(m)	Longitudinal position of propeller center forward aft perpendicular
Z_{prop}	$0.046875L$	(m)	Vertical position of propeller center under water line

Table 2
Investigated operational conditions.

Environmental Condition	H (m)	T_E (s)	n (rps)	EFD	CFD	Purpose
Calm Water	–	–	16.50	✓	✓	Validation & Model SPP
Wave $\lambda/L = 0.6$	0.06	0.7593	20.00	–	✓	Model SPP
Wave $\lambda/L = 1.1$	0.06	1.1204	16.50	✓	✓	Validation
			24.54	–	✓	Model SPP
Wave $\lambda/L = 1.6$	0.06	1.4125	19.44	–	✓	Model SPP

Fig. 1. Initial location and orientation of the defined coordinate systems.

In the model tests, the propeller slipstream velocity distribution was measured on a carriage-fixed Propeller Slipstream Plane (PSP) located 0.08 m ($0.025L$) behind the initial position of the Aft Perpendicular (AP). Therefore, in the CFD simulations, CF_{PSP} coordinate system is defined with its origin initially located at the propeller slipstream plane in the longitudinal direction and the design waterline in the vertical direction. Similar to CF_{COG}, CF_{PSP} moves with the constant ship velocity of U, irrespective of the ship instantaneous speed or motions.

3. Experimental method

The experimental model tests were carried out by Mwangi (2021) in Osaka University Towing Tank (OU). The test setup, KVLCC2 model (scale factor = 100) and the appended KP458 propeller are shown in Fig. 2.

The surge motion was fixed in the calm water model test (2DOF). On the other hand, the model tests in waves were conducted in 3DOF, in which the model was free to surge while it was towed with a light-weight carriage connected to the main carriage through a weak spring

system, as sketched in Fig. 2(c). The occurrence of surge resonance, i.e., interference of the spring natural frequency with the surge motion frequency in the studied waves, was prevented by the choice of a suitable spring stiffness $K = 98$ N/m. In order to avoid large stretch/compression of the spring and maintain a near-to-zero mean surge in waves, an external constant force F_0 (estimated from a set of preliminary model tests) was considered in each model test, but the details of which are missing in the experimental reports. Instead of using an actual spring system, a servo motor was used in the tests to emulate the effects of the spring system and the external force. Then, the instantaneous resultant of F_0, $-Kx$ and $-m_3\ddot{x}$ was exerted to the ship center of gravity.

The hull was connected to the light-weight carriage through a pitch-free gimbal at COG and a heaving rod incorporating a load cell dynamometer for force measurements. The mass of the dynamometer ($m_2 = 6.4$ kg) in addition to the masses of hull and pitch-free gimbal ($m_1 = 306.2$ kg) were the only contributors to the heave and pitch motions ($m_1 + m_2 \approx \Delta$), while the light-weight carriage mass ($m_3 = 2.5$ kg) was also involved in the surge motion. Three potentiometers
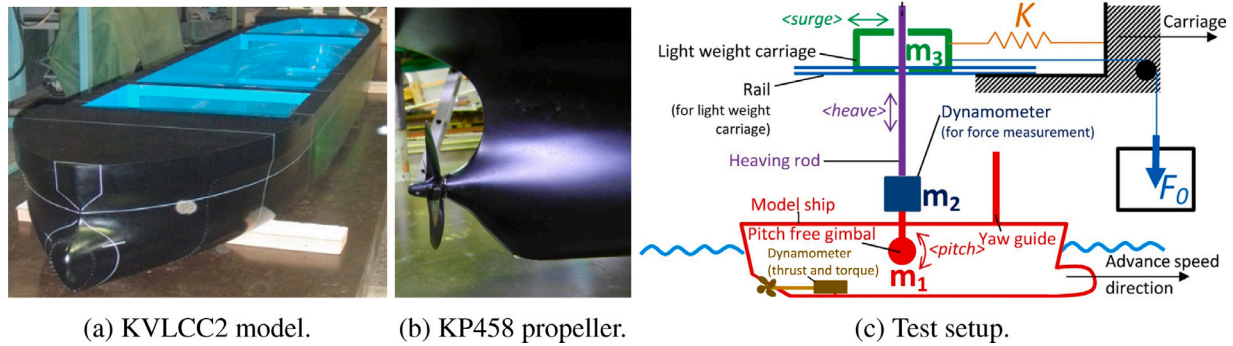
(a) KVLCC2 model. (b) KP458 propeller. (c) Test setup.

Fig. 2. KVLCC2 model, KP458 propeller and hub cap as well as the experimental setup for free surge conditions employing a spring system, adapted from the test campaign in the Osaka University Towing Tank, for instance, Kim (2014) and Mwangi (2021).

for motions measurement, a servo-type wave gauge (installed on the carriage 3.57 m ahead of fore perpendicular) for free surface elevation measurement and a self-propulsion dynamometer for thrust and torque measurement were employed. The sampling rate of the equipment was 100 Hz. Based on the measured water temperature, the Reynolds number in model tests was around $Re = 2.6159 \times 10^6$.

The velocity distribution of the flow at the propeller slipstream plane was measured using a 2-Dimensional Stereo Particle Image Velocimetry (SPIV) system fixed on the carriage. More information regarding the SPIV system can be found in Mwangi (2021). Since the propeller slipstream plane was fixed on the carriage, the instantaneous distance between the hull and the plane varied based on the instantaneous surge motion in the tests. The SPIV measurements were carried out at six different time instances of a wave encounter period. These time instances represent the incident wave elevation (at the wave gauge) phases of 0° (zero up crossing of wave at wave gauge), 60°, 120°, 180° (zero down crossing of the wave at wave gauge), 240° and 300°. Two vertical positions of the plane were considered in the SPIV measurements for each phase, in order to cover a larger area due to the large ship motions relative to the carriage. From the SPIV measurements, respectively around 230 and 115 images were collected and analyzed for calm water and each phase of the wave. One possible source of uncertainty stems from the actual SPIV timing as the incident free surface elevation may differ from the expected value during the run.

4. Numerical method

A commercial CFD solver, Simcenter STAR-CCM+ (version 2023.10), is employed to carry out the numerical simulations, in which the RANS equations for incompressible viscous flows are solved. The Reynolds stress is modeled by an Eddy Viscosity model, Boussinesq's hypothesis, using a quadratic constitutive relation to the strain and vorticity tensors, hence considering the anisotropy of the turbulence, details are provided in Simcenter STAR-CCM+ User Guide (2023). The $k - \omega\ SST$ turbulence model (with all y^+ wall treatment consideration), implemented according to Menter (1994), is used to model the turbulent viscosity through solving additional transport equations for turbulent kinetic energy k (TKE) and specific dissipation rate ω (SDR). The conservation equations for mass, momentum and turbulence quantities are solved using a segregated approach for coupling velocity and pressure fields. A Finite Volume method is used to discretize the continuous equations, considering a second-order spatial discretization scheme. The numerical methods in this paper are similar to the employed methods for the bare hull investigations in Irannezhad et al. (2023) and propeller open water investigations in Irannezhad et al. (2024).

The modeling of the free surface involves employing the Volume of Fluid (VOF) multiphase model and using the High-Resolution Interface Capturing scheme (HRIC) developed by Muzaferija and Perić (1998).

This scheme is applied to maintain a sharp interface between the incompressible fluid phases. In the simulations incorporating regular head waves, the 5th order Stokes waves are utilized due to their superior resemblance to real-world waves, as noted by Fenton (1985).

Different sources in the literature indicated the challenges involved in obtaining high-quality regular waves in both experimental tests and numerical simulations, for instance in ITTC (2021b,c) and Tavakoli et al. (2023). In numerical simulations, the challenges concern the change of wave amplitude and period during propagation, wave reflection at the boundaries of the computational domain and the presence of disturbances (wiggles) on the free surface, to name a few. It is often recommended, for instance by Perić and Abdel-Maksoud (2018, 2020), Berndt et al. (2021) and Perić et al. (2022), to tune the case-dependent simulation parameters for achieving higher-quality numerical waves. Therefore, prior to the self-propulsion simulations in this paper, wave propagation simulations in an empty domain (in the absence of the ship) have been carried out in Irannezhad et al. (2021) and Irannezhad (2022) to obtain a robust wave propagation simulation setup in the employed solver, hence diminishing/addressing the engaged wave propagation modeling errors. In these studies, the quality of the propagating numerical waves has been evaluated through comparison with the analytical wave, and the contributing factors to the discrepancies, such as quality of the cell sizes, dimensions of local refinement zones and accuracy of overset interpolations, have been discussed. The resultant simulation configurations, which are also applied in the self-propulsion simulations in the current study, yielded numerical waves that closely resembled the analytical counterpart, in which the discrepancies of the 1st harmonic amplitude (as the dominant harmonic component) remained primarily under 3%.

4.1. Computational domain

The computational domain is discretized using an Overset Mesh technique (for the ship motions) with a Least Square interpolation scheme, in conjunction with a Sliding Mesh technique (for rotation of the propeller) utilizing in-place internal interfaces. Consequently, the computational domain consists of three regions: background region, overset region and rotating mesh region (which also follows the ship motions and hence overset region motions). The dimensions of the computational domain and the engaged regions as well as the imposed boundary conditions are illustrated in Fig. 3.

To diminish the wave reflection from the boundaries, a wave forcing function is applied within a distance (equivalent to the ship length L) from all vertical boundaries with velocity inlet boundary conditions. In regular head waves simulations, the wave forcing function forces the solution of the discretized Navier–Stokes equations towards the theoretical 5th order Stokes wave solution. However, in calm water simulations, it forces the solution of the discretized Navier–Stokes equations towards the still water solution. Employing a wave probe, the
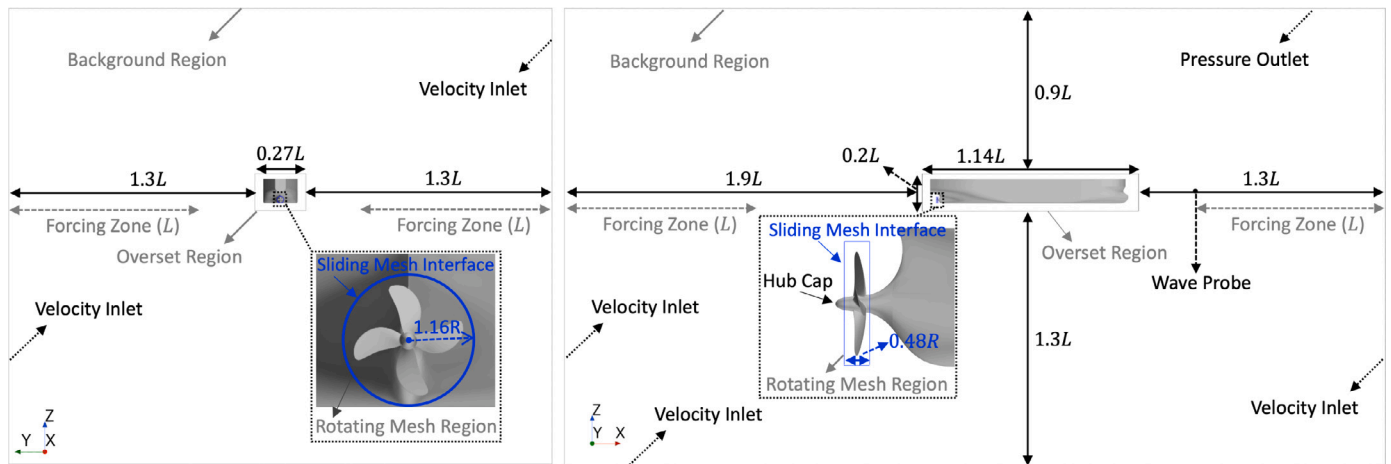
Fig. 3. Dimensions of the computational domain and engaged regions together with the applied boundary conditions and wave probe location.
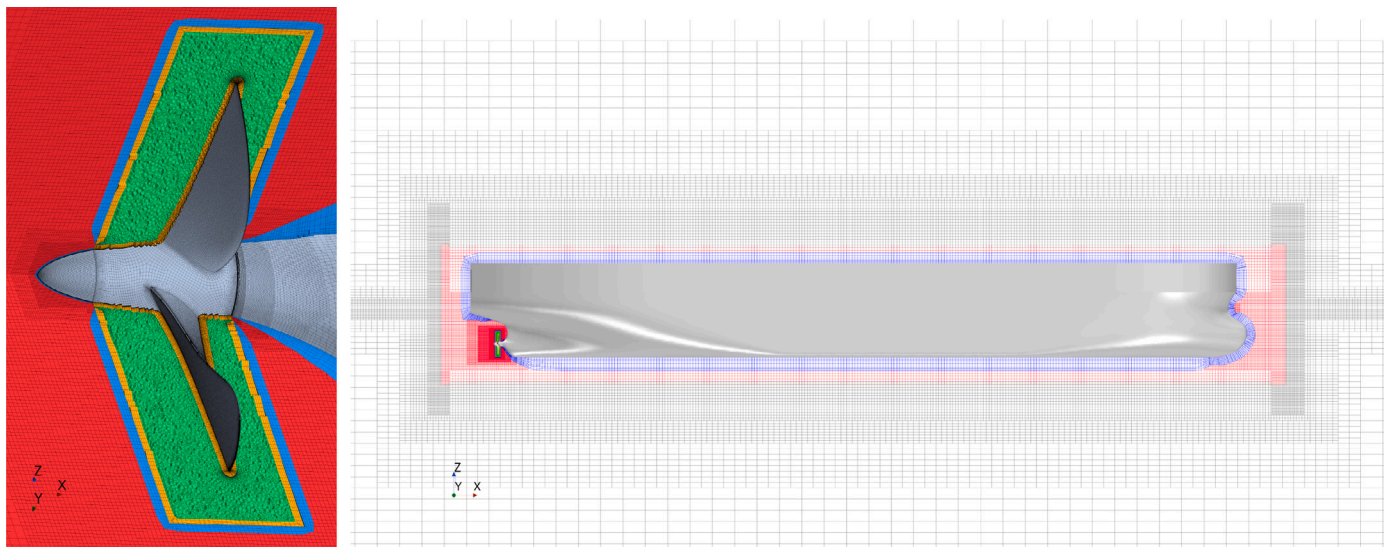

Fig. 4. Overview of the grid near the propeller and hull. Red and gray colors represent the trimmed hexahedral mesh in the overset and background regions, respectively. Blue and orange colors represent the prism layer meshes in the overset and rotating mesh regions, respectively. The green color represents the polyhedral mesh in the rotating mesh region.

numerical wave elevation is monitored at the end of the forcing zone in front of the fore perpendicular of the ship, in spite of the fact that the actual incident wave may be different from the monitored wave at the probe due to the numerical propagation errors. Nevertheless, according to the wave propagation investigations in Irannezhad et al. (2021), the utilized simulation configurations in this study ought to yield incident waves that closely resemble the analytical counterpart.

4.2. Grid generation

The employed grid in this study is primarily derived from merging the grids used in the bare hull investigations in Irannezhad et al. (2023) and POW investigations in Irannezhad et al. (2024) (adopting the grid refinement level of 1.00 in these investigations), using the STAR-CCM+ automatic mesh generator. Consequently, the self-propulsion simulations in this paper consist of a substantially larger number of cells ($\approx$ 27.5 million). This is attributed to the absence of the symmetry boundary condition, in contrast to the bare hull grid, and the integration of the propeller grid into the aft ship. The number of cells in the background, overset and rotating mesh regions are approximately 12.2 million, 7.7 million and 7.6 million cells, respectively. An overview of the employed grid is depicted in Fig. 4.

Unstructured grids are generated including the trimmed hexahedral meshes with local refinements near the free surface, hull and overset overlapping zone in the background and overset regions and polyhedral meshes with local refinements near the propeller in the rotating mesh region as well as prism layer meshes along the hull (including hub cap), propeller and sliding mesh interface in the overset and rotating mesh regions. The consideration of the smaller cell sizes near the overset overlapping zone and the generation of prism layers along the sliding mesh interface are introduced to derive more accurate information exchange between the regions.

The prism layers are generated in a way to yield the non-dimensional wall distance of $300 > y^+ > 30$ over the major part of the hull wetted surface area (using a wall function approach), but $y^+ < 1$ over the surface of the propeller and hub cap (using a wall-resolved approach).

Although a narrower local refinement zone near the free surface in calm water simulations, in comparison to regular wave simulations, drops the computational costs (increases computational efficiency) of such simulations, the same grid is employed in this study to minimize inconsistencies between simulations in calm water and waves. The bare hull studies by Sigmund (2019) and Irannezhad et al. (2023) also denote the usage of an identical grid in calm water and waves

simulations. The free surface local refinements in the employed grid in the current study result in approximately 10 cells per wave height H, but around 80, 147 and 213 cells per wave length for $\lambda/L = 0.6$, 1.1 and 1.6, respectively.

In the simulations, both the hull and the propeller are assumed to be rigid bodies and their hydroelasticity and flexibility are presumed negligible.

4.3. Time step

An implicit unsteady solver is employed with a second-order temporal discretizational scheme. The ITTC (2014b) recommended time step for the self-propulsion simulations incorporating the sliding mesh technique is $0.5° -2.0°$ of propeller revolution per time step. In the current study, $2°$ of propeller revolution per time step is considered resulting in the time step of $\Delta t = 2/(360n)$. In a separate simulation, the effect of time step reduction was studied by reducing the above mentioned time step by half, $\Delta t = 1/(360n)$, however, no significant change of thrust/torque was observed. Therefore, the selected time step was deemed conservative enough for the current analysis. The maximum number of inner iterations per time step is set to 20.

4.4. Motion modeling

The desired propeller rotational speed is applied to the rotating mesh region as well as the hub cap surface in form of wall tangential velocity boundary condition, to model the propeller and the hub cap revolution. It is worth mentioning that the simulations are initialized using a Moving Reference Frame (MRF) approach, prior to the revolution of the rotating mesh region, to reduce the computational costs by using significantly larger time steps.

The Dynamic Fluid Body Interaction (DFBI) module in STAR-CCM+ is utilized to model the ship motions (3DOF). The employed DFBI Rotation and Translation model accounts for the fluid, gravity and any external forces and moments. In addition to the constant force F_0, the effects of the light-weight carriage and spring, which were part of the experimental setup, are replicated through application of external forces $-m_3\ddot{x}$ and $-Kx$ in the ship advancing direction at the COG of the ship, in which $\ddot{x}$ is the instantaneous surge acceleration and x is the instantaneous surge motion. In each simulation time step, the computed $\ddot{x}$ and x from the previous time step are adopted to calculate the light-weight carriage and spring forces. According to the considered coordinate systems and reference frames, the positive surge x results in spring compression, as shown in Fig. 2(c), and hence a negative spring force $-Kx$ (i.e., in the opposite direction of ship forward speed).

4.5. Convergence criteria and post-processing techniques

In the self-propulsion simulations, the hydrodynamic forces on the propeller and hub cap surfaces are considered for obtaining thrust T and torque Q. The delivered power is then derived from $P_D = 2\pi nQ$. The thrust and torque coefficients in the self-propulsion condition, i.e., K_T and K_Q, are defined as,

$$K_T = \frac{T}{\rho n^2 D^4}, \qquad K_Q = \frac{Q}{\rho n^2 D^5}. \tag{2}$$

The required thrust T to drive a self-propelled ship at a velocity U is higher than the bare hull resistance R_T at that velocity. This originates from the propeller-induced acceleration (suction) of the flow and hence change of the pressure distribution at the aft-ship (close to propeller) in self-propulsion. It is more reasonable to consider the effects of the propeller behind the hull as causing an increase in resistance. However, it is also common practice to formulate this resistance increase as a deduction from the thrust available at the propeller, i.e., to assume that only part of the propeller thrust is available to overcome the bare

hull resistance. The increase of resistance or deduction of thrust in self-propulsion is often presented through thrust deduction factor t as,

$$t = 1 - \frac{R_T}{T}. \tag{3}$$

As mentioned before, F_0 is only introduced in the simulation concerning validation, i.e., solely in $\lambda/L = 1.1$ at $n = 16.5$ rps given in Table 2, to replicate the corresponding model test, whereas it is disregarded ($F_0 = 0$ N) in the model SPP simulations. Unfortunately, the applied F_0 in EFD is not available from experimental reports, hence an estimated value ($F_0 = 6.86$ N) is adopted in the simulation ($\lambda/L = 1.1$ at $n = 16.5$ rps) which may be counted as an essential source of discrepancy between EFD and CFD, due to a potentially unequal propeller loading and different distance between the model and the carriage-fixed propeller slipstream plane.

In each model SPP condition ($F_0 = 0$ N), it is required to have a propeller rotational speed that yields a zero mean surge motion (from the generated propeller thrust) during the ship performance at the intended ship velocity. However, it is extremely time-consuming and computationally expensive to find the precise propeller rotational speed at the self-propulsion point of the model (which yields precisely zero mean surge) in the RANS investigations, especially in regular head waves. Therefore, an estimated propeller rotational speed at the model SPP, given in Table 2, is adopted in the simulation in each condition. However, based on the accuracy of such estimation in each operational condition, the spring system response might vary, resulting in small (but not negligible) mean surge motion and acceleration and hence operating in a self-propulsion point very close, but not identical, to the self-propulsion point of the model (model SPP). Consequently, in the current study, the eventual mean spring and light-weight carriage forces are considered as external forces to adjust the force imbalance to reach the self-propulsion point at the desired ship forward velocity U.

The model SPP self-propulsion simulations (SP) results from the current study are combined with the bare hull (BH) investigations in Irannezhad et al. (2023) and propeller open water investigations in Irannezhad et al. (2024) to derive the propeller-hull interaction effects in calm water and regular head waves. An ideal propeller-hull interactions analysis may include derivation of instantaneous thrust deduction and wake fraction during the spring response time. However, this needs the simulations in bare hull and self-propulsion conditions to reach an ideally converged state with very small and constant oscillations of the ship instantaneous velocity and surge motion and hence spring and light-weight carriage forces. Moreover, the derivation of the instantaneous thrust deduction factor requires exactly identical instantaneous ship velocity oscillations during the spring response time in bare hull and self-propulsion conditions, because even small velocity variations result in significant resistance and thrust variations, and consequently, alterations of the spring and light-weight carriage forces. Therefore, the instantaneous thrust deduction factor and wake fraction cannot be achieved in the current investigations. Instead, the averaged thrust deduction factor and wake fraction can be obtained according to the averaged values of different quantities during a time window, for instance roughly on one spring natural period T_{spring}, on which the averaged velocity of the ship remains very close to the expected ship velocity U.

Therefore, in the current paper, the mean thrust deduction factor is estimated using mean values (during the chosen time window) of total resistance $\bar{R}_T$ from the bare hull simulation together with the propeller thrust $\bar{T}$ as well as the spring force $-K\bar{x}$ and light-weight carriage force $-m_3\ddot{\bar{x}}$ from the self-propulsion simulation. The mean value of the ship velocity during the same time window remains very close to U in both BH and SP conditions, which justifies the derivation of the mean thrust deduction factor in that velocity through,

$$\bar{t} = 1 - \frac{\bar{R}_T}{\bar{T} + (-K\bar{x} - m_3\ddot{\bar{x}})}, \tag{4}$$
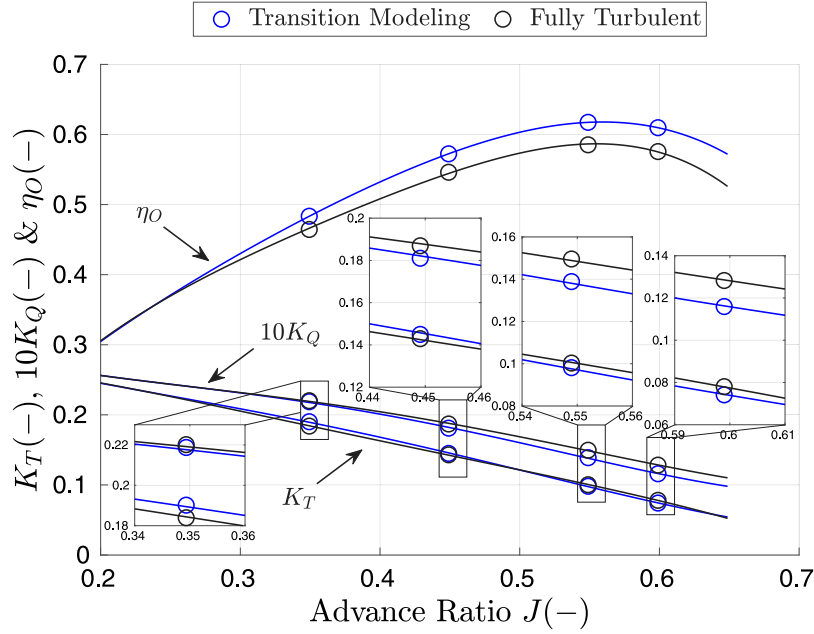
Fig. 5. Propeller open water curves, adopted from CFD investigations in calm water and regular head waves in Irannezhad et al. (2024), for fully turbulent simulations as well as simulations incorporating transition modeling.

in which $(-K\bar{x} - m_3\bar{\bar{x}})$ represents the additional force that compensates for the propeller thrust deficit/excess in SP condition at the estimated propeller rotational speed to reach model SPP. It should be noted that this additional force $(-K\bar{x} - m_3\bar{\bar{x}})$ does not influence the flow physics in the same way as the propeller thrust generation mechanism, and its consideration in this study is related to the correction of the thrust deficit/excess at the estimated propeller rotational speed. The corrected thrust, eventually, is used for the estimation of the thrust deduction factor. However, since the spring and light-weight carriage forces are relatively insignificant, their effects on the main analyses carried out in this paper are deemed inconsequential.

The mean wake fraction is obtained through the Thrust Identity Method outlined in ITTC (2021f). In the thrust identity method, the thrust from self-propulsion condition is assumed to be equal to the thrust from open water condition. According to this assumption, the propeller generates the same thrust at the same rotational speed when working behind a hull at the speed of U and in open water at a speed of advance U_A. In this study, the mean value of the propeller thrust coefficient $\bar{K}_T$, based on self-propulsion mean thrust $\bar{T}$ in Eq. (2), in conjunction with the propeller open water curves in Fig. 5 (adopted from Irannezhad et al., 2024) are employed to carry out the procedure proposed in the thrust identity method. Consequently, the thrust coefficient from the self-propulsion condition $\bar{K}_T$ is used to extract advance ratio $\bar{J}_T$, open water torque coefficient $\bar{K}_{Q_O}$ and open water efficiency $\bar{\eta}_O$ from the propeller open water curves. Thereafter, the effective wake fraction (Taylor wake fraction $\bar{w}_T$ in Taylor notation, ITTC (2021a)) is calculated as,

$$\bar{w}_T = 1 - \frac{\bar{J}_T nD}{U}. \tag{5}$$

Then the hull efficiency $\bar{\eta}_H$ and the relative rotative efficiency $\bar{\eta}_R$ are derived as,

$$\bar{\eta}_H = \frac{1 - \bar{t}}{1 - \bar{w}_T}, \qquad \bar{\eta}_R = \frac{\bar{K}_{Q_O}}{\bar{K}_Q}, \tag{6}$$

and consequently, the propulsive efficiency $\bar{\eta}_D$ is obtained from,

$$\bar{\eta}_D = \bar{\eta}_O \bar{\eta}_H \bar{\eta}_R. \tag{7}$$

The flow over each propeller blade can be a combination of laminar, transitional and turbulent flow (Baltazar et al., 2021). Although in

self-propulsion conditions, a fully turbulent regime is expected for the flow over the propeller blades in full-scale, one lingering question in ship hydrodynamics revolves around whether or not the flow regime in model-scale consists of transition from laminar to turbulent flow. The available literature on this subject is scarce. In the investigations by Hasuike et al. (2017), laminar flow separation was observed by oil flow visualizations (paint tests) in calm water self-propulsion model tests. The propeller incident wake behind the hull, especially for the high block coefficient hulls as of KVLCC2, may raise the possibility of a fully turbulent flow regime in self-propulsion condition in model-scale. This is even more likely under self-propulsion condition in regular head waves due to more significant and unsteady ship motions. Overall, the evaluation of the flow regime characteristics over the propeller blades in self-propulsion model-scale condition may be highly intricate, as there are several influencing factors involved, such as propeller geometry, rotational speed and the incident wake behind the hull as a result of hull geometry and motions as well as the wave orbital velocities.

In the POW investigations in Irannezhad et al. (2024) for the same propeller under study in this paper, laminar flow dominance (transition phenomenon) has been observed in some operational conditions in calm water, whereas in regular head waves, the unsteady and oblique flow characteristics of the incident waves (induced by the wave orbital velocities) implied increased turbulence. In the case of self-propulsion in the current study, there is an essential difference compared to POW, as the propeller works at the wake behind the hull, hence potentially leading to a fully turbulent regime, even in calm water, but it is not certainly the case in every operational condition.

Due to the lack of information about the flow regime in the current self-propulsion conditions, the flow is presumed to be fully turbulent in calm water and regular head waves simulations. Nonetheless, an additional self-propulsion simulation carried out in calm water using the $\gamma - Re_\theta$ transition model, i.e., the same model that has been employed for the POW investigations in Irannezhad et al. (2024), to gain a brief insight into the potential consequences.

The analysis of the results mainly concerns the self-propulsion simulations in calm water and regular head waves with fully turbulent flow regime considerations. However, two sets of propeller open water curves, one from fully turbulent simulations and another from

simulations incorporating a transition model, are provided in Fig. 5. In the applied thrust identity method, only the fully turbulent propeller open water curves are used in regular head waves, while both the fully turbulent and transition modeling propeller open water curves are employed in calm water for a brief comparison.

As mentioned before, the propulsive factors are derived from the mean values of different quantities during the chosen time window. However, two important considerations are associated with the post-processing techniques.

Firstly, the oscillations of different time series are significantly affected by the behavior of the spring system and hence instantaneous surge motion and ship velocity. Due to extremely high computational power requirements for self-propulsion simulations, it is not feasible to reach an ideal state of spring system behavior within the scope of the current study. Therefore, the time window for post-processing is chosen once a reasonable state of the spring system is obtained, which may introduce uncertainties into the achieved results.

Secondly, the oscillations in the time series of each studied quantity consist of three primary groups of frequencies. The first group of frequencies is related to the propeller revolution, where the involved frequencies represent the multiples of the blade passing frequency ω_b. The blade passing frequency can be described through the number of blades times the propeller frequency ω_p, thus $\omega_b = 4\omega_p = 4\Omega$. It should be noted that the most significant oscillations of the single-blade thrust and torque time series occur at the propeller frequency ω_p, whereas the oscillations of the total thrust and torque time series (on all blades and the hub cap) are in the blade passing frequency ω_b. The second group of frequencies is related to the spring behavior, where the involved frequencies are representing the multiples of the spring natural frequency ω_{spring}. Finally, the third group of frequencies is related to the incident waves, where the involved frequencies are the multiples of the wave encounter frequency ω_E. The oscillations of time series in calm water only concern the first and second groups of frequencies, whereas, in regular head waves, all three groups are incorporated in the measured quantities. It is worth mentioning that the oscillations in the blade passing frequency group are significant in the thrust and torque time series, but negligible in the ship velocity and motions time series.

Therefore, a Fourier analysis, using the Fast Fourier Transform (FFT), is performed on the chosen time window to obtain an insight into the behavior of different time series. The Fourier analysis results of each quantity under study $\psi(t)$ reads as follows,

$$
\begin{aligned}
\psi(t) = &\bar{\psi} + \psi_{1b}\cos(\omega_b t + \psi_{\varepsilon 1b}) + \psi_{2b}\cos(2\omega_b t + \psi_{\varepsilon 2b}) \\
&+ \psi_{3b}\cos(3\omega_b t + \psi_{\varepsilon 3b}) + \cdots \\
&+ \psi_{1s}\cos(\omega_{spring} t + \psi_{\varepsilon 1s}) + \psi_{2s}\cos(2\omega_{spring} t + \psi_{\varepsilon 2s}) \\
&+ \psi_{3s}\cos(3\omega_{spring} t + \psi_{\varepsilon 3s}) + \cdots \\
&+ \psi_{1E}\cos(\omega_E t + \psi_{\varepsilon 1E}) + \psi_{2E}\cos(2\omega_E t + \psi_{\varepsilon 2E}) \\
&+ \psi_{3E}\cos(3\omega_E t + \psi_{\varepsilon 3E}) + \cdots,
\end{aligned}
\tag{8}
$$

in which $\bar{\psi}$ is the mean value, but ψ_{ib}, ψ_{is} and ψ_{iE} are the ith harmonic amplitudes, and $\psi_{\varepsilon ib}$, $\psi_{\varepsilon is}$ and $\psi_{\varepsilon iE}$ are the ith harmonic phase components, respectively in the blade passing frequency ω_b, spring natural frequency ω_{spring} and wave encounter frequency ω_E.

A good choice of post-processing time window in calm water condition is one spring natural period $T_{spring} \approx 11.256$ s. However, in regular head waves, since the harmonic amplitudes of surge, heave and pitch in the wave encounter frequency are dominant, a good choice of time window is a multiple of wave encounter period T_E in each wave length condition, in order to minimize the spectral leakage in the Fourier analysis. On the other hand, the harmonic amplitudes of surge and instantaneous velocity in the spring natural frequency are significant. Therefore, to include both effects, the post-processing time window in each regular head wave condition is chosen as a multiple of the wave encounter period which is closest to one spring natural period. The time windows in regular waves $\lambda/L = 0.6$, 1.1 and 1.6 are respectively,

$15T_E \approx 11.39$ s, $10T_E \approx 11.20$ s and $8T_E \approx 11.30$ s. The chosen time window in each condition is very close to the spring natural period, hence the difference of the mean values of each quantity is negligible between averaging over the chosen time window and averaging over one spring natural period. It is worth mentioning that the same time windows were also chosen in the bare hull investigations in Irannezhad et al. (2023).

The simulations should converge in each time step as well as statistically for a reliable time period in order to perform a valid post-processing practice on the results. According to the recommendations in ITTC (2014a), the convergence can be evaluated via the observation of the mass and momentum equations residuals as the deviations of the current estimated solution from the ideal mass and momentum conservation. The conservative choice of 20 internal iterations per time step in the current study may justify the convergence in each time step. However, due to the complexity of the problem under study, the residuals exhibit an oscillatory behavior during the time. Moreover, the residuals are not directly linked to the engineering quantities, such as thrust and torque. Therefore, in this study, apart from the residual monitor, the convergence is evaluated by analyzing a reliable time window (from the tail of signals) of the thrust and torque time series in the simulations.

4.5.1. Convergence criterion for calm water simulations

As mentioned before, the tail of the thrust and torque time series are analyzed to evaluate the convergence of the calm water simulation. Since the thrust and torque time series oscillate in the blade passing frequency, the convergence evaluation is performed on the "periodic moving averaged time series", in which the value at each instance of time is the averaged value of the original time series on a moving window of one blade passing time period $1T_b$ before that instance of time. A representative plot of the original and periodic moving averaged time series is shown in Fig. 6. The horizontal axis displays the offset time, focusing solely on the tail of the computed signal while excluding the initial segment.

A calm water simulation is deemed converged when the Standard Deviation (STD) of the periodic moving average of the thrust and torque time histories is below 1% of its Root Mean Square (RMS) for the chosen time window of the signal tail (one spring natural period T_{spring}). If STD%RMS < 1 for both thrust and torque, then the simulation is deemed converged and the original time series of different quantities are analyzed over the chosen time window.

4.5.2. Convergence criterion for regular wave simulations

In Fig. 7, a representative plot is illustrated for a thrust/torque signal sample alongside its periodic moving average time series in both blade passing time period $1T_b$ and wave encounter period $1T_E$ in regular head waves simulations. The convergence is examined on the periodic moving average time series on $1T_E$, which is extracted from the original time series, where its value at each time instance is the average of the original signal values over a moving average window of $1T_E$ prior to that certain instance of time.

The convergence in regular head waves is defined as when the Standard Deviation (STD) of the periodic moving averaged signal (blue line) is lower than 1% of its Root Mean Square (RMS) over a chosen time window. If the STD%RMS < 1, then the simulation is deemed converged, and the original signal is post-processed over the chosen time window.

4.5.3. Reconstruction of time series

In order to analyze the instantaneous values of different quantities and their correlations during the ship performance, the reconstructed time series are used. The reconstructed time series of different quantities are derived during particular time periods depending on the purpose of the analysis. The dominant harmonic components (HC), i.e., harmonic amplitudes (HA) and harmonic phases, from the FFT
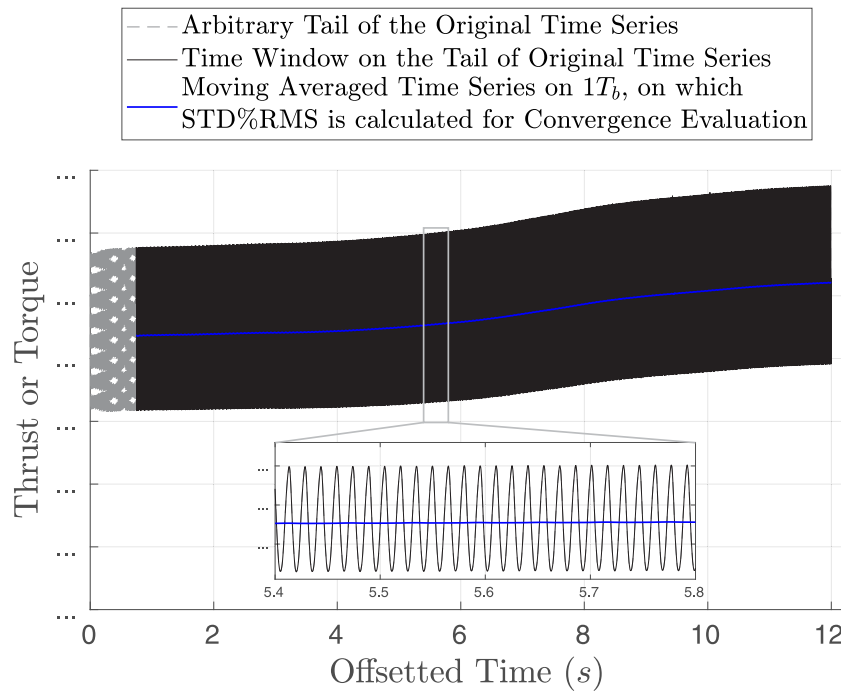
Fig. 6. A representative thrust/torque time series tail together with its periodic moving average for explaining the convergence criteria in calm water.
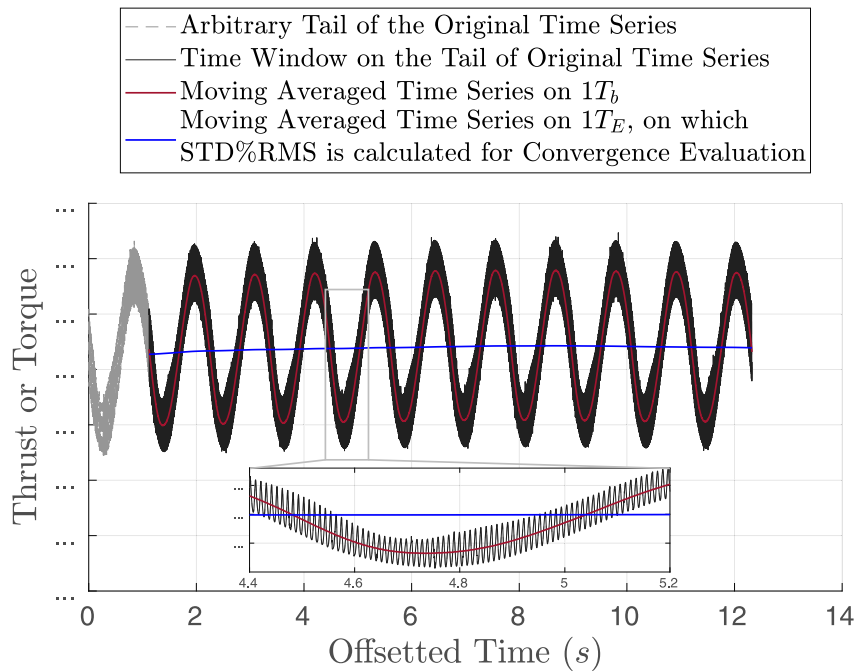

Fig. 7. A representative thrust/torque time series tail together with its periodic moving average on wave encounter period and blade passing time period for explaining the convergence criteria in regular head waves.

results in Eq. (8), are employed for the reconstruction of the time series. These dominant harmonic amplitudes in different groups of oscillation frequencies are presented for each quantity of interest. The origin of time $t/T_E = 0$ in the reconstructed time series is defined differently in the presented results which are explained in Sections 5 and 6.

It is worthwhile to mention that in regular head waves, the intricate physical factors involved make it challenging to accurately reconstruct the predominant oscillations of various quantities solely based on the aforementioned set of frequencies. This is because the dominant harmonic amplitudes in each of these frequencies may exhibit

variations over time during the wave encounter. Therefore, instead of reconstructed time series, a $1T_E$ window of the original time series (which includes the instantaneous spring effects in that period of time) is adopted for the presentation of the results during one encounter period in regular head waves.

5. Calm water results

In this section, the computed self-propulsion performance of the ship in calm water at $n = 16.50$ rps in free surge condition (3DOF) is an-

(a) Thrust.   (b) Torque.
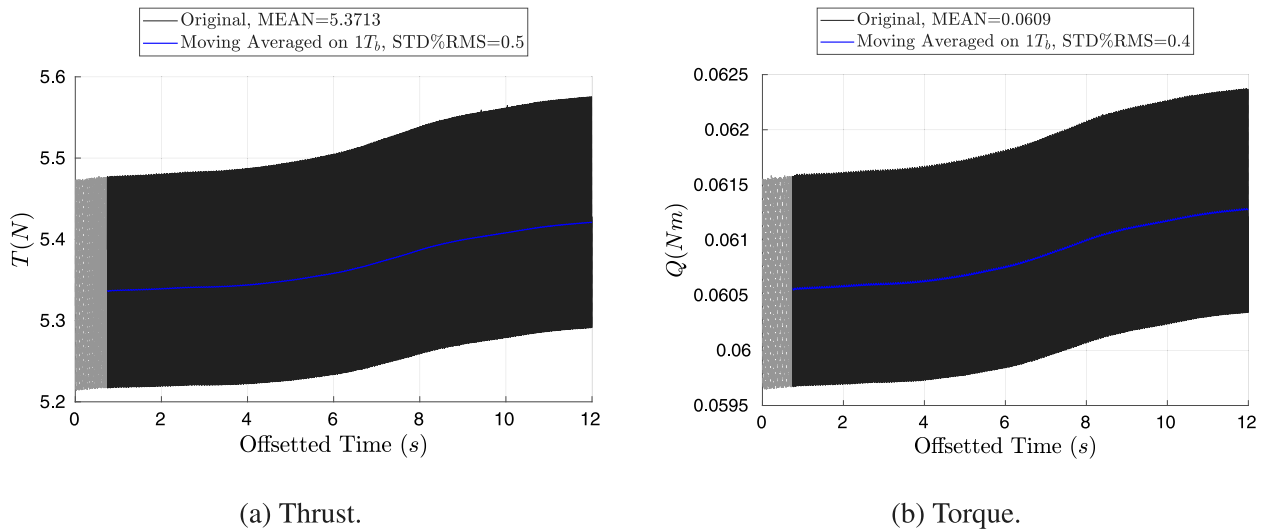
Fig. 8. Original and periodic moving average of the thrust and torque time series tail in calm water self-propulsion simulation at $n = 16.50$ rps.

alyzed and compared with the respective experimental measurements in fixed surge condition (2DOF). The relevant results from the bare hull investigation in Irannezhad et al. (2023) and POW investigation in Irannezhad et al. (2024) are combined with the self-propulsion simulation results from the current study to analyze the propeller-hull interaction effects on propulsion characteristics of the ship. In order to be consistent with the current self-propulsion simulation configurations, the results from the bare hull and POW simulations with the similar grid (indicated by the refinement level of 1.00 in Irannezhad et al. (2023) and Irannezhad et al. (2024)) are adopted.

5.1. Convergence evaluation

The calm water simulation convergence criterion, provided in Section 4.5.1, is fulfilled as it is shown in Fig. 8, where STD%RMS = 0.5 and 0.4 for the moving averaged thrust and torque time series, respectively.

In calm water, the considered propeller rotational speed in EFD is identical to the estimated propeller rotational speed at the model SPP, given in Table 2. The same propeller speed is used in the CFD simulation presented in this section, therefore, the generated thrust from the propeller is anticipated to yield a near-to-zero mean surge motion during one spring natural period in CFD, while the mean value of the ship instantaneous velocity over the same time window remains very close to the expected ship velocity U. In Fig. 9, the spring and light-weight carriage forces time series from CFD in calm water are shown which also outline the instantaneous surge motion and acceleration of the ship. For a clearer illustration of the results, only the tail of the time series (last 12 s with offset time in horizontal axis) from the simulation is presented. The mean value of each respective quantity over one spring natural period (i.e., the last $T_{spring} \approx 11.256$ s of the time series shown with solid black line) is presented in the legend of each plot.

The mean value of surge motion over T_{spring} is approximately $\bar{x} = -0.0013$ m resulting in the mean spring force of $-K\bar{x} = 0.1250$ N, while the instantaneous $-Kx$ oscillates between relatively larger values. On the other hand, the light-wight carriage force is almost negligible in comparison to the spring force, both in terms of the mean value and instantaneous values. The time series of $-m_3\ddot{x}$ exhibit oscillations in the spring natural frequency ω_{spring} as well as the blade passing frequency ω_b.

The oscillatory behavior in the spring natural frequency and the blade passing frequency is also present in the thrust and torque time series, seen in Fig. 8. Although the oscillations in the blade passing

frequency for thrust and torque time series exhibit a harmonic behavior with almost consistent harmonic amplitudes and phases, the behavior of the oscillations in the spring natural frequency is not completely harmonic for the chosen time window. This is because of the similar behavior of the instantaneous spring force and ship velocity over this time window.

Ideally, the simulations should run for much longer physical time to obtain both smaller and consistent oscillations of different time series in the spring natural frequency and then choose a post-processing time window that consists of several spring natural periods. However, this is not feasible within the scope of the current study due to the extremely high required computational costs. Therefore, the current status of the simulation and the chosen time window from the simulation time series are deemed to be reasonably adequate and suitable for representation of the overall ship performance.

Consequently, the Fourier analysis is carried out on the chosen time window and the reconstructed time series of thrust and torque are shown in Fig. 10. These time series are reconstructed using up to and including the $5th$ harmonic components (harmonic amplitudes and phases) in the blade passing frequency ω_b obtained through the Fourier analysis. The mean value as well as the dominant harmonic amplitudes are provided in the legends of the plots, in which HAi_b is the ith harmonic amplitude in the blade passing frequency. The considered reconstructed time period is equivalent to the time period of one propeller revolution, i.e., also equal to the number of blades multiplied by the blade passing time period ($1/n = 4T_b$), with an arbitrary origin $t/T_b = 0$. It is clear that HA1$_b$ is the dominant harmonic amplitude, while higher harmonic amplitudes are comparatively smaller, but not negligible though.

5.2. Validation

In Table 3, the calm water simulations results are compared with the model test data. In addition to the self-propulsion (SP) simulation results, the bare hull (BH) simulation results, adopted from Irannezhad et al. (2023), are provided. There were two experimental data sets (denoted by EFD$_1$ and EFD$_2$) available for the bare hull investigations, while only one EFD data set (EFD$_2$) is available for the self-propulsion condition.

A complete analysis of the bare hull surge $\bar{x}$, heave $\bar{z}$, pitch $\bar{\theta}$ and total resistance $\bar{R}_T$ results is presented in Irannezhad et al. (2023). In self-propulsion condition, the surge motion was fixed in the model tests and cannot be compared against the computed surge in 3DOF CFD. The absolute value of the validation error $E\%D$ in SP in comparison to BH
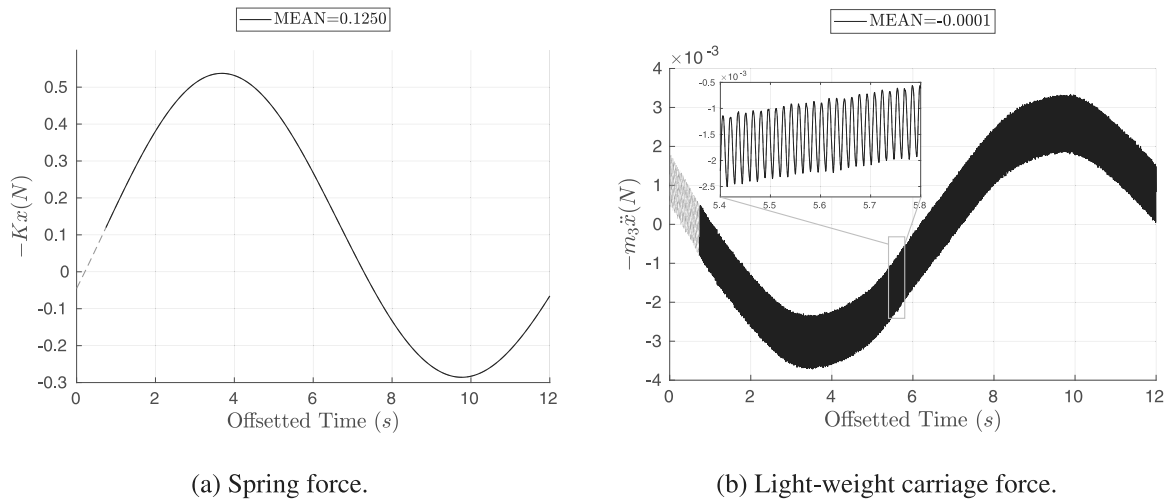
(a) Spring force.

(b) Light-weight carriage force.

Fig. 9. Tail of the time series of the spring and light-weight carriage forces in calm water self-propulsion simulation at $n = 16.50$ rps.
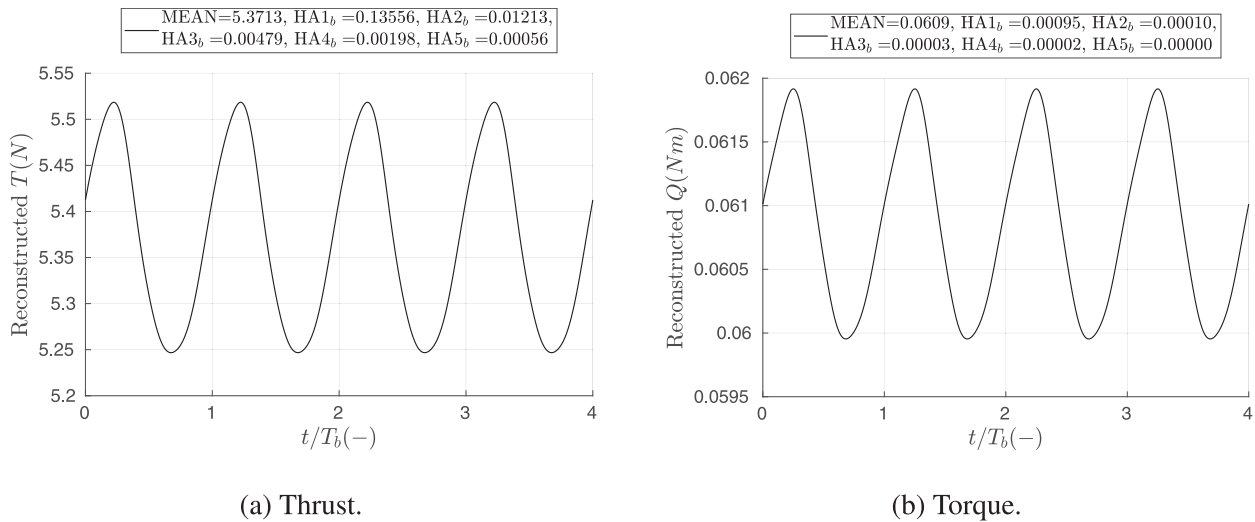

(a) Thrust.

(b) Torque.

Fig. 10. Reconstructed time series of thrust and torque during one propeller revolution in calm water self-propulsion simulation at $n = 16.50$ rps.

Table 3
Comparison between EFD and CFD in calm water in bare hull (BH) and self-propulsion (SP) conditions. The propeller rotational speed is set to $n = 16.50$ rps in SP condition.

Cond.	Data	CFD	EFD$_1$	EFD$_2$	E =CFD−EFD		$E\%D = E$/EFD×100	
					E_1	E_2	$E\%D_1$	$E\%D_2$
BH	$\bar{x}$ (m)	−0.0001	0.0124	0.0058	−0.0125	−0.0058	*	*
	$\bar{z}$ (m)	−0.0029	−0.0032	−0.0027	0.0002	−0.0002	−6.8	9.4
	$\bar{\theta}$ (deg)	0.115	0.129	0.088[a]	−0.014	0.027	−11.0	30.0
	$\bar{R}_T$ (N)	4.4189	4.394	4.440	0.024	−0.021	0.5	−0.5
SP	$\bar{x}$ (m)	−0.0013	–	**	–	**	–	**
	$\bar{z}$ (m)	−0.0033	–	−0.0028	–	−0.0005	–	18.7
	$\bar{\theta}$ (deg)	0.107	–	0.122[a]	–	−0.015	–	−12.5
	$\bar{Q}$ (Nm)	0.0609	–	0.0604	–	0.0005	–	0.8
	$\bar{T}$ (N)	5.3713	–	4.8310	–	0.5402	–	11.2

∗ $\bar{x}$ depends on F_0 and due to lack of information about F_0 in EFD, no meaningful comparison can be made.
∗∗ Surge motion was fixed in the self-propulsion model tests (EFD$_2$).
[a] Pitch motion sign from EFD$_2$ is modified here, due to inconsistency with respect to the prescribed coordinate system in Mwangi (2021). A similar modification is considered for the EFD$_2$ data in waves.

is increased for the heave motion and decreased for the pitch motion. In SP condition, the errors (discrepancies) E in terms of magnitude are insignificant (−0.0005 m for $\bar{z}$ and −0.015° for $\bar{\theta}$), similar to the BH condition. The comparison between CFD results shows a slight reduction of $\bar{z}$ (by 0.0004 m) and $\bar{\theta}$ (by 0.008°) in SP in comparison to BH, which may reflect the effects of propeller thrust as well as the local flow change in the aft ship caused by the propeller.

Although the thrust in CFD and EFD are very different (by 0.5402 N or 11.2%), the torque is similar (0.0005 Nm or 0.8%). The large error seen for $\bar{T}$ may be associated with the difference in degrees
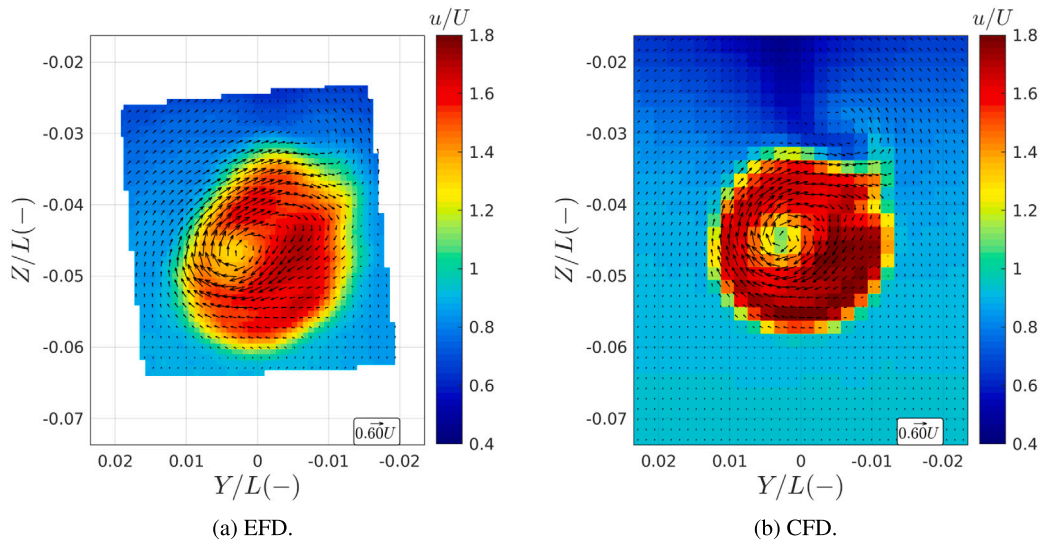
Fig. 11. Comparison of propeller slipstream velocity distribution, on the carriage-fixed propeller slipstream plane in CF_{PSP} coordinate system, between EFD and CFD in calm water self-propulsion condition at $n = 16.50$ rps.

of freedom between CFD (3DOF) and EFD (2DOF) where there was no clear information available about the force measurements at the dynamometer installed at COG (shown in Fig. 2(b)) and hence the change of the loading on the propeller in EFD. This also means that the thrust deduction factor from EFD cannot be obtained and compared with CFD.

In Fig. 11, the propeller slipstream velocity distribution on the carriage-fixed propeller slipstream plane in CF_{PSP} coordinate system (shown in Fig. 1) is compared between EFD and CFD in calm water self-propulsion condition at $n = 16.50$ rps. Approximately 230 images from SPIV measurements were collected and analyzed to present the EFD velocity distribution. The computed propeller slipstream in Fig. 11(b) is derived from averaging velocity distribution on the PSP plane, (depicted in Fig. 1), in each time step for one propeller revolution (180 time instances).

The instantaneous surge motion in CFD causes variation of the distance between the carriage-fixed PSP plane and the hull, whereas in EFD, the surge motion was fixed. This may be counted as an important source of discrepancy between EFD and CFD velocity distributions, hence solely a qualitative comparison can be made. Overall, the velocity distribution in CFD and EFD are comparable. There are also interesting similarities, particularly the large axial velocity area roughly close to $Y/L = -0.005$ and $Z/L = -0.05$ as well as a vortical structure outside the main propeller slipstream in the vicinity of $Y/L = -0.01$ and $Z/L = -0.03$ visualized by the tangential velocity vectors.

5.3. Propeller-hull interactions analysis

In Fig. 12, the tail of the time series of the instantaneous ship velocity in BH and SP simulations in calm water are shown, in which the mean values are also provided in the plot legend. As mentioned before, the SP simulation should ideally run for a much longer physical time to reach statistical convergence and obtain smaller and consistent oscillations of velocity and surge motion, similar to the BH simulation. Nevertheless, this is not feasible within the scope of the current study due to its extensive computational power requirements.

5.3.1. Propulsive factors

In Table 4, the mean values of the thrust deduction factor $\bar{t}$, Taylor wake fraction $\bar{w}_T$, hull efficiency $\bar{\eta}_H$, open water efficiency $\bar{\eta}_O$, relative rotative efficiency $\bar{\eta}_R$ and propulsive efficiency $\bar{\eta}_D$ in calm water are derived based on the procedures presented in Section 4.5. It is
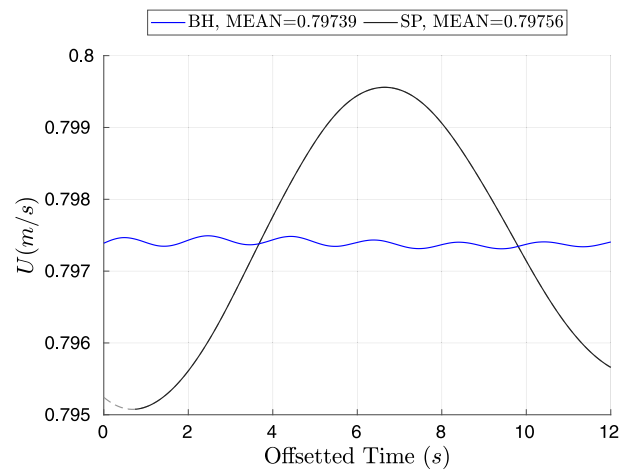
Fig. 12. Time series of the instantaneous ship velocity from CFD simulations in bare hull and self-propulsion conditions.

worth mentioning that these propulsive factors are calculated based on the model-scale CFD simulations. In calm water condition, the thrust identity method is employed using both fully turbulent and transition modeling propeller open water curves in Fig. 5.

The rather large calculated hull efficiency $\bar{\eta}_H$ may originate from the significant propeller-hull interaction effects on the propulsion performance in the highly-loaded model SPP condition. On the other hand, due to the higher loading on the propeller, the generated thrust and its corresponding $\bar{J}_T$ from the thrust identity method results in rather small propeller open water efficiency $\bar{\eta}_O$ and advance ratio. As can be perceived from the open water curves obtained from the fully turbulent flow simulation and the simulation including transition modeling (Fig. 5), at low advance velocities the difference between the two sets of curves is minute, which in turn results in a rather small impact on the propulsive factors. The impact of switching between the open water curves obtained from fully turbulent simulation or the ones including transition will be more significant at higher advance ratios.

In a brief comparison, the calm water self-propulsion simulation incorporating the $\gamma - Re_\theta$ transition model yields rather similar thrust and torque to the ones presented here for the fully turbulent simulation. The predicted thrust and torque from the simulation with transition

Table 4
Propulsive factors and corresponding quantities derived from CFD simulations in calm water. The propeller rotational speed of $n = 16.50$ rps is considered in SP condition which represents the model SPP.

Cond.	BH	SP ($n = 16.50$ rps)						
Calm	$\bar{R}_T$ (N)	$-\bar{K}\bar{x}$ (N)	$-m_3\bar{\dot{x}}$ (N)	$\bar{T}$ (N)	$\bar{Q}$ (Nm)	$\bar{P}_D$ (W)	$10\bar{K}_Q$ (–)	$\bar{K}_T$ (–)
	4.4189	0.1250	−0.0001	5.3713	0.0609	6.3096	0.2403	0.2091
	BH & SP	Thrust Identity Method (Transition Modeling Open Water Curves)						
	$\bar{t}$ (–)	$\bar{J}_T$ (–)	$\bar{w}_T$ (m)	$10\bar{K}_{Q_O}$ (–)	$\bar{\eta}_O$ (–)	$\bar{\eta}_H$ (–)	$\bar{\eta}_R$ (–)	$\bar{\eta}_D$ (–)
	0.1960	0.2988	0.3904	0.2317	0.4287	1.3190	0.9639	0.5451
		Thrust Identity Method (Fully Turbulent Open Water Curves)						
		$\bar{J}_T$ (–)	$\bar{w}_T$ (m)	$10\bar{K}_{Q_O}$ (–)	$\bar{\eta}_O$ (–)	$\bar{\eta}_H$ (–)	$\bar{\eta}_R$ (–)	$\bar{\eta}_D$ (–)
		0.2908	0.4068	0.2339	0.4125	1.3552	0.9734	0.5442
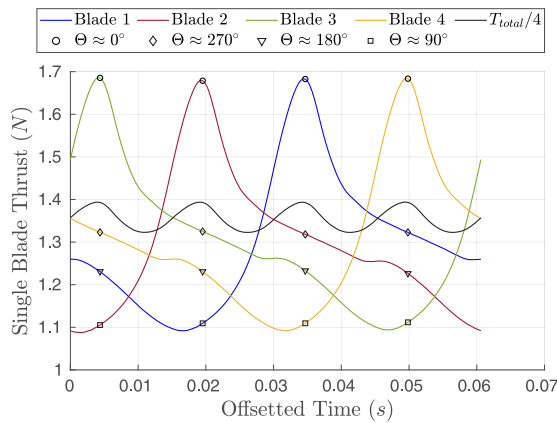
(a) Single-blade thrust.
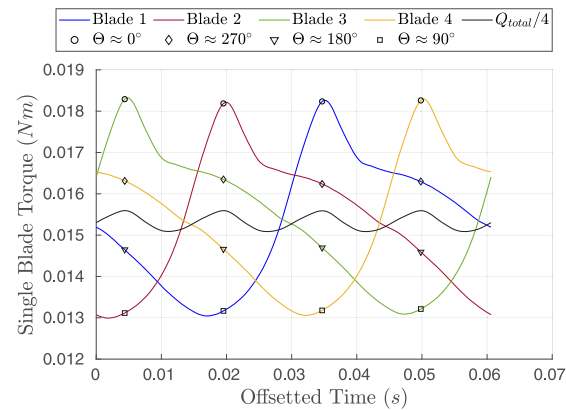
(b) Single-blade torque.

Fig. 13. Time series of the total (blades and hub cap) and individual blades thrust and torque during the last propeller revolution in calm water simulation at $n = 16.50$ rps.

model are approximately 0.3% (0.0162 N) and 2.3% (0.0014 Nm) lower than the thrust and torque from the fully turbulent simulation, which may justify the fully turbulent flow regime assumption in calm water self-propulsion simulation in this paper. Most probably, the small difference between the fully turbulent self-propulsion simulation and the simulation including the transition model is a result of a rather low propeller advance ratio at this speed (around 0.3). As shown in Irannezhad et al. (2024) the predicted propeller performance with and without considering the flow transition is almost the same at lower advance ratios while the difference becomes more significant at higher advance ratios according to the studied operational conditions for the current propeller. Nonetheless, the discussion will remain open on the actual flow regime, due to the lack of information about the actual turbulence level in calm water self-propulsion condition in this study.

5.3.2. Single-blade analysis

The contribution of each blade as well as the total (all blades and hub cap) thrust and torque during the last propeller revolution in the calm water simulation at $n = 16.50$ rps are shown in Fig. 13.

During one propeller revolution, each blade exhibits larger values of thrust and torque in the vicinity of the azimuthal position $\Theta \approx 0°$. It should be noted that based on the definition of the propeller coordinate system, the propeller revolution is in the decreasing direction of the azimuthal position, as depicted in Fig. 1, i.e., from $\Theta \approx 0°$ to $\Theta \approx 270°$, $\Theta \approx 180°$, $\Theta \approx 90°$ and then again $\Theta \approx 0°$.

Since the blades are numbered sequentially in the propeller rotational direction, thus, for the right-handed propeller, the maximum values of each blade thrust and torque occur in the reverse order of blade numbers during the provided time period. These maximum values of thrust and torque for each blade cause a peak in the total thrust and torque time series, whereas the minimum values of the total thrust and torque time series do not coincide with the minimum thrust and torque from each blade.

At the approximate time instance of maximum loading on blade 1 at the approximate azimuthal position $\Theta \approx 0°$ ($t \approx 0.034$ s), the contributions of different blades on total thrust and torque are provided in Fig. 14, in which each blade is colored with a single value representing its total contribution.

It is worth mentioning that during the propeller revolution, the contribution of the hub cap thrust remains approximately close to 0.119 N, whereas the hub cap torque is negligible and almost equal to zero. As mentioned before, the oscillations of the single-blade thrust and torque time series are mainly in the multiples of the propeller frequency ω_p. Fourier analysis of these time series reveals the significance of higher harmonic amplitudes (approximately up to the 7th harmonic amplitude in the propeller frequency ω_p, denoted by HAi_p) apart from the dominant $HA1_p$.

The hydrodynamic pressure, magnitude of wall shear stress and non-dimensional wall distance y^+ over the pressure side and suction side of the blades at the time of maximum thrust and torque for blade 1 at the approximate azimuthal position $\Theta \approx 0°$ ($t \approx 0.034$ s) are shown in Fig. 15.

For blade 1 at $\Theta \approx 0°$, the larger area with lower hydrodynamic pressure values on the suction side and the larger area with higher hydrodynamic pressure values on the pressure side, in the vicinity of the blade leading edge and close to the propeller tip, may justify the high thrust generated from this blade. Similarly, for this blade, the higher magnitudes of the wall shear stress, particularly near the blade tip, may be one of the important factors that contributed to the higher torque on this blade. Finally, the non-dimensional wall distance remains approximately $y^+ < 1$ over the main part of the propeller geometry and hub cap. On the other hand, $y^+ > 30$ for the major part of the hull wetted surface area in Fig. 16 in calm water simulation. The surface-averaged $\bar{y}^+$ value on the hull wetted surface area is about 99, but on the propeller and hub cap is approximately 0.16.
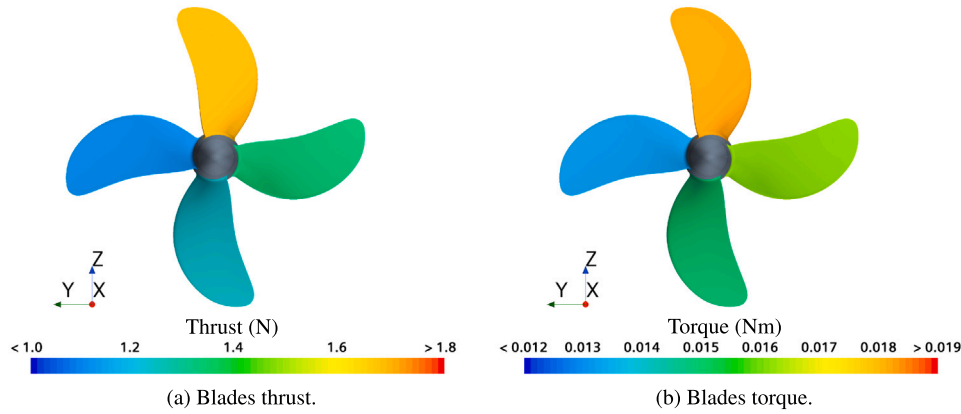
Fig. 14. Blades loading at approximate time instance of maximum thrust and torque for blade 1 (approximate azimuthal position $\Theta \approx 0°$, $t \approx 0.034$ s) in calm water simulation at $n = 16.50$ rps.

In Fig. 17, the vortical structures, obtained by two different Q-criterion iso-surface values, are shown near the propeller at the time of maximum thrust and torque for blade 1 ($t \approx 0.034$ s) in the calm water simulation. In Fig. 17(a), the larger value of Q-criterion iso-surface shows the strongest vortices, mainly originating from the blade tip and hub cap. On the other hand, the smaller vortices are also revealed by smaller Q-criterion iso-surface value in Fig. 17(b), which demonstrates the bilge vortex being ingested into the propeller. Moreover, a separate vortex development is observed at the top part of the main propeller slipstream on the starboard side, as also seen in Fig. 11. The vortical structure emerges from the interplay between the swirl generated by the propeller and the low-speed boundary layer in the uppermost part of the hull wake. It rotates counter to the direction of the propeller slipstream (propeller rotation direction). As previously shown in Fig. 15, the blade tip loading is relatively high when the blade passes $\Theta \approx 0°$, where the combination of the minimum axial velocity into the propeller and the increased transversal velocity induced by the bilge vortex increases the apparent incident angle of the flow over the blade which in turn results in increased blade loading. The temporal increased blade loading in combination with the low momentum flow around this blade position can be the reason behind the formation of the new vortical structure observed above the propeller slipstream.

6. Regular wave results

In this section, the computed self-propulsion performance of the ship in regular head waves, presented in Table 2, is analyzed. The analysis consists of a validation of the CFD results in $\lambda/L = 1.1$ at the propeller rotational speed of $n = 16.5$ rps against the corresponding experimental model test, and then a thorough investigation of the ship performance at model SPP using solely the CFD results in other operational conditions in Table 2. Similar to the calm water studies, the self-propulsion investigations in the current study are combined with the bare hull investigation in Irannezhad et al. (2023) and POW investigation in Irannezhad et al. (2024), employing similar grids, to derive the propulsive factors of the ship at the model SPP in regular head waves.

6.1. Validation

The validation of the CFD results in $\lambda/L = 1.1$ at the propeller rotational speed of $n = 16.5$ rps are presented in this section. Prior to the comparison between EFD and CFD, the convergence criterion is examined for the CFD thrust and torque in Fig. 18, based on the criterion explained in Section 4.5.2. The value of STD%RMS for the periodic moving average of the thrust and torque time series is around 0.3 over the chosen time window in this wave length, which fulfills the

defined convergence criterion. The mean values of the original signals over the chosen time window are also presented in the legend of each plot.

As mentioned before, an estimated $F_0 = 6.86$ is used in CFD, as there is no information available for the applied F_0 in EFD. Therefore, the mean value of surge motion cannot be compared, and hence, the spring force and the propulsive factors are not derived. In Fig. 19, the time series of the spring force as well as the instantaneous ship velocity and light-weight carriage force from the CFD simulation is shown.

Similar to calm water, the mean value of the light-weight carriage force (given in the plot legend) is negligible, whereas the mean value of the spring force is significant. The mean value of the ship velocity over the chosen time window is rather close to the expected ship velocity U.

In Table 5, the CFD results of the mean surge, heave and pitch as well as the mean bare hull total resistance and mean self-propulsion thrust and torque in $\lambda/L = 1.1$ at $n = 16.50$ rps are compared against the EFD data. An extensive comparison between EFD and CFD for the bare hull results is provided in Irannezhad et al. (2023). The validation errors for mean heave and pitch in self-propulsion are rather large and similar to the ones in the bare hull condition. Nonetheless, the errors are relatively small when the differences in terms of magnitude are compared. The validation error for the bare hull total resistance is roughly similar to the errors seen for the mean thrust and torque.

In Table 6, the dimensional and non-dimensional 1st harmonic amplitudes of motions in the wave encounter frequency, as the dominant component, are compared between EFD and CFD in both BH and SP conditions. While the analytical wave amplitude is used to non-dimensionalize the CFD results, the actual measured wave amplitude from each respective model test is used for EFD data. Similar to what has been seen in BH (discussed thoroughly in Irannezhad et al. (2023)), the average absolute error $\overline{|E\%D|}$, computed from averaging the absolute of errors for three motions, slightly decreases for the non-dimensional quantities in comparison to the dimensional ones in SP condition. Although $\overline{|E\%D|}$ is very similar between BH and SP, the absolute value of surge error $|E\%D|$ is reduced in SP condition while it is increased for heave and pitch, leading to similar average absolute errors. The largest discrepancies are seen for the 1st harmonic amplitude of pitch motion (26.9% corresponding to 0.377°) in SP condition, but reduced when the effects of actual measured wave height in the model test is taken into account, revealing the importance of actual measured wave height in the ship behavior. Overall, when the differences are analyzed in terms of magnitude, the discrepancy is mostly rather low.

The reconstructed time series (considering solely the dominant harmonic amplitudes in the wave encounter frequency) of free surface elevation, heave, pitch, thrust and torque are compared between CFD and EFD in Fig. 20. These time series demonstrate the discrepancies
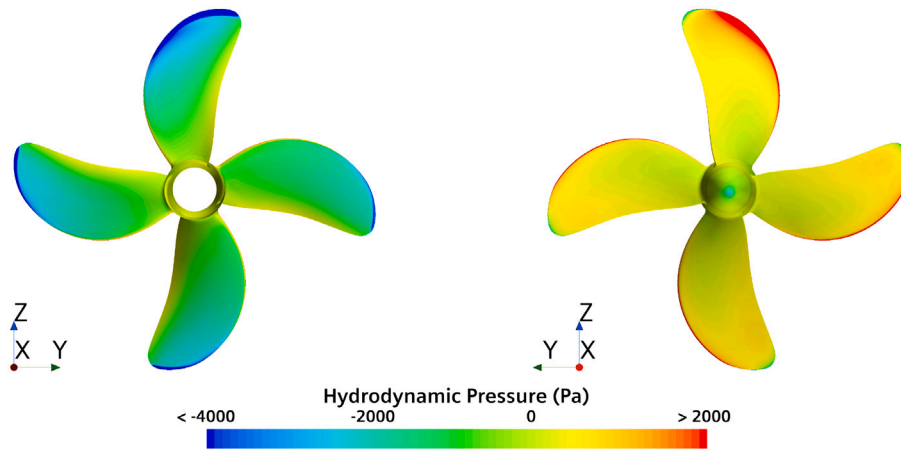
(a) Hydrodynamic pressure on suction side (left) and pressure side (right).
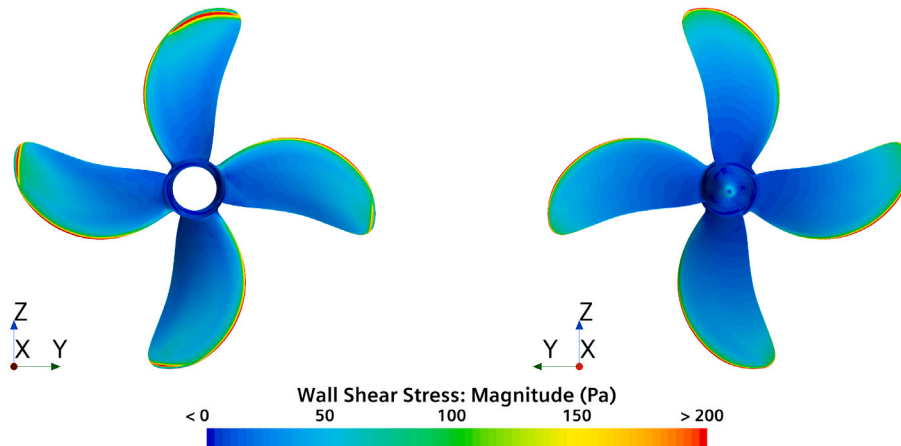
(b) Magnitude of wall shear stress on suction side (left) and pressure side (right).
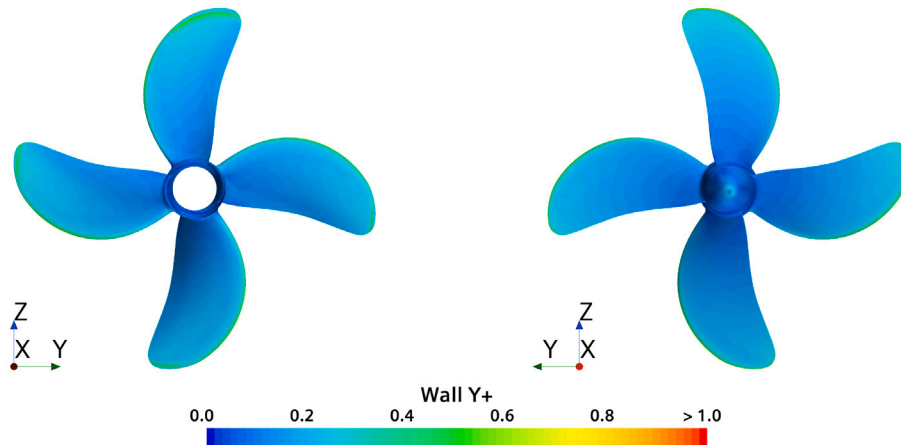
(c) Non-dimensional wall distance y^+ on suction side (left) and pressure side (right).

Fig. 15. Hydrodynamic pressure, magnitude of wall shear stress and non-dimensional wall distance y^+ over suction side and pressure side of the propeller at approximate time instance of maximum thrust and torque for blade 1 (approximate azimuthal position $\Theta \approx 0°$, $t \approx 0.034$ s) in calm water simulation at $n = 16.50$ rps.

of mean and harmonic amplitudes observed in Tables 5 and 6 as well as the harmonic phase deviations between EFD and CFD. It should be noted that the oscillations in the blade passing frequency are filtered out in the reconstructed thrust and torque time series.

The origin $t/T_E = 0$ of the reconstructed time series is taken as when the wave crest is at the original position of the ship fore perpendicular. The reconstructed time period of $1T_E$ is considered, consequently the oscillations in the spring natural frequency cannot be perceived. The

potential difference between the considered F_0, and hence the mean surge in EFD and CFD, can significantly affect the harmonic phases in these time series. This is due to the consideration of the initial position of the ship fore perpendicular as the origin of time and offsetting the time origin based on the free surface elevation derived from the carriage-fixed wave gauge measurements in EFD and the carriage-fixed probe monitor in CFD. The ship moves around its original position in the longitudinal direction based on its surge motion and since the

Table 5
Comparison of the mean values of motions and forces between EFD and CFD in regular head wave $\lambda/L = 1.1$ in bare hull (BH) and self-propulsion (SP) conditions. The propeller rotational speed is set to $n = 16.50$ rps in SP condition.

Cond.	Data	CFD	EFD$_1$	EFD$_2$	E =CFD−EFD		$E\%D = E/\text{EFD}\times100$	
					E_1	E_2	$E\%D_1$	$E\%D_2$
BH	$\bar{x}$ (m)	−0.0088	0.0708	−0.0165	−0.0795	0.0077	*	*
	$\bar{z}$ (m)	−0.0035	−0.0024	−0.0030	−0.0010	−0.0005	44.6	16.0
	$\bar{\theta}$ (deg)	0.131	0.089	0.319^a	0.042	−0.188	47.3	−58.9
	$\bar{R}_T$ (N)	11.1856	10.390	10.180	0.796	1.006	7.7	9.9
SP	$\bar{x}$ (m)	−0.0011	–	*	–	*	–	*
	$\bar{z}$ (m)	−0.0035	–	−0.0029	–	−0.0006	–	22.2
	$\bar{\theta}$ (deg)	0.120	–	0.381^a	–	−0.261	–	−68.5
	$\bar{Q}$ (Nm)	0.0601	–	0.0643	–	−0.0042	–	−6.6
	$\bar{T}$ (N)	5.2826	–	4.8015	–	0.4811	–	10.0

* $\bar{x}$ depends on F_0 and due to lack of information about F_0 in EFD, no meaningful comparison can be made.

^{a} Pitch motion sign from EFD$_2$ is modified here, due to inconsistency with respect to the prescribed coordinate system in Mwangi (2021).

Table 6
Comparison of the motions 1st harmonic amplitudes (in the wave encounter frequency) in dimensional and non-dimensional (using measured A in EFD but analytical A in CFD) forms between EFD and CFD in regular head wave $\lambda/L = 1.1$ in bare hull (BH) and self-propulsion (SP) conditions. The propeller rotational speed is set to $n = 16.50$ rps in SP condition.

Cond.	Data	CFD	EFD$_1$	EFD$_2$	E =CFD−EFD		$E\%D = E/\text{EFD}\times100$	
					E_1	E_2	$E\%D_1$	$E\%D_2$
BH	x_1 (m)	0.0022	0.0022	0.0026	0.0000	−0.0004	1.0	−14.4
	z_1 (m)	0.0217	0.0199	0.0198	0.0018	0.0019	9.1	9.4
	θ_1 (deg)	1.791	1.523	1.497	0.268	0.294	17.6	19.6
	$\overline{\|E\%D\|}$						9.2	14.5
	x_1/A (–)	0.0733	0.0744	0.0871	−0.0011	−0.0138	−1.5	−15.9
	z_1/A (–)	0.7224	0.6791	0.6722	0.0433	0.0502	6.4	7.5
	θ_1/kA (–)	0.584	0.509	0.497	0.075	0.087	14.6	17.5
	$\overline{\|E\%D\|}$						7.5	13.6
SP	x_1 (m)	0.0022	–	0.0023	–	−0.0001	–	−3.3
	z_1 (m)	0.0210	–	0.0184	–	0.0027	–	14.5
	θ_1 (deg)	1.780	–	1.403	–	0.377	–	26.9
	$\overline{\|E\%D\|}$						–	14.9
	x_1/A (–)	0.0744	–	0.0790	–	−0.0046	–	−5.8
	z_1/A (–)	0.7015	–	0.6289	–	0.0725	–	11.5
	θ_1/kA (–)	0.580	–	0.469	–	0.111	–	23.6
	$\overline{\|E\%D\|}$						–	13.6
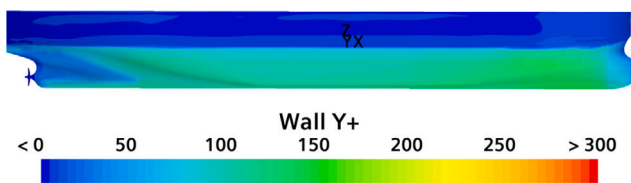
Fig. 16. Non-dimensional wall distance y^+ on the hull at $t \approx 0.034$ s in calm water simulation at $n = 16.50$ rps.

measurements equipment as well as CFD computed motions concern the ship COG, there might be a phase difference between the carriage-fixed wave extraction and the instantaneous position of the ship fore perpendicular.

In Fig. 20(a), the analytical waves at the initial position of the ship fore perpendicular as well as the initial position of the propeller center are shown. Moreover, the time instances of SPIV measurements are indicated by vertical dashed lines. The aforementioned potential discrepancies between EFD and CFD for the considered F_0 and the instantaneous surge motion can lead to the variation of the carriage-fixed planes longitudinal position with respect to the hull and the introduction of uncertainties to the SPIV time instances. Consequently, solely a qualitative comparison, in Figs. 21 and 22, is carried out for the propeller slipstream velocity distribution between EFD and CFD on the carriage-fixed propeller slipstream plane (PSP) in CF_{PSP} coordinate system (outlined in Fig. 1).

As reported in Fig. 20(d), the CFD thrust is higher than the EFD thrust throughout the entire wave encounter period. This means that the propeller accelerates the flow more in CFD in comparison to EFD which might be the reason for the slightly higher velocity obtained from CFD at the propeller slipstream in comparison to EFD as shown in Figs. 21 and 22.

Moreover, the differences between pitch motion in Fig. 20(c) may also contribute to the discrepancies between the vertical position of the main propeller slipstream on the carriage-fixed plane. It should be noticed that the SPIV measurements at each t/T_E represent an averaged velocity distribution on the plane from approximately 115 images, while solely one time step of the simulation is considered for the CFD velocity distribution results. Despite various aforementioned potential sources of discrepancy, the propeller slipstream velocity distribution is rather comparable between EFD and CFD.

6.2. Propeller-hull interactions analysis

The analysis of the propeller-hull interaction effects on the ship performance at the self-propulsion point of the model (model SPP) in regular head waves is presented in this section. The operational conditions presented in Table 2 at the model SPP are considered. First, the self-propulsion simulations convergence is examined and then the propeller-hull interactions in different wave conditions are compared. Additionally, the relevant calm water results are retrieved in this section enhancing the comparison with the regular head waves results.
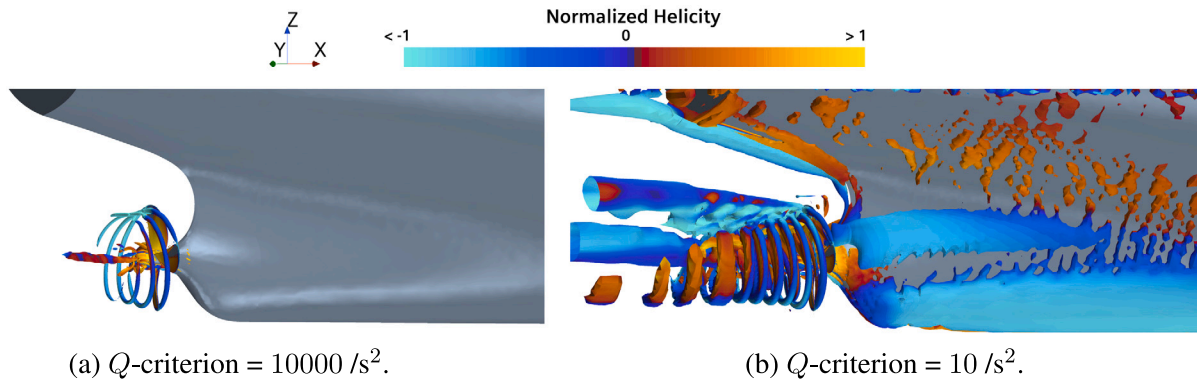
(a) Q-criterion $= 10000 \, /\text{s}^2$.   (b) Q-criterion $= 10 \, /\text{s}^2$.

Fig. 17. The vortical structures (colored by normalized helicity) found by Q-criterion at $t \approx 0.034$ s in the calm water simulation at $n = 16.50$ rps.
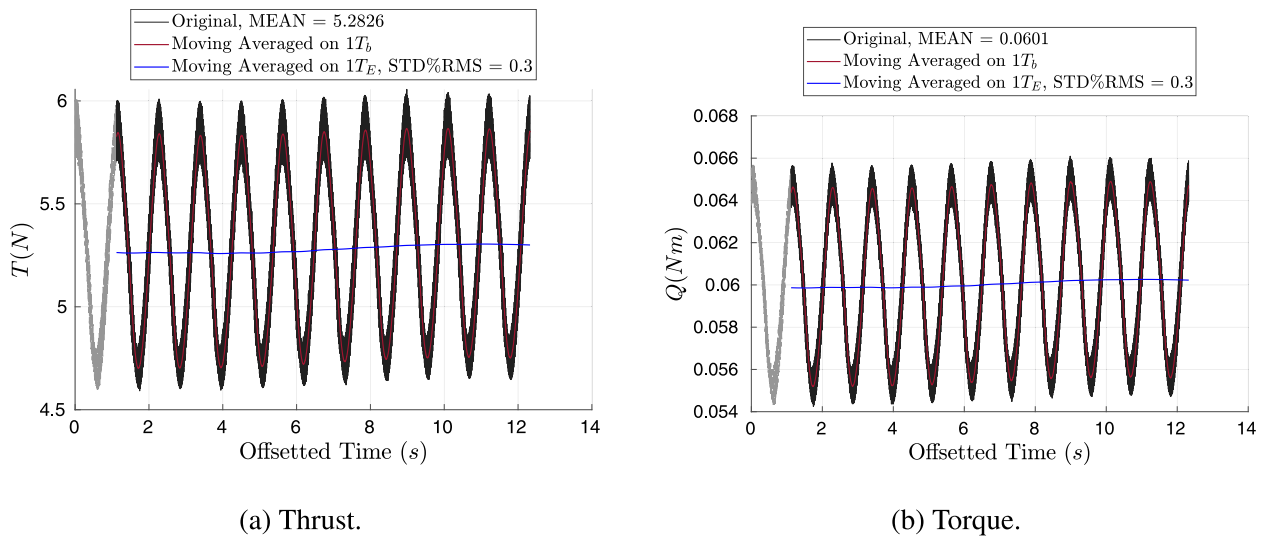

(a) Thrust.   (b) Torque.

Fig. 18. Original and periodic moving average (on $1T_b$ and $1T_E$) of the thrust and torque time series tail in self-propulsion simulation in $\lambda/L = 1.1$ at $n = 16.50$ rps.

The defined convergence criterion in regular head waves is fulfilled in all wave conditions as depicted in Fig. 23. Thereafter, the post-processing of the results is carried out on the chosen time windows in each wave condition.

In Fig. 24, the tail of the self-propulsion simulations (at model SPP) time series of the instantaneous ship velocity, spring force and light-weight carriage force over the chosen time window in calm water and regular head waves are presented. The wave encounter period T_E is different for each wave length and the time window in each condition is chosen based on the explanations in Section 4.5. The mean values over the chosen time window are given in the legends of the plots.

The instantaneous ship velocity and spring force in regular head waves mainly oscillate in the wave encounter frequency as well as the spring natural frequency. The oscillations in the wave encounter frequency are more significant in $\lambda/L = 1.6$. The mean values of the instantaneous ship velocity over the chosen time window, seen in Fig. 24(a), remain very close to the expected ship velocity U. Although rather significant oscillations in the wave encounter frequency are seen for the light-weight carriage force in Fig. 24(c), the mean values in all conditions are negligible.

The mean values of the spring force are rather significant, particularly in $\lambda/L \approx 1.1$. A more accurate estimation of the propeller rotational speed n in each condition is required to reach the self-propulsion point of the model with precisely zero mean spring force. Moreover, the simulations should run for a longer physical time to gain a more accurate insight into the behavior of the spring system based on the estimated propeller rotational speed. However, these demand an extensive amount of computational power which falls beyond the scope of the current investigations. Therefore, the current status of the simulations is deemed adequately acceptable for an overall ship performance analysis, and the mean values of the spring and light-weight carriage forces are considered as the inconsequential correction of the thrust deficit/excess at the estimated propeller rotational speed to reach the model SPP.

6.2.1. Propulsive factors

The averaged propulsive factors in regular head waves, obtained according to the procedure provided in Section 4.5, are presented in Table 7. The bare hull (BH) total resistance results, adopted from Irannezhad et al. (2023), are combined with the mean values of the propeller thrust, spring force and light-weight carriage force over the chosen time window in each wave condition to derive the thrust deduction factor based on Eq. (4). Interestingly, the thrust deduction factor in all three regular head waves is decreased in comparison to the calm water value $\bar{t} = 0.1960$ presented in Table 4. This, as one of the main objectives of the current paper, will be further analyzed in the following sections.

In regular head waves, only the fully turbulent open water curves, shown in Fig. 5, are considered within the applied thrust identity method to derive the Taylor wake fraction and other propulsive factors. Moreover, the results of the applied thrust identity method in calm water based on solely the fully turbulent open water curves, calculated in Table 4, are retrieved for comparison.

Table 7

Propulsive factors and corresponding quantities derived from CFD simulations in calm water and regular head waves, in which the propeller rotational speed n in each condition represents the estimated model SPP in Table 2.

Calm	BH	SP ($n = 16.50$ rps)						
	$\bar{R}_T$ (N)	$-K\bar{x}$ (N)	$-m_3\bar{\ddot{x}}$ (N)	$\bar{T}$ (N)	$\bar{Q}$ (Nm)	$\bar{P}_D$ (W)	$10\bar{K}_Q$ (–)	$\bar{K}_T$ (–)
	4.4189	0.1250	−0.0001	5.3713	0.0609	6.3096	0.2403	0.2091
	BH & SP	Thrust Identity Method (Fully Turbulent Open Water Curves)						
	$\bar{t}$ (–)	$\bar{J}_T$ (–)	$\bar{w}_T$ (m)	$10\bar{K}_{Q_o}$ (–)	$\bar{\eta}_O$ (–)	$\bar{\eta}_H$ (–)	$\bar{\eta}_R$ (–)	$\bar{\eta}_D$ (–)
	0.1960	0.2908	0.4068	0.2339	0.4125	1.3552	0.9734	0.5442
$\lambda/L = 0.6$	BH	SP ($n = 20.00$ rps)						
	$\bar{R}_T$ (N)	$-K\bar{x}$ (N)	$-m_3\bar{\ddot{x}}$ (N)	$\bar{T}$ (N)	$\bar{Q}$ (Nm)	$\bar{P}_D$ (W)	$10\bar{K}_Q$ (–)	$\bar{K}_T$ (–)
	6.9165	−0.0267	0.0010	8.3662	0.0938	11.7830	0.2520	0.2217
	BH & SP	Thrust Identity Method (Fully Turbulent Open Water Curves)						
	$\bar{t}$ (–)	$\bar{J}_T$ (–)	$\bar{w}_T$ (m)	$10\bar{K}_{Q_o}$ (–)	$\bar{\eta}_O$ (–)	$\bar{\eta}_H$ (–)	$\bar{\eta}_R$ (–)	$\bar{\eta}_D$ (–)
	0.1707	0.2608	0.3551	0.2411	0.3815	1.2859	0.9565	0.4693
$\lambda/L = 1.1$	BH	SP ($n = 24.54$ rps)						
	$\bar{R}_T$ (N)	$-K\bar{x}$ (N)	$-m_3\bar{\ddot{x}}$ (N)	$\bar{T}$ (N)	$\bar{Q}$ (Nm)	$\bar{P}_D$ (W)	$10\bar{K}_Q$ (–)	$\bar{K}_T$ (–)
	11.1856	−0.6164	0.0003	13.6968	0.1505	23.2051	0.2687	0.2411
	BH & SP	Thrust Identity Method (Fully Turbulent Open Water Curves)						
	$\bar{t}$ (–)	$\bar{J}_T$ (–)	$\bar{w}_T$ (m)	$10\bar{K}_{Q_o}$ (–)	$\bar{\eta}_O$ (–)	$\bar{\eta}_H$ (–)	$\bar{\eta}_R$ (–)	$\bar{\eta}_D$ (–)
	0.1449	0.2118	0.3574	0.2531	0.3222	1.3307	0.9420	0.4039
$\lambda/L = 1.6$	BH	SP ($n = 19.44$ rps)						
	$\bar{R}_T$ (N)	$-K\bar{x}$ (N)	$-m_3\bar{\ddot{x}}$ (N)	$\bar{T}$ (N)	$\bar{Q}$ (Nm)	$\bar{P}_D$ (W)	$10\bar{K}_Q$ (–)	$\bar{K}_T$ (–)
	6.3715	−0.1267	0.0003	7.8107	0.0877	10.7154	0.2496	0.2191
	BH & SP	Thrust Identity Method (Fully Turbulent Open Water Curves)						
	$\bar{t}$ (–)	$\bar{J}_T$ (–)	$\bar{w}_T$ (m)	$10\bar{K}_{Q_o}$ (–)	$\bar{\eta}_O$ (–)	$\bar{\eta}_H$ (–)	$\bar{\eta}_R$ (–)	$\bar{\eta}_D$ (–)
	0.1708	0.2668	0.3587	0.2396	0.3880	1.2930	0.9602	0.4817

The operational condition under study represents the model SPP, hence the propeller is highly loaded leading to rather low advance ratios $\bar{J}_T$ (extracted from the propeller open water curves) in calm water and all three regular head waves.

Even though the propeller rotational speed is substantially different in different waves, the Taylor wake fraction is almost equal in all three wave lengths, and at the same time smaller than the calm water value. As presented in Irannezhad et al. (2023), the nominal wake in waves changes depending on the wave conditions. The mean values of the surface-averaged axial component of the nominal wake over the propeller disk (BH condition) are 9.8%, 21.3% and 14.6% larger than the calm water value in $\lambda/L = 0.6$, 1.1 and 1.6, respectively. The propeller loading is dependent on the wake. The loading decreases when the wake becomes fuller and vice versa, at a constant rotational speed. The propeller suction effect becomes stronger with increased loading. The combination of varying nominal wake and propeller loading in waves leads to opposing effects which might be the reason for the similar Taylor wakes in different wave conditions. Notably, the Taylor wake fraction decreases in all three waves compared to the calm water value (fuller wake), or in other word, the propeller advance velocity increases in waves in comparison to calm water.

The delivered power in $\lambda/L = 1.1$ exceeds substantially that of the other studied waves. This is primarily attributable to the significantly larger total resistance in this wave, coupled with a noticeably lower total propulsive efficiency. Interestingly, the open water efficiency, hull efficiency, relative rotative efficiency and propulsive efficiency in all three studied regular waves are reduced in comparison to calm water. The reduction of the open water efficiency $\bar{\eta}_O$, relative rotative efficiency $\bar{\eta}_R$ and propulsive efficiency $\bar{\eta}_D$ is more pronounced in $\lambda/L = 1.1$ than the shorter and longer waves. However, the hull efficiency $\bar{\eta}_H$ is reduced more significantly in $\lambda/L = 0.6$ and $\lambda/L = 1.6$ where there is a smaller discrepancy between the thrust deduction factor $\bar{t}$ in regular head waves and calm water. The detailed analysis of the discrepancies of each propulsive factor in regular head waves from the calm water values is out of the scope of the current investigations. Nevertheless, the potential causes that have resulted in the variation of the thrust deduction factor are addressed in the following.

6.2.2. Impacts of waves on thrust deduction factor

In this section, the impacts of regular head waves on the thrust deduction factor are analyzed, employing the bare hull (BH) findings adopted from Irannezhad et al. (2023) and the current self-propulsion (SP) results at the model SPP in calm water and regular head waves CFD simulations. To this end, the behavior of the ship and its propeller during one encounter wave period T_E in each wave length are analyzed using the time series of different quantities. Consequently, the oscillations in the spring natural frequency are mainly disregarded in such time series.

For the BH results, the reconstructed time series is provided considering the dominant harmonic components, details of which can be found in Irannezhad et al. (2023). However, for the SP in regular head waves, due to the exceedingly complex behavior of the time series, the results of the Fourier analysis may become very hard to interpret. Therefore, the reconstruction of time series based on the blade passing and wave encounter frequencies becomes unfeasible. Although other signal processing techniques, such as Hilbert-Huang Transform by Huang and Attoh-Okine (2005), can be applied to gain more insight into the time series behavior, it is out of the scope of the current paper's objectives. Therefore, for an accurate demonstration of the SP time series, a time window (equal to $1T_E$ in each wave length) is extracted from the original time series, which is referred as "$1T_E$ window" henceforth.

For a consistent representation of the BH and SP time series, an identical time origin $t/T_E = 0$ should be considered. Given that the origin of the BH reconstructed time series is defined as the time in which the wave crest is located at the initial position of the ship fore perpendicular (FP), the $1T_E$ window from the original SP time series should be extracted accordingly. Therefore, the $1T_E$ window is extracted from approximately the last two encountered waves in each SP simulation, in which the origin of time $t/T_E = 0$ (kick-off time for the $1T_E$ window) is the time when the wave crest reaches the initial position of the ship fore perpendicular and considering the end point of $1T_E$ after the kick-off time in each wave length.
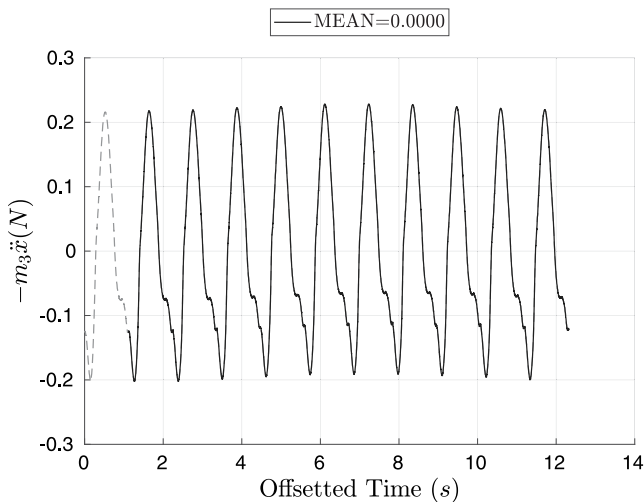
The aforementioned time series from the BH and SP investigations are shown in Figs. 25, 26, 28, 29 and 31. One important point about
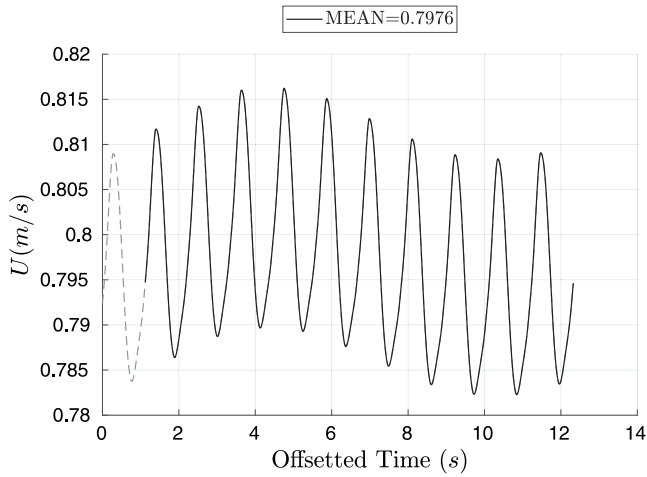
(a) Instantaneous velocity.
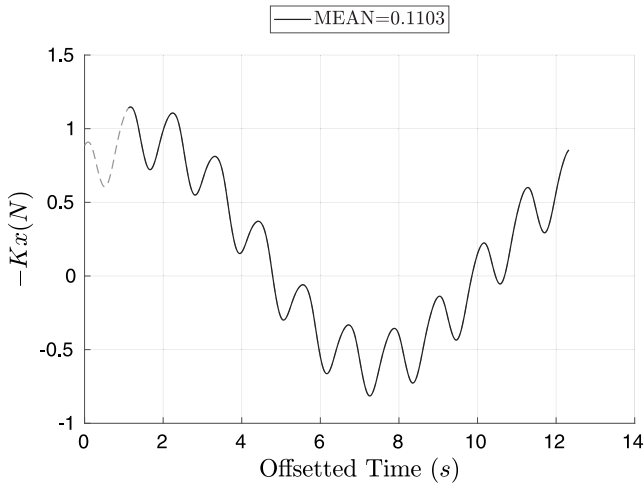
(b) Spring force.

(c) Light-weight carriage force.

Fig. 19. Tail of time series of instantaneous velocity, spring force and light-weight carriage force in self-propulsion simulation in $\lambda/L = 1.1$ at $n = 16.50$ rps.

these time series is that the time in the horizontal axis is divided by the wave encounter period T_E. Given that T_E varies for each wave length, the time series in each wave length are stretched/compressed distinctively. Nonetheless, presenting the results in this way enhances the analysis and comparison of each studied quantity between different wave lengths. Moreover, consistent line colors for the results from each wave length and consistent line types for the results of BH and SP conditions are considered in the presented plots.

In Fig. 25(a), the analytical free surface elevation ζ at the initial position of the ship fore perpendicular (FP) and propeller center (PC) for each wave length are shown. Given that the monitored wave elevation at the probe in both BH and SP simulations is very similar to the analytical counterpart, these time series are not presented.

The significant difference between the presented mean surge motion time series in BH and SP conditions in Fig. 25(b) arises from the effects of the spring system. For BH, the presented reconstructed time series include the spring effects during one spring natural period, whereas for SP, solely a $1T_E$ window of the original time series is extracted which might represent any arbitrary time period of the spring response in its natural period. Therefore, these time series should not be compared between BH and SP in terms of the mean values. However, the dominant harmonic components, i.e., 1st harmonic amplitude and phase, are comparable and similar between BH and SP in each wave length. The minimum surge in all three waves in both BH and SP conditions occurs approximately near $t/T_E \approx 0.5$, i.e., when the wave trough is close to the ship fore perpendicular.

The heave and pitch motions in each wave length are almost identical between BH and SP conditions. A complete analysis of the BH motions in different wave lengths is provided in Irannezhad et al. (2023), which are also applicable for the SP condition in the current paper. One of the important points is the relatively more significant heave and pitch motions in $\lambda/L = 1.1$ and 1.6 in comparison to the shortest wave $\lambda/L = 0.6$, which were found to substantially affect the ship nominal wake in the longer waves in BH condition. Since the motions in BH and SP are almost identical, then the resistance and nominal wake analyses from the BH studies can facilitate the analysis of the propeller performance and its interactions with the hull in the SP condition. Therefore, the reconstructed time series of the total resistance and axial velocity component of the surface-averaged (over propeller disk) nominal wake $\tilde{u}$ from the BH studies in calm water (single value) and regular head waves are provided in Fig. 26.

As discussed thoroughly in Irannezhad et al. (2023), during one encountered wave period in regular head waves, substantial variations are seen for $\tilde{u}$, as shown in Fig. 26(b), and the time-averaged values in all three waves are larger (around 9.8%, 21.3% and 14.6% for $\lambda/L = 0.6$, 1.1 and 1.6, respectively) than the calm water value. Overall, the variation of nominal wake in waves is found to be associated with the instantaneous propeller disk velocities, boundary layer contraction/expansion due to hull motions, bilge vortex dynamics, shaft vortex dynamics and the orbital wave velocities at the propeller disk as well as the complex interactions between these factors in different operational conditions.

In $\lambda/L = 0.6$, due to small heave and pitch motions, the contribution from the instantaneous disk velocities, the boundary layer development due to motions as well as the shaft and bilge vortices dynamics are found to be rather insignificant and the wake is found to be mainly affected by the wave orbital velocities. This can be perceived through the observation of the similar behavior of $\tilde{u}$ in Fig. 26(b) and the analytical wave at the propeller center ζ_{PC} in Fig. 25(a). Nonetheless, the wave orbital velocities slightly affect the boundary layer thickness and the strength of the vortical structures within the propeller disk. These effects lead to approximately 9.8% larger time-averaged axial wake $\bar{\tilde{u}}$ in this wave length in comparison to calm water value.
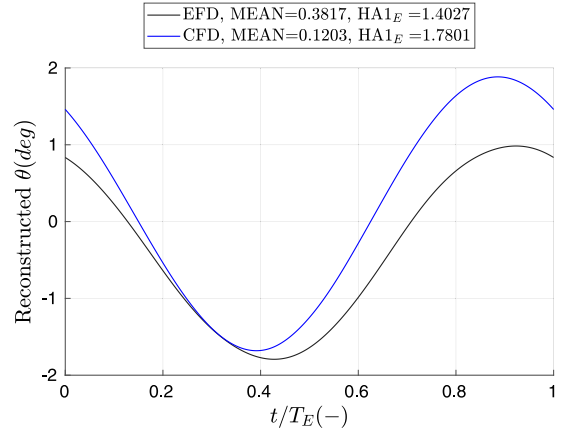
However, large amplitude ship motions in $\lambda/L = 1.1$ and 1.6 significantly affect the formation of the boundary layer as well as the dynamics of the vortical structures. In Fig. 26(b), significant variations
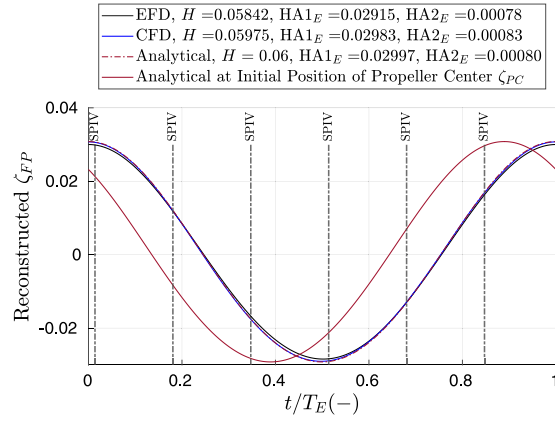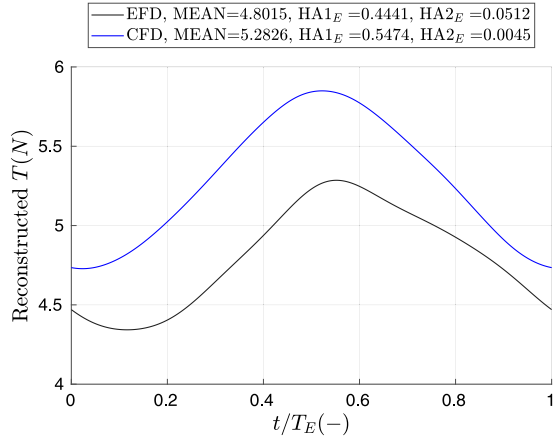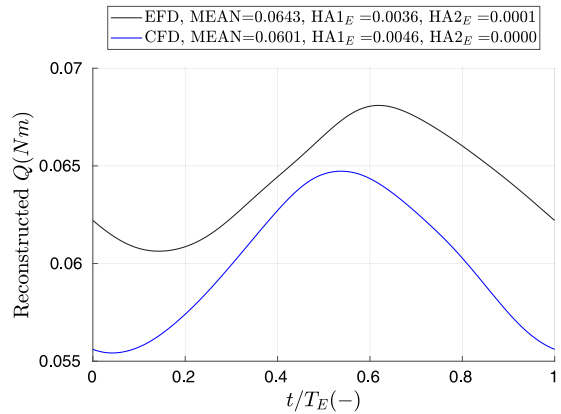
(a) Free surface elevation.
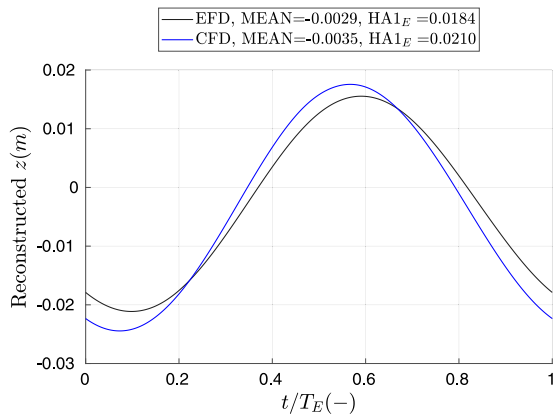
(b) Heave.

(c) Pitch.

(d) Thrust.

(e) Torque.

Fig. 20. Reconstructed time series of free surface elevation, heave, pitch, thrust and torque for EFD and CFD in self-propulsion condition in $\lambda/L = 1.1$ at $n = 16.50$ rps.

are seen for $\bar{u}$ in these wave lengths, in which the presence of the higher harmonic amplitudes may reveal complex interactions between different contributing factors. As mentioned before, $\bar{u}$ in $\lambda/L = 1.1$ and 1.6 is respectively 21.3% and 14.6% larger than the calm water value.

For a better illustrations of the results, the vortical structures found by Q-criterion $= 10$ /s² (similar to Fig. 17(b) for SP, but looking from portside) as well as the distribution of the nominal wake on the propeller disk at the time instances of maximum and minimum $\bar{u}$

from the BH investigations in each wave length are shown in Fig. 27. Moreover, the shaft (propeller center) vertical displacement Δz_{shaft} and acceleration $\ddot{\Delta} z_{shaft}$ time series are shown in Fig. 28 demonstrating the combined effects of heave and pitch motions at the aft ship. Since the BH and SP motions are almost identical, solely the time series of vertical displacement and acceleration in SP condition are depicted.

The nominal wake in $\lambda/L = 0.6$ at the maximum and minimum $\bar{u}$ time instances are rather similar and the bilge vortex and shaft vortex
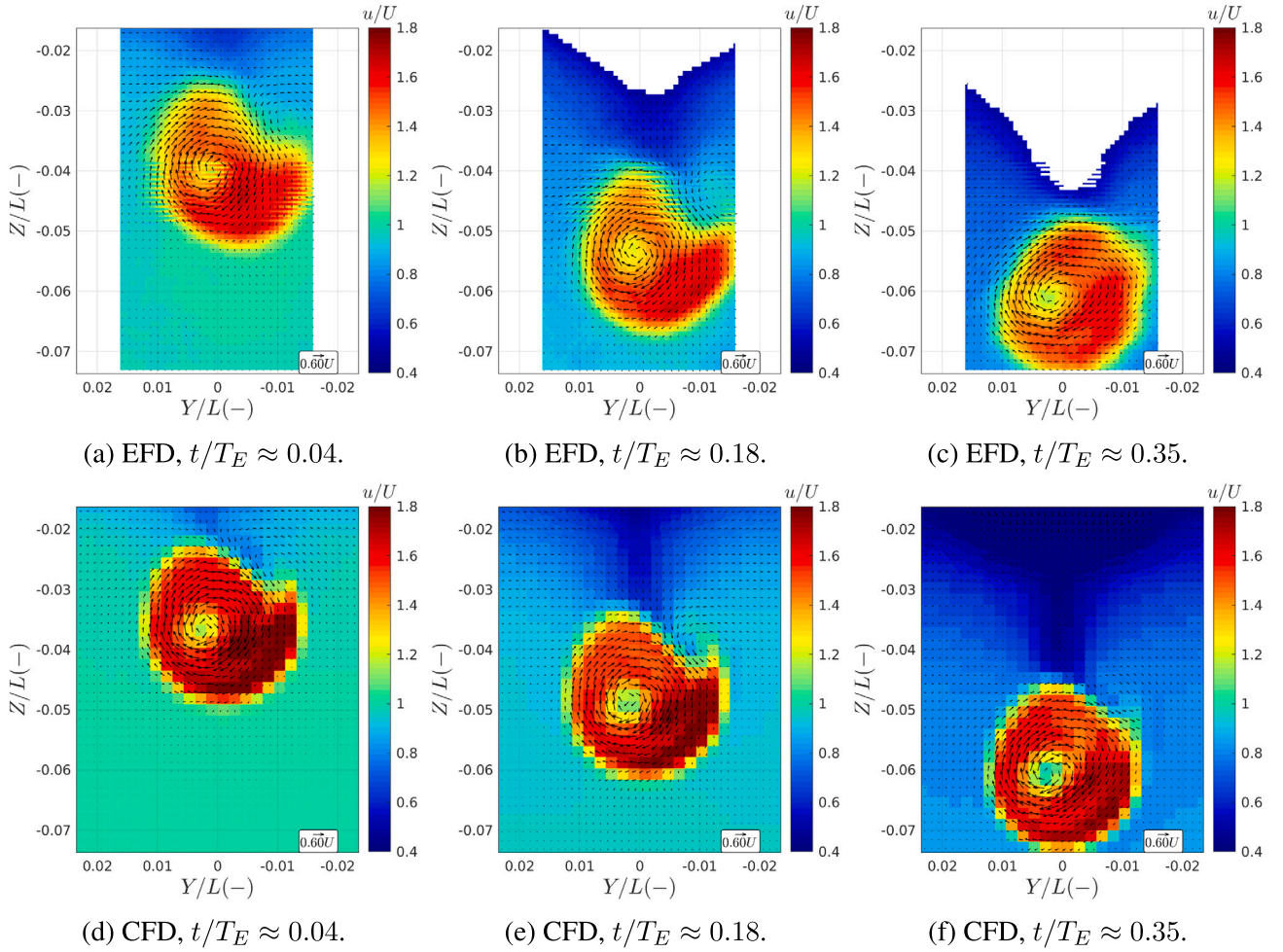
Fig. 21. Comparison of propeller slipstream velocity distribution, on the carriage-fixed propeller slipstream plane in CF_{PSP} coordinate system, between EFD and CFD at different $t/T_E \approx 0.04$, 0.18 and 0.35 time instances in $\lambda/L = 1.1$ in self-propulsion condition at $n = 16.50$ rps.

positions on the disk remained almost unchanged, due to previously discussed small ship motions in this wave. However, the maximum and minimum $\tilde{u}$ time instances of nominal wake are substantially different in both $\lambda/L = 1.1$ and 1.6.

In both $\lambda/L = 1.1$ and 1.6, the maximum of $\tilde{u}$ coincides with the time in which the shaft is almost horizontal ($\Delta z_{shaft} \approx 0$) and moving downwards and ζ_{PC} is approaching the still water level from the wave crest. The considerable downward motion of the shaft center leads to contraction of the boundary layer which consequently results in an upward moving flow around the aft bilge and thus formation of a strong bilge vortex which sweeps away the weakened shaft and bilge vortices at the propeller disk. At this time, the bilge vortex disperses and moves almost out of the propeller disk while the weakened shaft vortex at the propeller disk is located above the shaft and the area below the shaft is mainly a high-velocity area.

On the other hand, the minimum $\tilde{u}$ for $\lambda/L = 1.1$ and 1.6 occurs when the shaft is located lower than its original position and moving upwards and the wave trough just passed (ζ_{PC} is reaching the still water level). At this stage, bilge vortices hit the propeller plane and play a significant role in the dynamics of the wake at the propeller disk, as shown in Figs. 27(e) and 27(f). A strong shaft vortex in the minimum wake state is located under the shaft which leads to the formation of a large patch of low-speed flow in this region.

Overall, the large hull motions in the longer waves ($\lambda/L = 1.1$ and 1.6) dictate the variation of nominal wake through both the contraction/expansion of the boundary layer as well as the imposed

vortical structure dynamics. However, the wave orbital velocities are the dominant factor in the shortest wave $\lambda/L = 0.6$ where the hull motions are insignificant. These features of the bare hull nominal wake are discussed to aid in the analysis of the self-propulsion performance of the ship in the following discussion.

In Fig. 29, the total thrust and torque time series ($1T_E$ window), as well as the single-blade ones, are shown for model SPP simulations in regular head waves. The amplitudes of the oscillations of the total thrust and total torque time series in the blade passing frequency vary during the wave encounter period, particularly in $\lambda/L = 1.6$, whereas less pronounced in the shortest wave. The 1st harmonic amplitudes of total thrust oscillations in the wave encounter frequency in percentage of the mean thrust value HA1$_E$%MEAN are roughly 3.3%, 5.0% and 9.4% in $\lambda/L = 0.6$, $\lambda/L = 1.1$ and $\lambda/L = 1.6$, respectively.

As shown in Fig. 26(a), the behavior of R_T is almost similar for all three waves during each respective T_E, with negative total resistance values occurring approximately in $0.25 < t/T_E < 0.75$, and maximum/minimum resistance values approximately at the time of wave crest/trough at the ship fore perpendicular. According to Table 7, the mean of the total resistance in $\lambda/L = 1.1$ is larger than the other two waves. On the other hand, the departure of the transient total resistance in Fig. 26(a) for $\lambda/L = 1.1$ from its mean value is smaller in comparison to the shorter and longer wave lengths. Intuitively, one might assume that the propeller thrust equals the instantaneous resistance but in the opposite direction, thus enabling the ship to maintain its target speed. However, in reality, the thrust and resistance equilibrium does not occur instantaneously in waves and instead due to different mechanisms
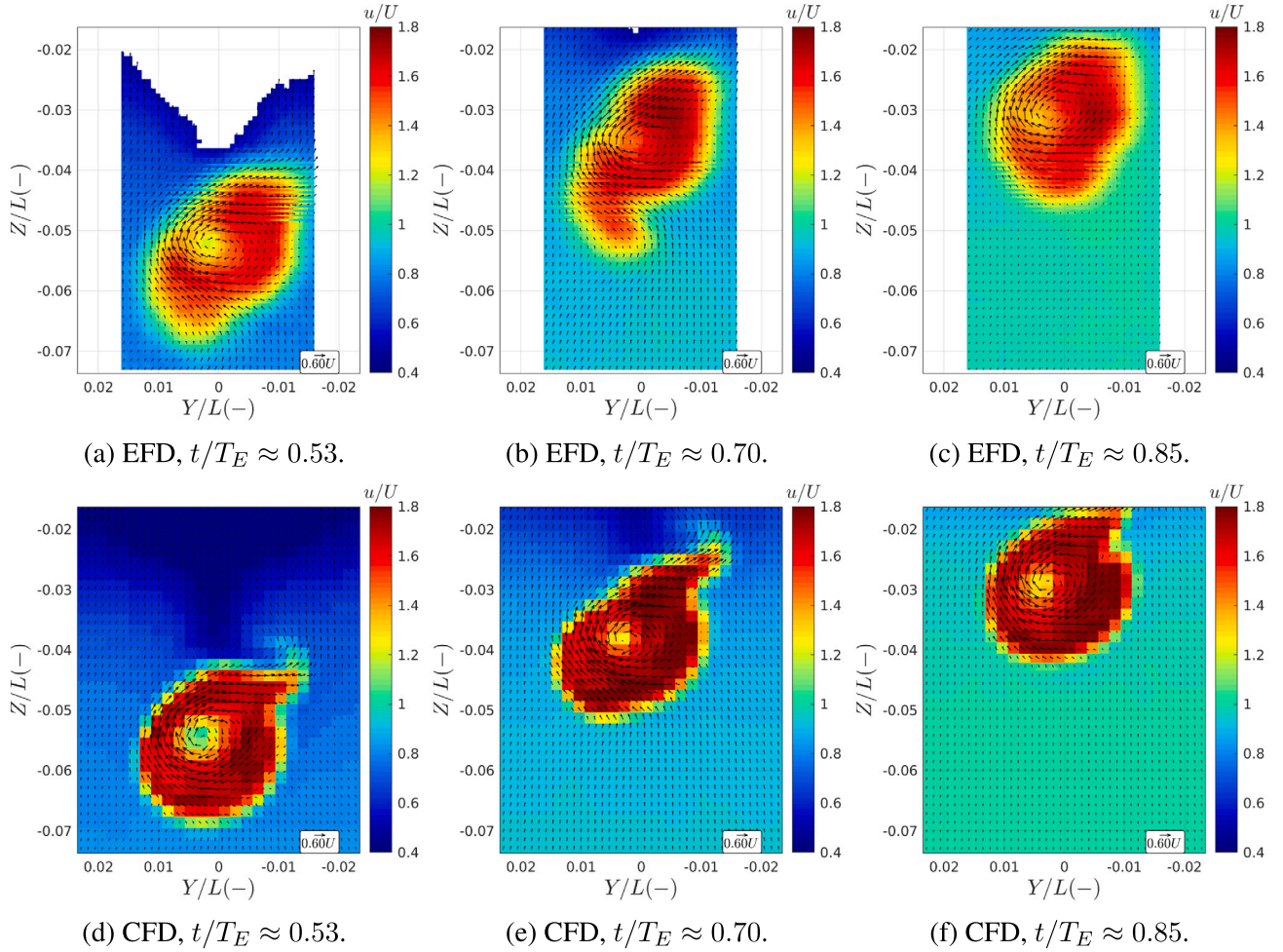
Fig. 22. Comparison of propeller slipstream velocity distribution, on the carriage-fixed propeller slipstream plane in CF_{PSP} coordinate system, between EFD and CFD at $t/T_E \approx 0.53$, 0.70 and 0.85 time instances in $\lambda/L = 1.1$ in self-propulsion condition at $n = 16.50$ rps.

behind resistance and thrust generation they are balanced over a full wave encounter period instead. In the case of the application of a weak spring system for controlling the position of the model relative to the carriage, the equilibrium is achieved over the natural period of the spring (larger spring natural period compared to the wave encounter period). The dynamics of resistance in waves is primarily a result of hull motions which are governed by the hull inertia, while the dynamics of propeller thrust are mainly governed by the flow into the propeller. In waves, the variation of the total resistance around its mean value is roughly one to two orders of magnitude larger than the variation of the wake, and thus the variation of the total thrust.

Generally, in self-propulsion conditions in calm water, higher propeller rotational speed results in higher propeller loading and thrust generation, thus more severe flow suction by the propeller. This results in lower pressure at the aft ship, hence a higher thrust deduction factor for the higher propeller rotational speeds in calm water. In the current investigations, the propeller rotational speed in regular waves is higher than the calm water n to overcome the added resistance due to waves and hence reach the expected ship velocity. Moreover, the unloading skin friction correction force is not applied in this study, and the self-propulsion point of the model is considered, meaning that the propeller is highly-loaded in model-scale to reach the ship's expected velocity with near-to-zero surge motion at model SPP. This means if the calm water conditions presumption were valid, due to the very high propeller rotational speed, the thrust deduction factor should have increased in waves in comparison to calm water. However, based on the results in

Table 7, the thrust deduction factor in all three waves is reduced in comparison to calm water. In the following parts, overall observations (based on the flow physics analysis in BH and SP conditions) are discussed to investigate the reduction of the thrust deduction factor in waves versus calm water in the current study. Thus, most of the discussions are made for the propeller thrust, while the propeller torque is also provided as a reference, despite the fact that the behavior of thrust and torque are very similar.

In all three waves, the oscillations of the total thrust in wave encounter frequency are approximately following the axial component of the nominal wake in Fig. 26(b), as the higher $\tilde{u}$ time instances roughly coincide with the lower thrust time instances in 29(a). However, it is important to notice that the maximum/minimum thrust is occurring slightly later/earlier (in t/T_E) than the minimum/maximum $\tilde{u}$, which might be originated from the propeller induced velocities and the acceleration of the flow upstream of the propeller which leads to a different wake into the propeller in comparison to the nominal wake. Furthermore, greater oscillations of the total thrust time series in the wave encounter frequency are seen for the longer waves with more significant $\tilde{u}$ oscillations.

In Fig. 30, the vortical structures (colored by normalized helicity) are visualized by the iso-surface of Q-criterion = 10 /s^2 from the self-propulsion simulations (model SPP) in regular head waves at the approximate time instances of maximum and minimum BH nominal wake. It should be noted that the presented time instances are chosen to be similar to the BH simulations in Fig. 27, but they do not represent the maximum and minimum thrust conditions.
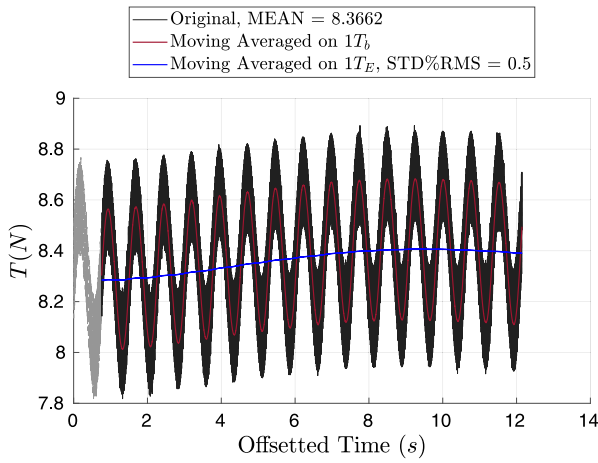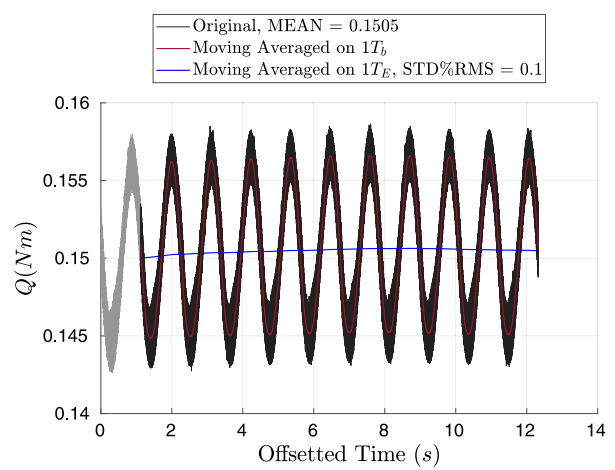
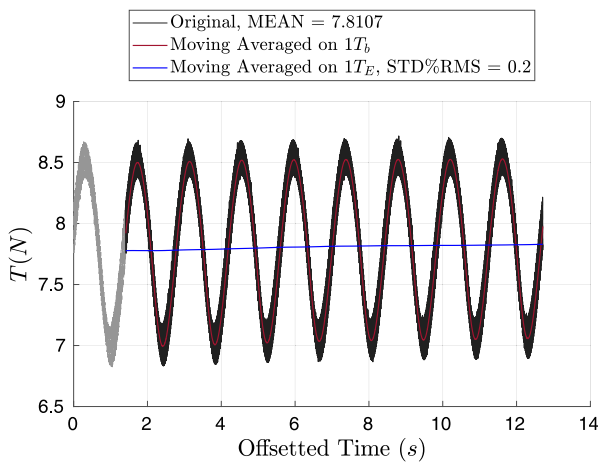(a) Thrust in $\lambda/L = 0.6$.
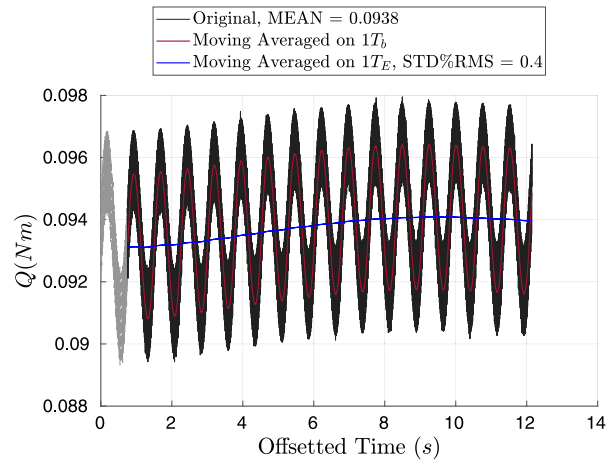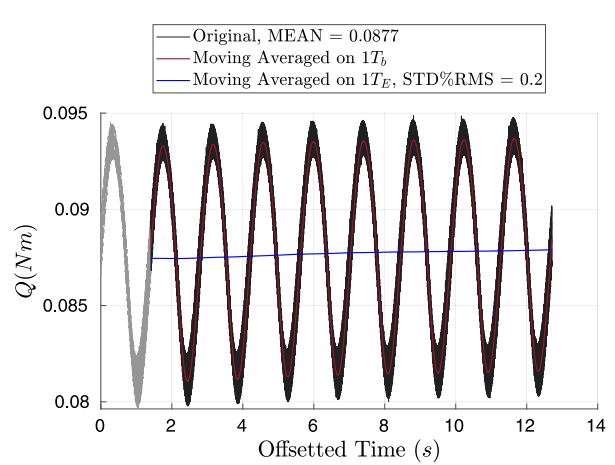
(b) Torque in $\lambda/L = 0.6$.
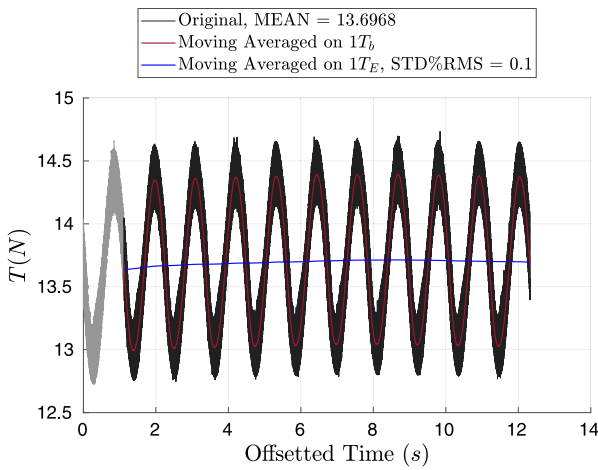
(c) Thrust in $\lambda/L = 1.1$.

(d) Torque in $\lambda/L = 1.1$.

(e) Thrust in $\lambda/L = 1.6$.

(f) Torque in $\lambda/L = 1.6$.

Fig. 23. Original and periodic moving average (on $1T_b$ and $1T_E$) of the thrust and torque time series tail in self-propulsion simulations in $\lambda/L = 0.6$, 1.1 and 1.6 with the corresponding n at model SPP.
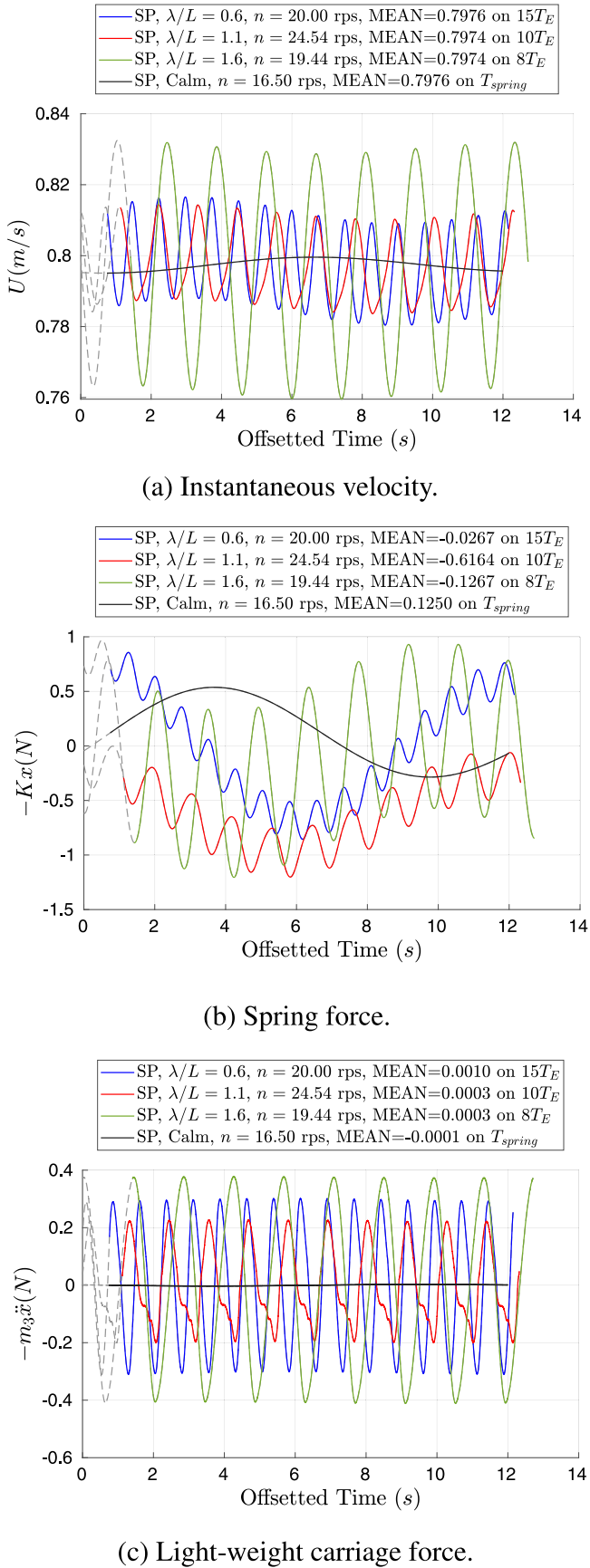
(a) Instantaneous velocity.

(b) Spring force.

(c) Light-weight carriage force.

Fig. 24. Self-propulsion (model SPP) time series of instantaneous velocity, spring force and light-weight carriage force in calm water and regular head waves. The mean values over the chosen time window are provided in the legends.

As discussed before, for the nominal wake analysis, the large hull motions in the longer waves ($\lambda/L = 1.1$ and 1.6) result in contraction/expansion of the boundary layer and extensive vortical structure dynamics which leads to bilge vortices residing outside of the propeller disk within a certain duration of the wave encounter period, which together lead to increase of $\bar{\bar{u}}$ by 21.3% and 14.6% (for $\lambda/L = 1.1$ and 1.6, respectively) in comparison to the calm water value. Although the propeller suction in SP condition may affect the significance of the boundary layer contraction/expansion as well as the time span and the extent of the bilge vortices outside of the disk in comparison to calm water, the effect is presumably less dominant. This implies the flow that is being ingested into the propeller during one encounter period is not consistently from the hull boundary layer, as in calm water. Since at certain time instances of the wave encounter period the flow is being ingested into the propeller from regions outside the hull boundary layer, the aft flow and thus the pressure distribution in the aft are less affected by the propeller action. This difference in flow acceleration and hence the change of pressure in the aft ship in SP in comparison to BH, in conjunction with the observed increase of $\bar{\bar{u}}$ in $\lambda/L = 1.1$ and 1.6 are the most likely physical evident that have led to the decrease of thrust deduction factor in these waves.

One very interesting point here is that the vertical shaft displacement as a combined effect of heave and pitch is very similar in terms of the dominant 1st harmonic amplitude in both $\lambda/L = 1.1$ and 1.6 in Fig. 28(a), even slightly larger for the longer wave, whereas there is a larger reduction of $\bar{t}$ in $\lambda/L = 1.1$ than $\lambda/L = 1.6$ in comparison to calm water. However, it should be reminded that the wave encounter period T_E in $\lambda/L = 1.1$ is smaller than $\lambda/L = 1.6$, hence the shaft vertical acceleration $\ddot{\Delta z}_{shaft}$ is relatively larger in $\lambda/L = 1.1$ as shown in Fig. 28(b). The shaft vertical acceleration represents the hull dynamics in the aft and thus plays a role in the development of the boundary layer in the aft as well as the dynamics of the bilge vortex. Larger shaft acceleration means that the boundary layer and bilge vortex have more vigorous dynamics and thus reside outside the propeller disk for an extended duration. This resulted in a larger (21.3%) increase of $\bar{\bar{u}}$ in $\lambda/L = 1.1$ versus calm water in the bare hull investigations, and is conceptualized to be the main reason for the more significant reduction of the thrust deduction factor versus calm water.

In $\lambda/L = 0.6$ the heave and pitch motions and hence the shaft vertical displacement are insignificant as seen in Figs. 25 and 28(a). Consequently, in this wave, the aft ship pressure reduction, originating from the flow suction by the propeller, is rather concentrated in a roughly similar hull surface area as of calm water condition. On the one hand, the propeller rotational speed in this wave is increased (to $n = 20.00$ rps from the calm water value $n = 16.50$ rps) to overcome the added resistance and reach the expected ship velocity at model SPP (near-to-zero mean surge), which may result in a more intense pressure reduction in the aft ship. On the other hand, a larger advance velocity is expected in this wave versus calm water (due to the effects of the wave orbital velocities, the nominal wake $\bar{\bar{u}}$ increases by 9.8% in comparison to calm water), which in turn results in increased propeller advance velocity. The interplay between the need for increased thrust and at the same time the increase of the propeller advance velocity, leads to reduced propeller loading (less propeller suction), and thus reduced thrust deduction factor in comparison to calm water.

Once again it should be mentioned that the approach taken in this paper to derive the thrust deduction factor at model SPP, i.e., considering the retained spring force and light-weight carriage force as the thrust deficit/excess as shown in Eq. (4), may not fully represent the flow physics in self-propulsion and thus may affect the calculation of thrust deduction factor. However, the proposed modification of the thrust deduction factor is a reasonably accurate representation of the flow physics. The general definition of thrust deduction complies with the concept of resistance increase due to the action of the propeller in comparison to calm water resistance. It is not possible to measure the resistance in self-propulsion in experiments; however, it can be
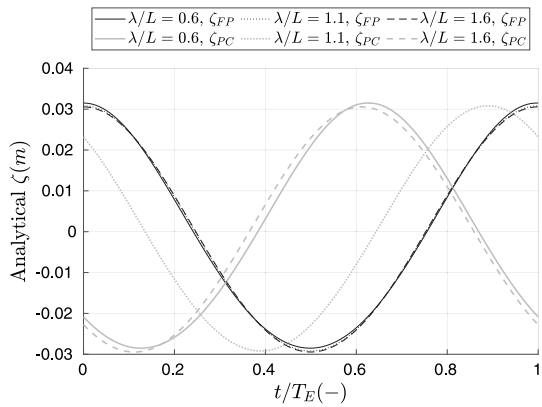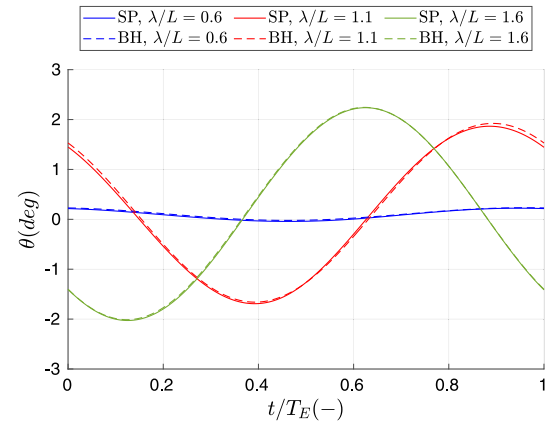
(a) Analytical free surface elevation at FP and PC.
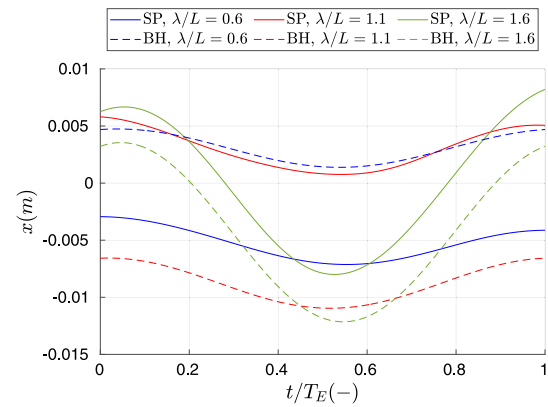
(b) BH (reconstructed) and SP ($1T_E$ window) surge.
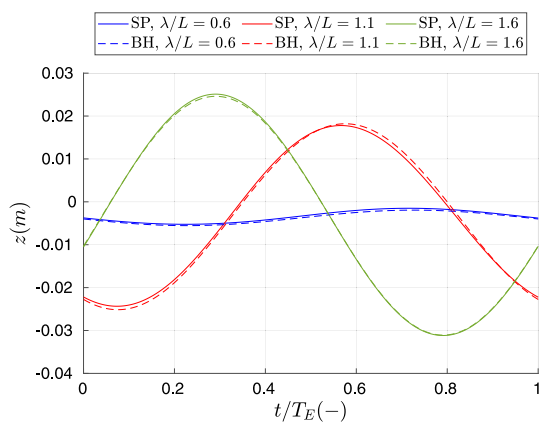
(c) BH (reconstructed) and SP ($1T_E$ window) heave.

(d) BH (reconstructed) and SP ($1T_E$ window) pitch.

Fig. 25. Analytical free surface elevation at the initial positions of the ship fore perpendicular (FP) and propeller center (PC) as well as the reconstructed time series of bare hull (BH) motions (adopted from Irannezhad et al., 2023) in comparison to the $1T_E$ windows of the self-propulsion (SP) motions time series (model SPP) in regular head waves.
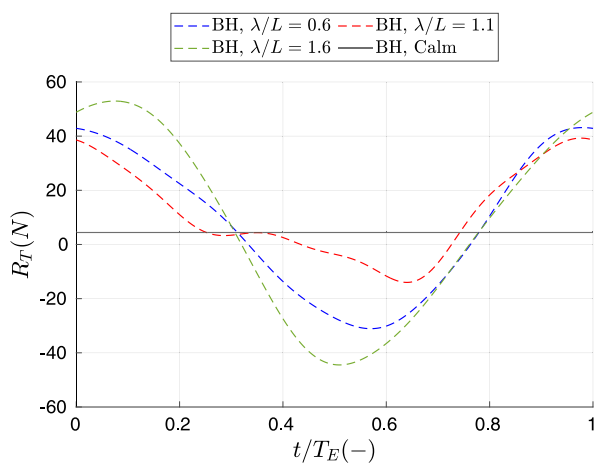
(a) BH (reconstructed) total resistance.
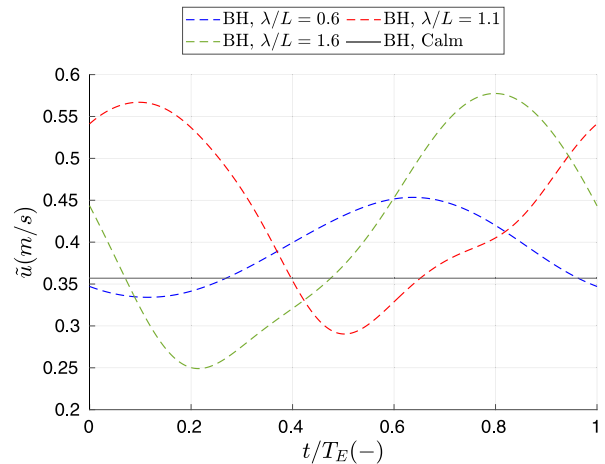
(b) BH (reconstructed) nominal wake (axial).

Fig. 26. Reconstructed time series of bare hull total resistance and surface-averaged (over propeller disk) nominal wake axial velocity component in calm water (single value) and regular head waves, adopted from Irannezhad et al. (2023). The time origin $t/T_E = 0$ is identical to the time origin in Fig. 25.
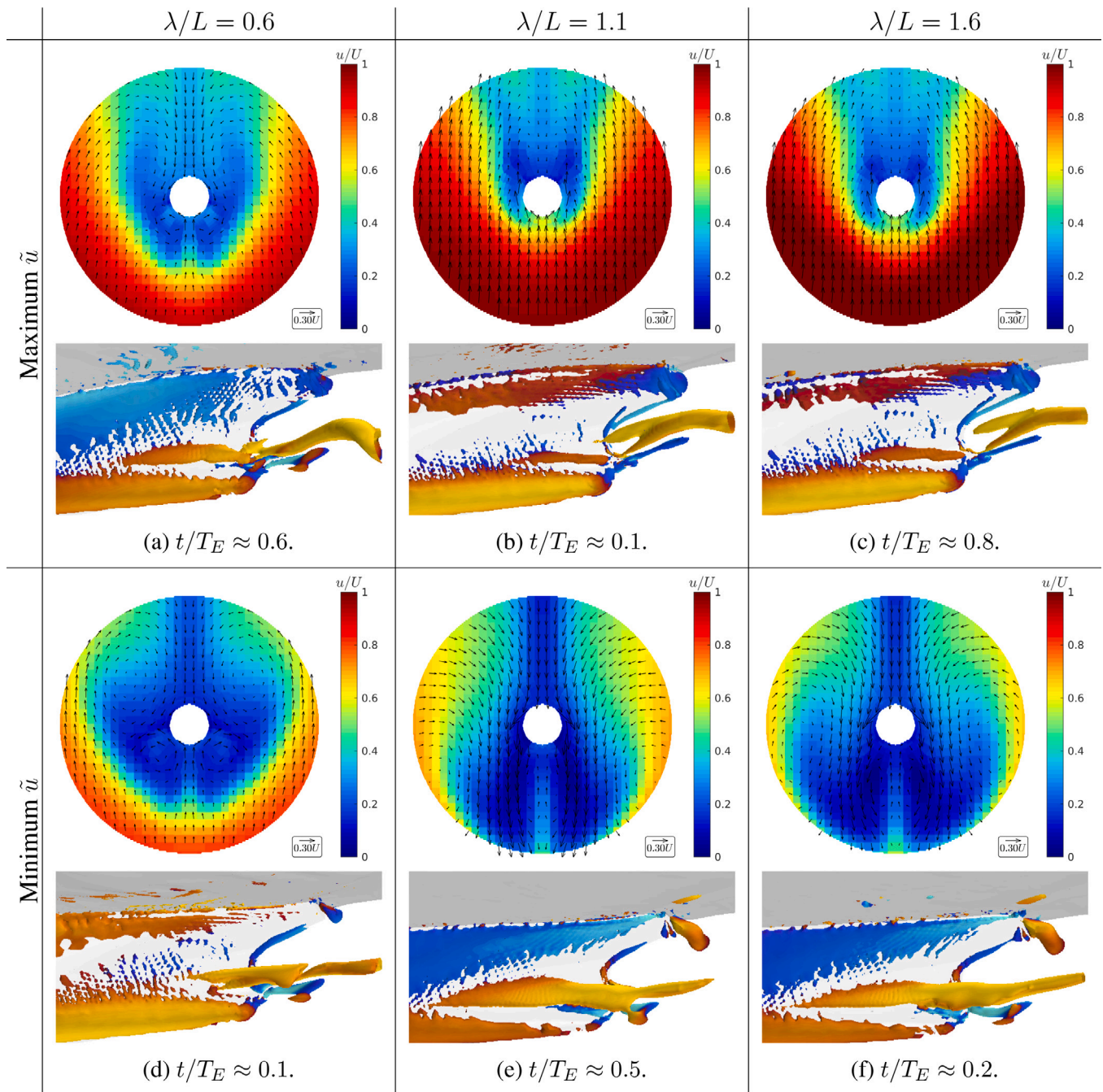
Fig. 27. Bare hull nominal wake on the hull-fixed propeller disk and the vortical structures (colored by normalized helicity provided in Fig. 17) found by Q-criterion = 10 /s² (similar to Fig. 17(b) for SP condition, but looking from portside) at the approximately maximum and minimum time instances of surface-averaged axial velocity component of the BH nominal wake $\tilde{u}$ in regular head wave simulations, adopted from Irannezhad et al. (2023).

estimated through self-propulsion CFD simulations by assuming that the averaged thrust from the propeller is in equilibrium with the averaged resistance forces on the other hull surfaces except the propeller. Consequently, in the current paper, the estimated thrust deduction factors, derived from Eq. (4) and presented in Table 7, are cross-checked through comparison with the estimated resistance increase in self-propulsion simulations from the calm water resistance.

It is worthwhile to also mention that in this paper, the observations made to investigate the impacts of waves on the averaged thrust deduction factor in model-scale are developed around the global effects of waves on the propeller performance and hence propeller-hull interactions, while the physical phenomena entailed in the propeller performance in terms of thrust generation on different blades at various

radial and azimuthal positions and different instances time during ship performance are exceedingly complex. The effects of transversal and vertical velocity components of the hull wake may significantly affect the thrust generation mechanism, for instance by changing the advance angle at various radial and azimuthal positions and hence introducing more abrupt or local effects.

In order to briefly analyze such local effects, the thrust and torque generated from a single blade during one wave encounter period are presented in Figs. 29(c) and 29(d). These plots reveal the complexity of the incident flow field by the propeller, as the thrust generation on this blade significantly changes based on time and azimuthal position, particularly for the longer waves $\lambda/L = 1.1$ and 1.6. One observation is that the oscillations of the total thrust and the single-blade thrust in the
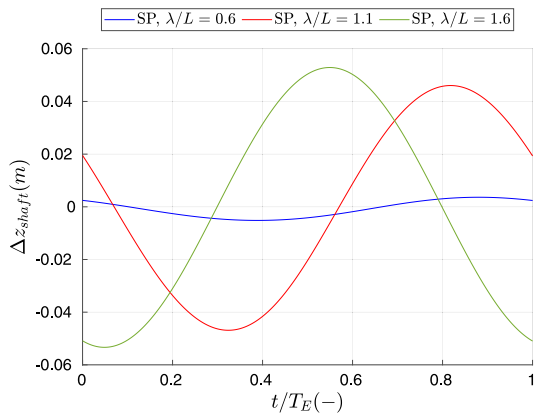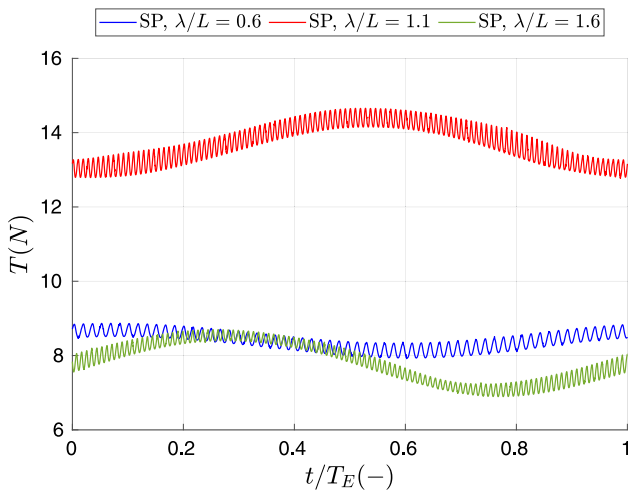
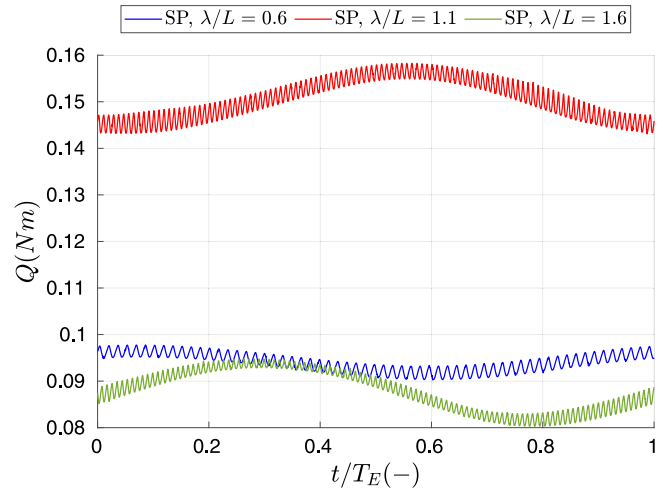(a) SP ($1T_E$ window) shaft vertical displacement.
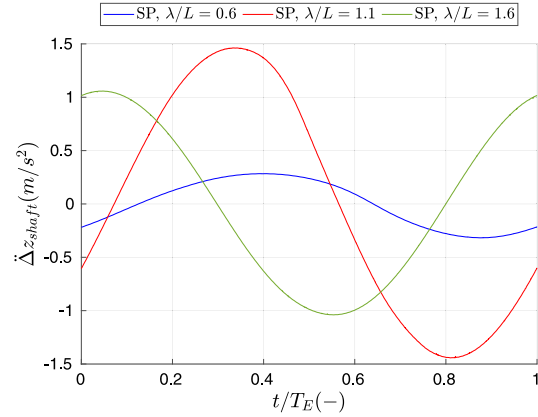
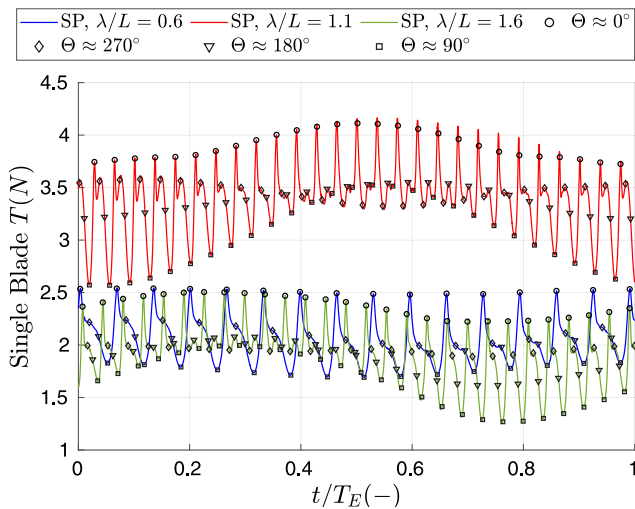(b) SP ($1T_E$ window) shaft vertical acceleration.

Fig. 28. The $1T_E$ windows of the self-propulsion (SP) shaft (propeller center) vertical displacement and acceleration time series in regular head waves. The time origin $t/T_E = 0$ is identical to the time origin in Fig. 25.
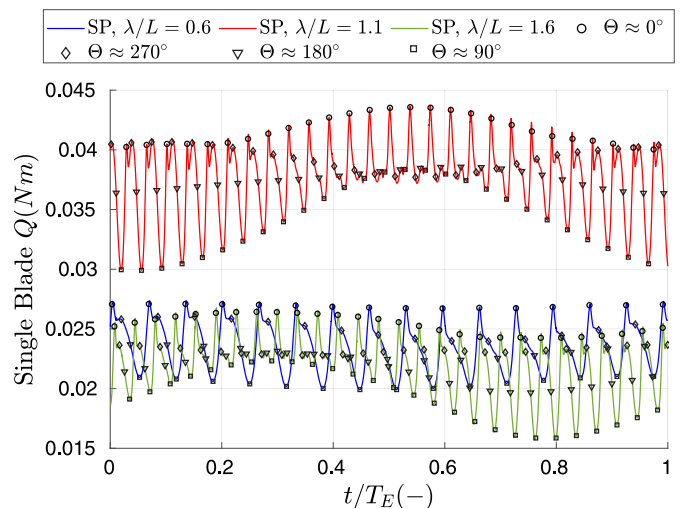

(a) SP thrust ($1T_E$ window).

(b) SP torque ($1T_E$ window).

(c) SP single-blade thrust ($1T_E$ window).

(d) SP single-blade torque ($1T_E$ window).

Fig. 29. Self-propulsion (model SPP) time series of total thrust and torque as well as single-blade thrust and torque over the $1T_E$ window in regular head waves. The time origin $t/T_E = 0$ is identical to the time origin in Fig. 25.
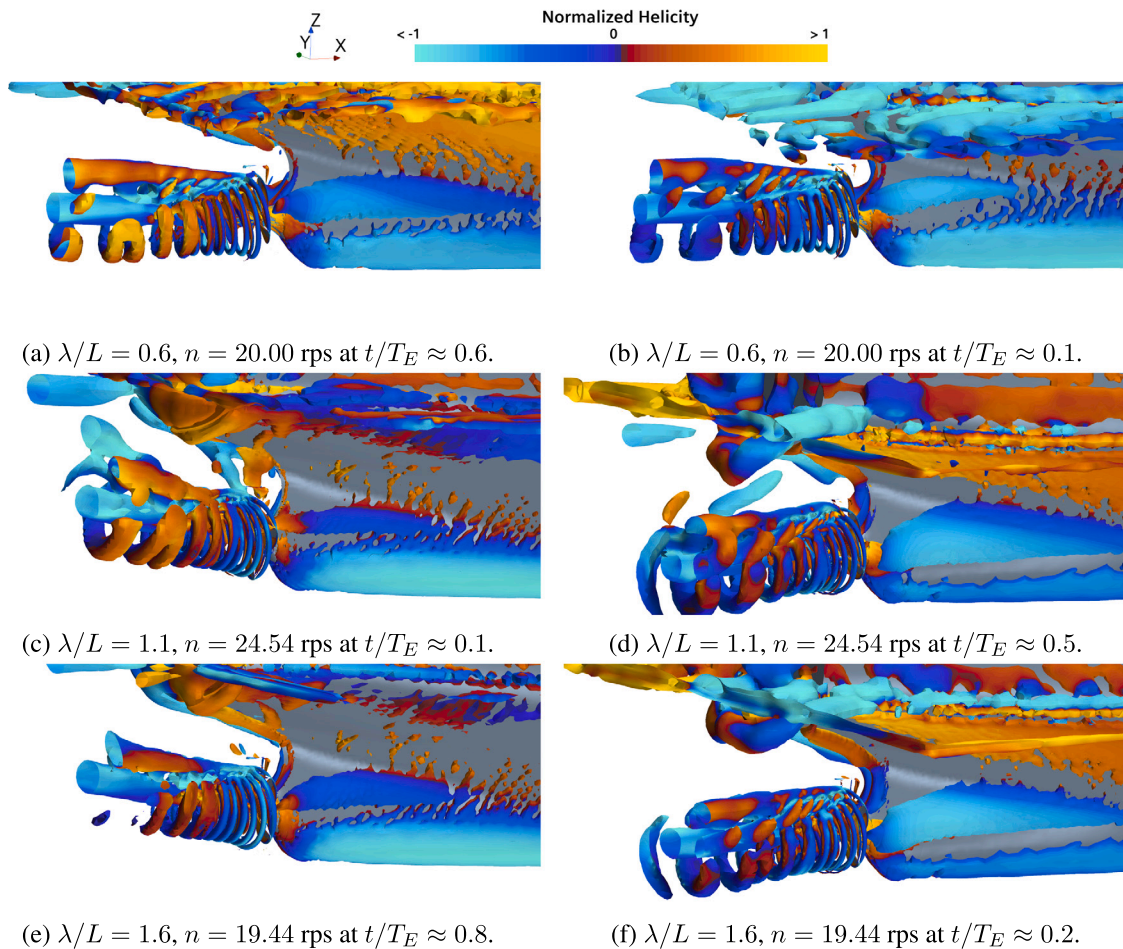
(a) $\lambda/L = 0.6$, $n = 20.00$ rps at $t/T_E \approx 0.6$.

(b) $\lambda/L = 0.6$, $n = 20.00$ rps at $t/T_E \approx 0.1$.

(c) $\lambda/L = 1.1$, $n = 24.54$ rps at $t/T_E \approx 0.1$.

(d) $\lambda/L = 1.1$, $n = 24.54$ rps at $t/T_E \approx 0.5$.

(e) $\lambda/L = 1.6$, $n = 19.44$ rps at $t/T_E \approx 0.8$.

(f) $\lambda/L = 1.6$, $n = 19.44$ rps at $t/T_E \approx 0.2$.

Fig. 30. The vortical structures (colored by normalized helicity) found by Q-criterion = 10 /s^2 from the self-propulsion simulations (model SPP) in regular head waves at the approximate time instances of maximum and minimum BH nominal wake.

wave encounter frequency are almost similar. Although the variation of the generated thrust from the single-blade in each azimuthal position remains rather small in the shortest wave $\lambda/L = 0.6$ (roughly similar to calm water in Fig. 13), the generated thrust at different azimuthal positions varies significantly in longer weaves, especially near $\Theta \approx 270°$ and $\Theta \approx 90°$.

For instance, for calm water in Fig. 13 and the shorter wave $\lambda/L = 0.6$, the minimum thrust of the single-blade occurs around the azimuthal position $\Theta \approx 90°$. Although the minimum thrust of the single-blade mainly occurs around the same azimuthal position $\Theta \approx 90°$ during the major part of the one encounter wave period in the longer waves, for some part of the encounter wave period (e.g., in the vicinity of $t/T_E \approx 0.5$ in $\lambda/L = 1.1$), the azimuthal position which represents the approximate minimum thrust of the single-blade swapped from $\Theta \approx 90°$ to $\Theta \approx 270°$. One of the contributing factors to these effects can be perceived through the transversal and vertical velocity components of the nominal wake from BH, shown in Fig. 31, which can significantly affect the incident flow field of the propeller. Very large variations are seen for the vertical velocity component in $\lambda/L = 1.1$ and 1.6, which were found, in Irannezhad et al. (2023), to be mainly related to the instantaneous propeller disk velocities due to shaft vertical motions. This, apart from the dominant axial velocity component, may partially explain the single-blade thrust generation variation in different azimuthal positions. For example, the time instances with lower bare hull nominal $\bar{w}$ values roughly coincide with the swapping of the minimum single-blade thrust generation azimuthal position from $\Theta \approx 90°$ to $\Theta \approx 270°$.

Further detailed analysis is required to derive more solid conclusions from the single-blade analysis in waves. Nevertheless, to avoid confusion about the significance of oscillations in each wave condition and be able to compare them with the ones seen in calm water, the time series of total thrust and torque as well as the single-blade thrust and torque should be compared during one wave encounter period, but based on the propeller/blade revolution frequencies, as depicted in Fig. 32, instead on t/T_E. The calm water time series is derived from repeating the last propeller revolution from the simulation. The aforementioned discussions are still valid for the total thrust and torque time series. For the single-blade analysis, similar oscillations are generally seen in the shortest wave $\lambda/L = 0.6$ as of calm water, whereas the oscillations vary significantly in the longer waves which might not follow the calm water oscillations during a greater part of the encounter period.

6.3. Computational costs

Fig. 33 displays the computational costs, measured in terms of physical time simulations, across different wave lengths and propeller rotational speeds (n). Approximately $40{,}000$ to $60{,}000$ cells per core are allocated for each simulation during parallel processing. The utilization of different computing resources (HPC clusters) with varying configurations across simulations introduces some inconsistency (bias) when directly comparing computational costs. Nonetheless, the data presented in Fig. 33 can still provide insights into overall comparisons among different simulations.
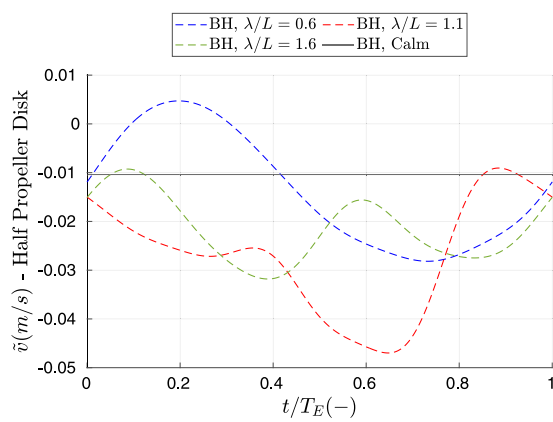
(a) BH (reconstructed) nominal wake (transversal).
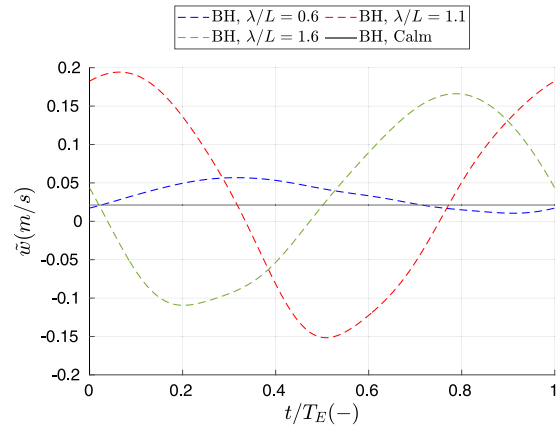


(b) BH (reconstructed) nominal wake (vertical).

Fig. 31. Reconstructed time series of surface-averaged (over propeller disk) nominal wake transversal and vertical velocity components in calm water (single value) and regular head waves ($1T_E$), adopted from Irannezhad et al. (2023). The time origin $t/T_E = 0$ is identical to the time origin in Fig. 25.
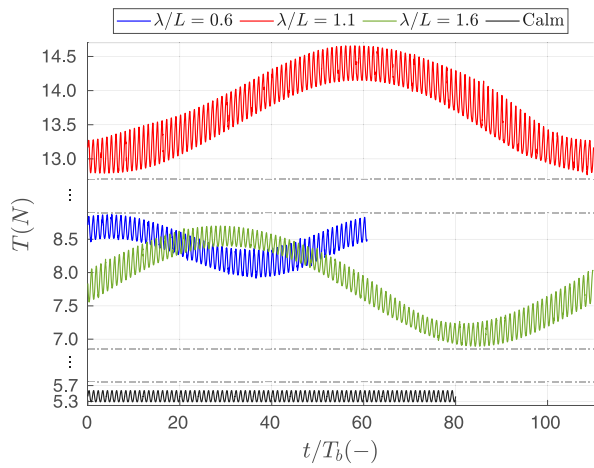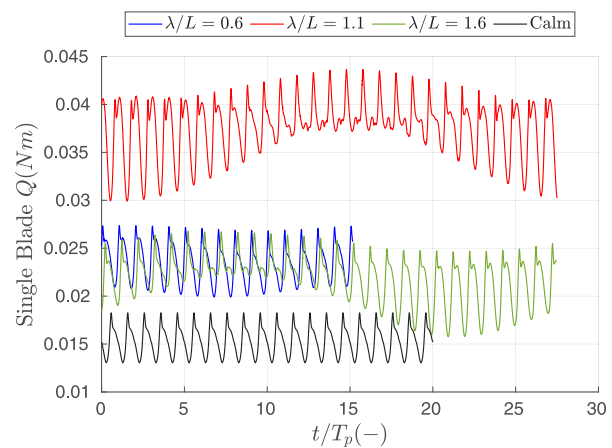

(a) SP thrust ($1T_E$ window).
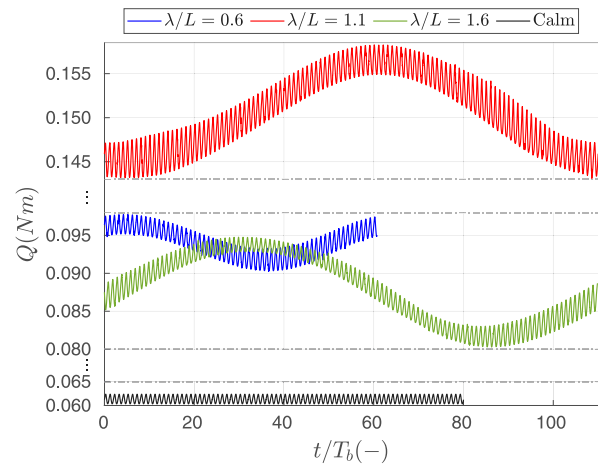
(b) SP torque ($1T_E$ window).
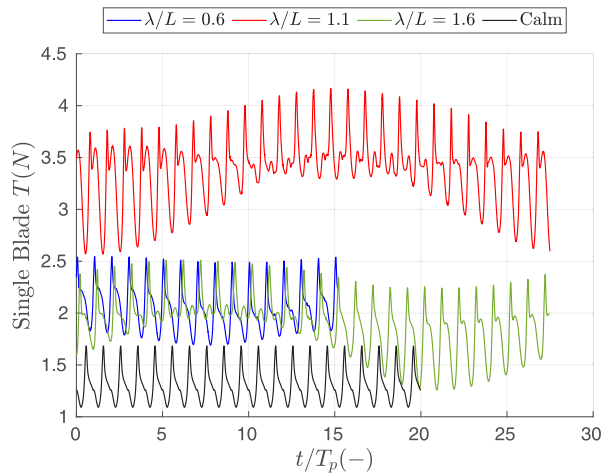
(c) SP single-blade thrust ($1T_E$ window).

(d) SP single-blade torque ($1T_E$ window).

Fig. 32. Self-propulsion (model SPP) time series ($1T_E$ window) of total thrust and torque in t/T_b as well as single-blade thrust and torque in $t/T_p = t/4T_b$ for each propeller rotational speed n in calm water (repeated last revolution) and each regular head waves. The time origin $t/T_b = t/T_b = 0$ is identical to the time origin in Fig. 25 for regular head waves, but selected arbitrarily for calm water.
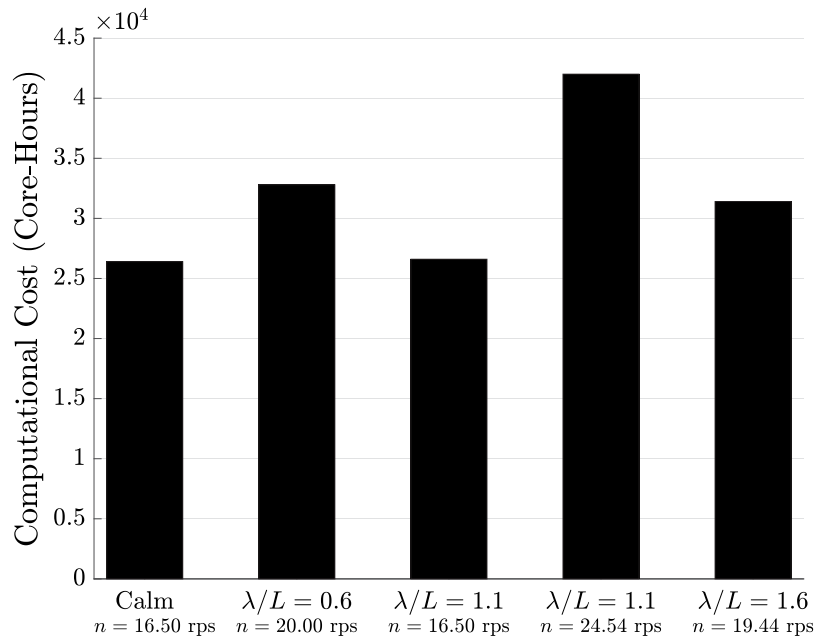
Fig. 33. Computational costs in terms of 1 second of physical time self-propulsion simulation in calm water and regular head waves.

Since the simulations in calm water and regular head waves utilize identical grids and models, the computational expense per second of physical time simulation primarily relies on the time step, which is influenced by n. It should be emphasized that the total computational power required for running simulations under varying operational conditions cannot be directly deduced from the computational costs illustrated in Fig. 33. As mentioned earlier, the simulations were initialized by the MRF approach to mitigate computational expenses, followed by the utilization of the Sliding Mesh technique. A rough approximation suggests that the calm water and the shortest wave simulations require 640 cores (CPUs) for 36 days. However, for simulations in $\lambda/L = 1.1$ at $n = 24.54$ rps, this duration extends to roughly 44 days due to a smaller required time step.

7. Conclusions

In this study, the impacts of regular head waves on the propeller-hull interactions in model-scale were analyzed. RANS simulations in calm water and regular head waves of a propeller-appended hull, self-propulsion (SP), from the current paper were combined with the bare hull (BH) simulations results in Irannezhad et al. (2023) and propeller open water (POW) simulations in Irannezhad et al. (2024) in similar operational conditions to derive the propulsion characteristics of the ship, particularly the thrust deduction and wake fraction. The investigations were carried out for the KVLCC2 tanker at its design speed, in model-scale, free to heave, pitch and surge by means of a weak spring system, and equipped with the KP458 propeller, operating in calm water and three regular head waves with the same wave height and three different wave lengths, $\lambda/L = 0.6$, 1.1 and 1.6.

Due to the extremely large computational power requirements for running the SP simulations, it was not feasible in the current study to derive the precise propeller rotational speed at the self-propulsion point of the model (model SPP). Consequently, the propeller rotational speed in each condition was estimated to yield a near-to-zero mean surge and hence operating at a point very close to the model SPP. Therefore, in the current study, the thrust deduction factor, as one of the key investigated quantities, was derived considering a slight correction of the thrust deficit/excess from the estimated propeller rotational speed to reach the model SPP at the intended velocity. The corrections were made through the relatively small retained spring system forces (related to

the mean surge motion and acceleration) during a chosen time window of spring response time. Although this approach might not represent the full entailed physical effects at the model SPP, it is deemed to be a reasonably good approximation of it. Although it is preferable to run the simulations for a longer physical time to obtain more accurate spring system behavior, the investigated status of the simulations in the current paper was found to be fairly adequate for the overall ship performance evaluation.

The CFD results were compared to the available experimental EFD data in selective operational conditions. Overall, the CFD results were comparable to the EFD data, particularly when the discrepancies were compared in terms of magnitude. The propeller slipstream transient velocity distribution was also compared qualitatively between CFD and 2-Dimensional Stereo Particle Image Velocimetry (SPIV) measurements.

The time series of different quantities from the CFD results in different waves were compared during one wave encounter period. Interestingly, the motions were almost identical between BH and SP conditions, hence the nominal wake analysis from the BH investigations was used to analyze the propeller performance in SP condition. According to the BH studies, during one encountered wave period in regular head waves, substantial variations were seen for the axial velocity component of the surface-averaged nominal wake over the propeller disk $\tilde{u}$, and the time-averaged values $\bar{\tilde{u}}$ in all three waves were larger (around 9.8%, 21.3% and 14.6% for $\lambda/L = 0.6$, 1.1 and 1.6, respectively) than the calm water value. Overall, the variation of nominal wake in waves was found to be associated with the instantaneous propeller disk velocities, boundary layer contraction/expansion due to hull motions, bilge vortex dynamics, shaft vortex dynamics and the orbital wave velocities at the propeller disk as well as the complex interactions between these factors in different operational conditions. It was found that the large hull motions in the longer waves ($\lambda/L = 1.1$ and 1.6) dictated the variation of nominal wake through the contraction/expansion of the boundary layer as well as imposed vortical structure dynamics. However, the wave orbital velocities were the dominant factor in the shortest wave $\lambda/L = 0.6$ where the hull motions were insignificant.

The Taylor wake fraction was almost equal in all three wave lengths (and smaller than the calm water value), even though the propeller rotational speed was substantially different. Interestingly, the SP simulations and the applied thrust identity method yielded very similar

values for the Taylor wake fraction in all three waves, in contrast to the nominal wake in BH condition. However, the Taylor wake fraction was decreased in all three waves compared to the calm water value, or in other words, the advance velocity was increased in waves which was in line with the BH nominal wake observations.

The estimated thrust deduction factor in $\lambda/L = 0.6$, 1.1 and 1.6 was found to be respectively 12.8%, 26.1% and 12.9% smaller than the calm water value. The physical evidence of such reductions was discussed in this paper.

It was concluded that in $\lambda/L = 1.1$ and 1.6, due to very large shaft vertical motions and hence significant contraction/expansion of the boundary layer as well as strong vortical structure dynamics, the flow that was being ingested into the propeller during one encounter wave period was not solely and continuously from the aft ship boundary layer flow and hence, the wake had a larger momentum in comparison to the calm water wake which is heavily influenced by the hull boundary layer. Therefore, the incident flow to the propeller was expected to be substantially different and the primary acceleration of the flow and thus the impacts on the hull pressure distribution at the aft ship was not identical to the calm water condition. The diminished boundary layer flow acceleration and hence the less prominent change of pressure in the aft ship in SP in comparison to BH, in conjunction with the observed increase of $\bar{u}$ in $\lambda/L = 1.1$ and 1.6 were the most likely physical evidence that led to the decrease of thrust deduction factor in these waves. More significant shaft vertical acceleration in $\lambda/L = 1.1$ and thus longer time period of bilge vortex residence outside of the propeller incident field resulted in a fuller wake (higher $\bar{u}$ and thus less prone to be influenced by the propeller suction) in this wave in comparison to $\lambda/L = 1.6$, which was found to be the main reason for lower thrust deduction factor in $\lambda/L = 1.1$.

In $\lambda/L = 0.6$, due to the insignificant heave and pitch motions and hence smaller shaft vertical displacement, the aft ship pressure reduction, originated from the flow suction by the propeller, was rather concentrated on a roughly similar hull surface area as of calm water condition. On the one hand, the propeller rotational speed in this wave was larger than the calm water value to overcome the added resistance and reach the expected ship velocity at model SPP, which potentially can result in a more intense pressure reduction in the aft ship. On the other hand, a larger advance velocity was obtained in this wave versus calm water (due to the effects of the wave orbital velocities the nominal wake $\bar{u}$ increased by 9.8% in comparison to calm water). These counteracting effects possibly have resulted in a reduction of the thrust deduction factor in this wave with respect to the calm water value.

It is worthwhile to mention that the analysis in this paper mainly concerned the global effects as the analysis of the local physical phenomena associated with the propeller performance in regular head waves was intricate because of the unsteady and complex effects of the flow at various radial and azimuthal positions on different blades during the encounter period in waves. However, in a brief single-blade thrust investigation during one encounter wave period, it was seen that the large shaft vertical motions in $\lambda/L = 1.1$ and 1.6 resulted in significant local effects that led to the swap of the minimum thrust generation of the blade between $\Theta \approx 90°$ and $\Theta \approx 270°$ azimuthal positions.

The computational costs of running the simulations were extremely large, mainly due to the utilization of the discretized propeller approach and hence a very small time step as well as the consideration of the ship free to surge utilizing a weak spring system. The latter increased the complexity of the problem and its post-processing techniques but with the advantage of obtaining more accurate ship performance results in regular head waves with an intended velocity compared to the fixed surge conditions. However, it should be mentioned that the results and conclusions in this paper concerned only the KVLCC2 in model-scale and solely under selective operational conditions, at the design speed, fully-loaded operational condition, in calm water and three regular head waves, to name a few. However, as

a rough anticipation, it is likely from the current investigations that the full-scale motions would be rather similar, while the effects of boundary layer contraction/expansion and vortical structure dynamics would be reduced due to higher Reynolds numbers and hence the decline of viscous effects. This manuscript is under development and more analysis is in progress, which may lead to further revisions.

CRediT authorship contribution statement

Mohsen Irannezhad: Writing – review & editing, Writing – original draft, Visualization, Investigation, Formal analysis, Data curation, Conceptualization. **Martin Kjellberg:** Writing – review & editing, Supervision, Conceptualization. **Rickard E. Bensow:** Writing – review & editing, Supervision, Conceptualization. **Arash Eslamdoost:** Writing – review & editing, Writing – original draft, Supervision, Resources, Project administration, Funding acquisition, Conceptualization.

Declaration of competing interest

The authors declare that they have no known competing financial interests or personal relationships that could have appeared to influence the work reported in this paper.

Data availability

Data will be made available on request.

Acknowledgments

References

Baltazar, J., Rijpkema, D., Falcão de Campos, J., 2021. Prediction of the propeller performance at different Reynolds number regimes with RANS. J. Marine Sci. Eng. (ISSN: 2077-1312) 9 (10), http://dx.doi.org/10.3390/jmse9101115.

Berndt, J.C., Perić, R., Abdel-Maksoud, M., 2021. Improved simulation of flows with free-surface waves by optimizing the angle factor in the HRIC interface-sharpening scheme. J. Appl. Fluid Mech. (ISSN: 1735-3572) 14 (3), 909–920. http://dx.doi.org/10.47176/jafm.14.03.32062, URL https://www.jafmonline.net/article_1132.html.

Bhattacharyya, R., 1978. Dynamics of marine vehicles. In: A Wiley-Interscience publication, Wiley.

Bhattacharyya, A., Steen, S., 2014. Propulsive factors in waves: A comparative experimental study for an open and a ducted propeller. Ocean Eng. (ISSN: 0029-8018) 91, 263–272. http://dx.doi.org/10.1016/j.oceaneng.2014.09.020.

Cai, B., Mao, X., Xu, Q., Tian, B., Qiu, L., Zhan, X., 2023. Numerical simulation of KVLCC2 self-propulsion with ducted propeller in head waves. Ocean Eng. (ISSN: 0029-8018) 285, 115427. http://dx.doi.org/10.1016/j.oceaneng.2023.115427.

Faltinsen, O.M., Minsaas, K.J., Liapis, N., Skjørdal, S.O., 1980. Prediction of resistance and propulsion of a ship in a seaway.. In: Proceedings of the 13^{Th} Symposium on Naval Hydrodynamics. Tokyo, pp. 505–529.

Fenton, J., 1985. A fifth-order stokes theory for steady waves. J. Waterway Port Coastal Ocean Eng. 111 (2), 216–234. http://dx.doi.org/10.1061/(ASCE)0733-950X(1985)111:2(216).

Gerritsma, J., van den Bosch, J., Beukelman, W., 1961. Propulsion in regular and irregular waves. Int. Shipbuild. Prog. 8 (82), 235–247. http://dx.doi.org/10.3233/ISP-1961-88201.

Hasuike, N., Okazaki, M., Okazaki, A., Fujiyama, K., 2017. Scale effects of marine propellers in POT and self propulsion test conditions. In: Proceedings of the 5th International Symposium on Marine Propulsors. SMP'17, Espoo, Finland, URL https://www.marinepropulsors.com/proceedings/2017/TB2-2.pdf.

Huang, N., Attoh-Okine, N., 2005. The Hilbert-Huang Transform in Engineering. Taylor & Francis, ISBN: 9780849334221, http://dx.doi.org/10.1201/9781420027532.

Irannezhad, M., 2022. Numerical investigation of ship responses in calm water and regular head waves. In: Thesis for the degree of Licentiate of Engineering, Report no. 2022:04. (ISSN: 1652-8565) URL https://research.chalmers.se/publication/530499/file/530499_Fulltext.pdf.

Irannezhad, M., Bensow, R.E., Kjellberg, M., Eslamdoost, A., 2021. Towards uncertainty analysis of CFD simulation of ship responses in regular head waves. In: Proceedings of the 23rd Numerical Towing Tank Symposium (NuTTS 2021). Duisburg, Germany, pp. 37–42, URL https://www.uni-due.de/imperia/md/content/ist/nutts_23_2021_mulheim.pdf.

Irannezhad, M., Bensow, R.E., Kjellberg, M., Eslamdoost, A., 2023. Comprehensive computational analysis of the impact of regular head waves on ship bare hull performance. Ocean Eng. (ISSN: 0029-8018) 288, 116049. http://dx.doi.org/10.1016/j.oceaneng.2023.116049.

Irannezhad, M., Kjellberg, M., Bensow, R.E., Eslamdoost, A., 2024. Experimental and numerical investigations of propeller open water characteristics in calm water and regular head waves. Ocean Eng. (ISSN: 0029-8018) 302, 117703. http://dx.doi.org/10.1016/j.oceaneng.2024.117703, URL https://www.sciencedirect.com/science/article/pii/S0029801824010400.

ITTC, 2014a. International towing tank conference. recommended procedures and guidelines 7.5-03-02-03, "practical guidelines for ship cfd applications", 27th ITTC, 2014.

ITTC, 2014b. International towing tank conference. recommended procedures and guidelines 7.5-03-03-01, "practical guidlines for ship self-propulsion cfd", 27th ITTC, 2014.

ITTC, 2017. International Towing Tank Conference. Recommended Procedures and Guidelines 7.5-02-03-01.5, "Predicting Powering Margins", 28th ITTC, 2017.

ITTC, 2021a. International towing tank conference. dictionary of hydromechanics, prepared by the quality systems group of the 29th ITTC, 2021.

ITTC, 2021b. International towing tank conference. final report and recommendations from the seakeeping committee, 29th ITTC, 2021.

ITTC, 2021c. International towing tank conference. final report and recommendations from the specialist committee on modelling of environmental conditions, 29th ITTC, 2021.

ITTC, 2021d. International towing tank conference. final report and recommendations from the the resistance and propulsion committee, 29th ITTC, 2021.

ITTC, 2021e. International towing tank conference. recommended procedures and guidelines 7.5-02-03-01.1, "propulsion/bollard pull test", 29th ITTC, 2021.

ITTC, 2021f. International towing tank conference. recommended procedures and guidelines 7.5-02-03-01.4, "1978 ITTC performance prediction method", 29th ITTC, 2021.

ITTC, 2021g. International towing tank conference. recommended procedures and guidelines 7.5-02-07-02.2, "prediction of power increase in irregular waves from model test", 29th ITTC, 2021.

Kim, H., 2014. Phase-Averaged SPIV Wake Field Measurement for KVLCC2 Propeller Plane in Waves (Ph.D. thesis). Osaka University, Japan, http://dx.doi.org/10.18910/50513.

Kim, D.-H., Sanada, Y., Sadat-Hosseini, H., Stern, F., 2021. URANS simulations for a free-running container ship: Part 2. Added power. J. Hydrodyn. 33, 448–467. http://dx.doi.org/10.1007/s42241-021-0053-5.

Kim, B.-S., Wang, S., Zhu, Z., Kim, Y., 2023. Numerical simulation of free-running turning test of ship in waves. Ocean Eng. (ISSN: 0029-8018) 288, 115951. http://dx.doi.org/10.1016/j.oceaneng.2023.115951, URL https://www.sciencedirect.com/science/article/pii/S0029801823023351.

Lee, S.-H., Hwang, S., Kim, H.-S., Hyun, Y.-J., Lee, S.-K., Paik, K.-J., 2023. A numerical study on the hydrodynamic performance of a tanker in bow sea conditions depending on restraint conditions. J. Marine Sci. Eng. (ISSN: 2077-1312) 11 (9), http://dx.doi.org/10.3390/jmse11091726, URL https://www.mdpi.com/2077-1312/11/9/1726.

Lee, S.-H., Paik, K.-J., Cho, J.-H., Kim, G.-H., Kim, H.-S., Kim, S.-H., 2022. A numerical study on self-propulsion performance in regular waves and power prediction in irregular waves. Int. J. Naval Architect. Ocean Eng. (ISSN: 2092-6782) 14, 100454. http://dx.doi.org/10.1016/j.ijnaoe.2022.100454, URL https://www.sciencedirect.com/science/article/pii/S2092678222000206.

Lee, S.-H., Paik, K.-J., Hwang, H.-S., Eom, M.-J., Kim, S.-H., 2021. A study on ship performance in waves using a RANS solver, part 1: Comparison of power prediction methods in regular waves. Ocean Eng. 227, http://dx.doi.org/10.1016/j.oceaneng.2021.108900.

Lee, C.-M., Seo, J.-H., Yu, J.-W., Choi, J.-E., Lee, I., 2019. Comparative study of prediction methods of power increase and propulsive performances in regular head short waves of KVLCC2 using CFD. Int. J. Naval Architect. Ocean Eng. (ISSN: 2092-6782) 11 (2), 883–898. http://dx.doi.org/10.1016/j.ijnaoe.2019.02.001.

Lee, S.-K., Yu, K., Chen, H.-C., Tseng, R.K.-C., 2010. CFD Simulation For Propeller Performance Under Seaway Wave Condition. In: Proceedings of the 20th International Offshore and Polar Engineering Conference. Beijing, China, (ISSN: 1098-6189) pp. ISOPE–I–10–080, URL https://onepetro.org/ISOPEIOPEC/proceedings/ISOPE10/All-ISOPE10/ISOPE-I-10-080/11269.

Menter, F.R., 1994. Two-equation eddy-viscosity turbulence models for engineering applications. AIAA J. 32 (8), 1598–1605. http://dx.doi.org/10.2514/3.12149.

Mikkelsen, H., 2021. Numerical Study of Ship Performance in Calm Water and in Waves (Ph.D. thesis). Technical University of Denmark, URL https://orbit.dtu.dk/en/publications/numerical-study-of-ship-performance-in-calm-water-and-in-waves.

Moor, D.I., Murdey, D.C., 1970. Motions and propulsion of single screw models in head seas, Part II.. Trans. R. Inst. Naval Architect. 112 (2).

Muzaferija, S., Perić, M., 1998. Computation of free surface flows using interface-tracking and interface-capturing methods. In: Mahrenholtz, O., Markiewicz, M. (Eds.), Nonlinear Water Wave Interaction. WIT Press, Computational Mechanics Publications, Southampton, pp. 59–100.

Mwangi, B.O., 2021. SPIV Flow Field Measurement around the Stern of a Self-propelled KVLCC2 Model Ship in Regular Head Waves (Ph.D. thesis). Osaka University, Japan, http://dx.doi.org/10.18910/85407.

Nakamura, S., Naito, S., 1975. Propulsive performance of a container ship in waves. J. Soc. Naval Architect. Japan 15 (158), 24–48.

Perić, R., Abdel-Maksoud, M., 2018. Analytical prediction of reflection coefficients for wave absorbing layers in flow simulations of regular free-surface waves. Ocean Eng. (ISSN: 0029-8018) 147, 132–147. http://dx.doi.org/10.1016/j.oceaneng.2017.10.009, URL https://www.sciencedirect.com/science/article/pii/S0029801817306066.

Perić, R., Abdel-Maksoud, M., 2020. Reducing Undesired Wave Reflection at Domain Boundaries in 3D Finite Volume-Based Flow Simulations via Forcing Zones. J. Ship Res. (ISSN: 0022-4502) 64 (01), 23–47. http://dx.doi.org/10.5957/jsr.2020.64.1.23.

Perić, R., Vukčević, V., Abdel-Maksoud, M., Jasak, H., 2022. Optimizing wave generation and wave damping in 3D-flow simulations with implicit relaxation zones. Coast. Eng. (ISSN: 0378-3839) 171, 104035. http://dx.doi.org/10.1016/j.coastaleng.2021.104035, URL https://www.sciencedirect.com/science/article/pii/S0378383921001794.

Saettone, S., 2020. Ship Propulsion Hydrodynamics in Waves (Ph.D. thesis). Technical University of Denmark, URL https://orbit.dtu.dk/en/publications/ship-propulsion-hydrodynamics-in-waves.

Sanada, Y., Kim, D.-H., Sadat-Hosseini, H., Stern, F., Hossain, M.A., Wu, P.-C., Toda, Y., Otzen, J., Simonsen, C., Abdel-Maksoud, M., Scharf, M., Grigoropoulos, G., 2022. Assessment of EFD and CFD capability for KRISO container ship added power in head and oblique waves. Ocean Eng. 243, http://dx.doi.org/10.1016/j.oceaneng.2021.110224.

Seo, J.-H., Lee, C.-M., Yu, J.-W., Choi, J.-E., Lee, I., 2020. Power increase and propulsive characteristics in regular head waves of KVLCC2 using model tests. Ocean Eng. (ISSN: 0029-8018) 216, 108058. http://dx.doi.org/10.1016/j.oceaneng.2020.108058.

Sigmund, S., 2019. Performance of ships in waves (Ph.D. thesis). University of Duisburg-Essen, http://dx.doi.org/10.17185/duepublico/70021.

Simcenter STAR-CCM+ User Guide, 2023. Version 2023.10.

Tanibayashi, H., 1983. Effects of service conditions on propulsive perfromance of ships.. In: Conference on Seagoing Qualities of Ships and Marine Structures.. Varna, Bulgaria, p. 53, URL http://resolver.tudelft.nl/uuid:07acf32a-0835-4eb2-b0e3-2dcfae6c97ac.

Tavakoli, S., Khojasteh, D., Haghani, M., Hirdaris, S., 2023. A review on the progress and research directions of ocean engineering. Ocean Eng. (ISSN: 0029-8018) 272, 113617. http://dx.doi.org/10.1016/j.oceaneng.2023.113617, URL https://www.sciencedirect.com/science/article/pii/S002980182300201X.

Tokgoz, E., 2015. A CFD Study on the Propeller-Hull Interaction Flow in Waves Using Body-Force Distribution Model (Ph.D. thesis). Osaka University, Japan, http://dx.doi.org/10.18910/53979.

Ueno, M., Tsukada, Y., Tanizawa, K., 2013. Estimation and prediction of effective inflow velocity to propeller in waves. J. Marine Sci. Technol. 18, 339–348. http://dx.doi.org/10.1007/s00773-013-0211-8.

Van Sluijs, M.F., 1972. Performance and propeller load fluctuations of a ship in waves. URL https://repository.tudelft.nl/islandora/object/uuid:393be90b-6d2d-48d4-ae64-c5429d972075/datastream/OBJ, Netherlands Ship Research Centre TNO, *Report No. 163 S.*.

Woeste, J.T., O'Reilly, C.M., Gouveia, R.K., Young, Y.L., 2022. Propeller–hull interactions and added power in head seas. Ocean Eng. (ISSN: 0029-8018) 247, 110630. http://dx.doi.org/10.1016/j.oceaneng.2022.110630, URL https://www.sciencedirect.com/science/article/pii/S002980182200097X.

Wu, P.-C., Hossain, M.A., Kawakami, N., Tamaki, K., Kyaw, H.A., Matsumoto, A., Toda, Y., 2020. EFD and CFD Study of Forces, Ship Motions, and Flow Field for KRISO Container Ship Model in Waves. J. Ship Res. (ISSN: 0022-4502) 64 (01), 61–80. http://dx.doi.org/10.5957/jsr.2020.64.1.61.

Yu, J.-W., geun Kim, S., Jeong, W., Kim, Y.I., Choi, J.-E., Lee, I., 2022. Prediction of resistance and propulsion performances using calm-water and resistance tests in regular head waves of a 1,800 TEU container ship. Int. J. Naval Architect. Ocean Eng. (ISSN: 2092-6782) 14, 100458. http://dx.doi.org/10.1016/j.ijnaoe.2022.100458, URL https://www.sciencedirect.com/science/article/pii/S2092678222000243.